POLITECNICO DI TORINO

Ph.D. in Materials Science and Technology – cycle XXVI

Ph.D. Thesis

Metal oxide semiconductors as humidity and NO_x sensors for environmental monitoring

Mohamed Ahmed Abdelkader Abdelhamid Hassan

178752

Tutor

Prof. Jean-Marc Tulliani

January 2014

Summary

Semiconducting metal oxide (SMO) sensors are one of the most widely studied groups of chemiresistive gas sensors due to their unique advantages such as low cost, small size, measurement simplicity, durability, ease of fabrication, and low detection limits (< ppm levels). Moreover, most SMO based sensors tend to be long-lived and somewhat resistant to poisoning. The SMO undergoes reduction or oxidation while reacting with the target gas and this process causes an exchange of electrons at a certain characteristic rate, thereby affecting the sensor's resistance and yielding a certain signal.

The aim of this PhD is to fabricate new semiconducting metal oxide sensors capable of detecting humidity and/or NO_x gas.

The research is subdivided into three main different parts:

- The first is to prepare SMO sensors within a template (inorganic clay e.g. Sepiolite, glass):

a) ZnO has been synthesized into the sepiolite structure by means of different acid treatments in order to check the sensitivity of the resulting materials toward humidity and NO_2. Different samples have been prepared S1, S2, S6 and S24 for the samples acidified for 1, 2, 6 and 24 hours, respectively.

Sepiolite leached for 2 h (S2) showed a significant ability to detect quite low Relative Humidity (RH) values. Also, S2 revealed a significant capability for detecting NO_2 and H_2 in an optimal working temperature 300°C.

b) Crystallization of zinc oxide by melt quenching technique; The idea is to check the possibility to fabricate a percolated network from ZnO crystals within a glass matrix

by means of crystallization process then to test the resulting material as NO_x gas sensor.

A melt with nominal composition 58% ZnO 33.3% B_2O_3 4% WO_3 4% Bi_2O_3 has been quenched. The chosen glass sample was then subjected to the heat treatment for 15 hours at the temperature close to the established T_x (crystallization temperature).

As obtained glass ceramic material with adding a ZnO sol-gel (to improve the adhesion of the ink onto alumina substrate) gives a great ability to detect NO_2 at a quite low working temperature (150ºC), in conditions close to the environmental one's. This is a promising approach for glass ceramic materials in sensors application which could be used not only as humidity sensors but also for detecting other several gases with a quite good selectivity.

- The second part is Li – doped iron oxide as a new material for NO_2 detection:

Various compositions of lithium doped hematite containing 1, 2, 5, 10, 15, and 20 atomic percent were synthesized by solid state reaction. Electrochemical impedance spectroscopy (EIS) analyses under air and argon were used to determine the semiconducting behavior of the samples (n- or p-type) and to investigate the sensitivity of these materials towards NO_2.

Lithium doped hematite samples exhibit an n type semiconducting behavior. Lithium ferrites could work as NO_2 sensors at a quite low operating temperature (200°C). Generally, sensor response of lithium ferrites towards NO_2 revealed an acceptable linear evolution with gas concentration for some compositions.

- The third is commercial SMO; In_2O_3 and ZnO with different morphologies.

The objective of this work is the development of materials with hierarchical architectures for the realization of gas sensors capable of detecting low concentration of NO_2 in air at low temperature.

Different films have been prepared: ZnO and In_2O_3 thick films, ZnO thin films prepared by sol-gel technique, ZnO nanorods (NR) prepared by technology template of ZnO films obtained by Sol gel and ZnO nanowires (NW) prepared by electrospinning.

ZnO thick film and ZnO thin film have the best sensitivity towards NO_2 among the other samples.

Acknowledgments

Firstly, I thank Allah (Almighty) for helping me doing this PhD research during the last three years. Foremost, I would like to express my sincere gratitude to my advisor Prof. Jean-Marc Tulliani for the continuous support of my Ph.D study and research, for his patience, motivation, enthusiasm, and immense knowledge. His guidance helped me in all the time of research and writing of this thesis.
Besides my advisor, I would like to thank the rest of LINCE group, for their kind help during my lab activities.

My sincere thanks also go to Dr. Christian Lopez and all the staff in LEPMI - Grenoble, France. Also, Prof. Udo Weimar, Prof. Nicolae Barsan, and Susanne Wicker and all the staff in Weimar group, Universität Tübingen, Germany for helping me during my stay in their groups.

I thank also Matteo Pavese and Daniel Milanese for helping me in realizing some measurements in their labs.

I would like to thank my family: my parents, wife, sons (Abdelrahman, Yasmine), for supporting me spiritually throughout my life.

Last but not the least; I would like to dedicate this PhD to the martyrs of freedom in Egypt and the entire world.

Table of contents

Summary

Acknowledgments

1. Humidity sensors

1.1. Concept of Humidity

1.2. Humidity related definitions

1.3. Ceramic / Semiconductor humidity sensors

1.4. Water-adsorption mechanism on oxide surfaces

1.5. Ionic-type humidity sensors

1.5.1 Sensing mechanism of ionic-type humidity sensors

1.5.2. Microstructure and electrical properties

1.5.3. Performance of ionic-type humidity sensors

1.5.4. Influence of the addition of alkali ions

1.5.5. Performance of ionic-type humidity sensors in thick-film form

1.6. Electronic-type humidity sensors

1.6.1. Sensing mechanism of electronic-type humidity sensors

1.6.2. Performance of electronic-type humidity sensors

1.7. Solid-electrolyte-type humidity sensors

1.8. Ceramic thin films: towards integrated humidity sensors

1.9. Humidity sensitivity of rectifying junctions

1.9.1. P-n heterocontact-type humidity sensors

1.9.2. Metal/semiconductor interface-type humidity sensors

Conclusions

References

2. NO_x sensors

2.1. Development of air pollution emissions

2.2. Sources, occurrence in air and effects of NO_2

2.2.1. Sources

2.2.2. Occurrence in air

2.2.3. Effects of NO_2

2.3. Environmental monitoring of NO_X

2.4. European air quality standards for NO_2 and NO_X

2.5. Europe-wide survey of NO_2 and NO_X

2.5.1. Exceedances of limit values

2.5.2. NO_2 in rural, urban and traffic locations

2.5.3. Distance to target

2.5.4. Trends in NO_2 and NO_X concentrations

2.5.5. NO_X emissions

2.5.6. Relationship of NO_X emissions and NO_2 concentrations

2.6. Exposure to NO2 pollution in Europe

2.6.1. Human exposure

2.6.2. Exposure of ecosystems

2.7. Responses

2.8. Semiconducting metal oxides as environmentally hazardous gas sensors

2.8.1. Nitrogen dioxide sensors

Conclusions

References

3. Clays and sepiolite

3.1. Introduction

3.2. Sepiolite structure

3.3. Ion exchange

3.4. Clay-water relations

3.4.1. Solubility

3.4.2. High-temperature reactions

3.5. Characterization and experimental results

3.5.1. Humidity test

3.5.2. Measurements under NO_X and H_2

Conclusions

References

4. Hematite and ferrites materials

4.1. Principal iron oxides

4.2. Hematite properties

4.2.1. Principal properties of hematite

4.2.3. Hematite compound: ferrites based on alkaline and alkaline earth

4.2.3.1. Lithium ferrite

4.2.4. Ceramic sensors based on hematite elements

4.3. Li – doped iron oxide as a new material for NO_2 detection

4.3.1. Preparation Procedure

4.3.3. Humidity test

4.3.4. Electrical characterization by impedance spectroscopy

4.3.4.1. Measurements under air/argon

4.3.4.2. Measurements under NO_X

Conclusions

References

5. Glass – Ceramic sensors

5.1. Ceramic Materials and Sensors

5. 2. Adsorption and Ceramics

5.3. Electrical Conduction in Ceramic Materials

5.3.1. Charge carriers

5.3.1.1. Intrinsic charge carriers in stoichiometric hosts

5.3.1.2. Non-stoichiometry

5.3.1.3. Extrinsic charge carriers

5.3.1.4. Mobility

5.4. Electrical conductivity in oxides

5.5. Conduction Mechanisms

5.5.1. Sensor application using non-stoichiometric compounds

5.5.2. Sensor application using extrinsic ionic conductors

5.5.3. Sensor application using extrinsic electronic conductors

5.5.3.1. Extrinsic electronic conductors - bulk effect

5.5.3.2. Extrinsic electronic conductors - surface effect

5.6. Humidity sensors

5.7. Concluding Remarks

5.7.1. Microstructure of ceramics

5.7.2. Catalysis

5.8. Motivation of using glass ceramic as gas sensor

5.9. Experimental Work: Crystallization of zinc oxide by melt quenching technique

5.9.1. Material and Methods

5.9.1.1. Precursors

5.9.1.2. Preparation of material and methods

5.9.2. Physico-chemical data for the ternary system

5.9.2.1. Binary system Bi_2O_3-ZnO

5.9.2.2. Binary system Bi_2O3-WO_3

5.9.2.3. Binary system ZnO-WO_3

5.9.3. Characterizations

5.9.4. NO_2 sensitivity measurements

Conclusions

References

6. Commercial In_2O_3 and ZnO different morphologies NO_x sensors

6.1. Thin nanostructured films for gas sensing

6.2. Hierarchical structures for gas sensing

6.3. ZnO and In_2O_3 sensing materials choice

6.3.1. Zinc Oxide

6.3.1.1. Chemical Sensing prosperities of ZnO

6.3.2. Indium Oxide

6.3.2.1. General properties of In_2O_3

6.3.2.2. Sensing prosperities of In_2O_3

6.4. Characterization and experimental results

6.4.1. Powders characterization

6.4.2. Thick - films preparation

6.4.3. Thick - films characterization

6.4.4. Electrical Characterization – NO_2 response

References

Appendix: Characterization techniques

A.1. Pressing

A.2. Natural sintering

A.3. X-Ray diffraction

A.4. Laser granulometry

A.5. SEM

A.6. Porosimetry

A.7. The screen-printing technique

A.8. Screen-printing inks

A.9. Humidity measurement device

A.10. Impedance spectroscopy

A.11. BET

References

Chapter 1 - Humidity sensors

Humidity sensors have gained increasing applications in industrial processing and environmental control. For manufacturing highly sophisticated integrated circuits in semiconductor industry, humidity or moisture levels are constantly monitored in wafer processing. There are many domestic applications, such as intelligent control of the living environment in buildings, cooking control for microwave ovens, and intelligent control of laundry etc. In automobile industry, humidity sensors are used in rear- window defoggers and motor assembly lines. In medical field, humidity sensors are used in respiratory equipment, sterilizers, incubators, pharmaceutical processing, and biological products. In agriculture, humidity sensors are used for green-house air-conditioning, plantation protection (dew prevention), soil moisture monitoring, and cereal storage. In general industry, humidity sensors are used for humidity control in chemical gas purification, dryers, ovens, film desiccation, paper and textile production, and food processing. Humidity sensors are used for a wide variety of applications. Because applications in each field require different operating conditions, various types of humidity sensors based on a variety of sensing materials will be described. This paper is organized as follows. It begins with the classification of humidity sensors based on types of sensing materials and detection ranges. Then the relative humidity sensors based on ceramic, semiconductor, and polymer materials. Absolute humidity sensors, which were not extensive studied but are found wide-spread applications in many industrial fields [1].

1.1. Concept of Humidity

The water content in surrounding air is an important factor for the well-being of humans and animals. The level of comfort is determined by a combination of two factors: relative humidity and ambient temperature. You may be quite comfortable at−30°C (−22°F) in Siberia, where the air is usually very dry in winter, and feel quite miserable in Cleveland near lake Erie at 0°C (+32°F), where air may contain a substantial amount of moisture. Humidity is an important factor for operating certain equipment (e.g., high-impedance electronic circuits, electrostatic-sensitive components, high-voltage devices, fine mechanisms, etc.). A rule of thumb is to assure a relative humidity near 50% at normal room temperature (20–25°C).This may vary from a low as 38% for the Class-10 clean rooms to 60% in hospital operating rooms. Moisture is the ingredient common to most manufactured goods and processed materials. It can be said that a significant portion of the U.S. G.N.P. (Gross National Product) is moisture [2]. Humidity can be measured by instruments called hygrometers. The first hygrometer was invented by Sir John Leslie (1766–1832) [3]. To detect moisture contents, a sensor in a hygrometer must be selective to water, and its internal properties should be modulated by the water concentration. Generally, sensors for moisture, humidity, and dew temperature can be capacitive, conductive, oscillating, or optical. The optical sensors for gases detect dew-point temperature, whereas the optical hygrometers for organic solvents employ absorptive of near-infrared (NIR) light in the spectral range from 1.9 to 2.7 μm. There are many ways to express moisture and humidity, often depending on the industry or the particular application. The moisture of gases is expressed sometimes in pounds of water vapour per million cubic feet of gas. The moisture in liquids and solids is generally given as a percentage of water per total mass (wet-weight basis), but may be given on a dry-

weight basis. The moisture in liquids with low water miscibility is usually expressed as parts per million by weight (PPM_w). The term moisture generally refers to the water content of any material, but for practical reasons, it is applied only to liquids and solids, whereas the term humidity is reserved for the water vapour content in gases.

1.2. Humidity related definitions:

Moisture: the amount of water contained in a liquid or solid by absorption or adsorption which can be removed without altering its chemical properties.

Mixing ratio (humidity ratio) r: the mass of water vapour per unit mass of dry gas.

Absolute humidity (mass concentration or density of water vapour): the mass m of water vapour per unit volume v of wet gas: dw = m/v. In other words, absolute humidity is the density of the water vapour component. It can be measured, for example, by passing a measured quantity of air through a moisture-absorbing substance (such as silica gel) which is weighed before and after the absorption. Absolute humidity is expressed in grams per cubic meter, or in grams per cubic foot. Because this measure is also a function of atmospheric pressure, it is not generally useful in engineering practice [4].

Relative humidity: the ratio of the actual vapour pressure of the air at any temperature to the maximum of saturation vapour pressure at the same temperature. Relative humidity in percent is defined as

$$RH = 100\frac{P_w}{P_s} \qquad (1)$$

Where P_w the partial pressure of water is vapour and P_s is the pressure of saturated water vapour at a given temperature. The value of RH expresses the vapour content as

a percentage of the concentration required to cause the vapour saturation, [i.e., the formation of water droplets (dew) at that temperature]. An alternative way to present RH is as a ratio of the mole fraction of water vapour in a space to the mole fraction of water vapour in the space at saturation. The value of P_w together with partial pressure of dry air P_a is equal to pressure in the enclosure or to the atmospheric pressure P_{atm} if the enclosure is open to the atmosphere:

$$P_w + P_s = P_{atm} \qquad (2)$$

At temperatures above the boiling point, water pressure could displace all other gases in the enclosure. The atmosphere would then consist entirely of super- heated steam. In this case, $P_w = P_{atm}$. At temperatures above 100°C, RH is a misleading indicator of moisture content because at these temperatures P_s is always more than P_{atm}, and maximum RH can never reach 100%. Thus, at normal atmospheric pressure and a temperature of 100°C, the maximum RH is 100%, whereas at 200°C, it is only 6%. Above 374°C, saturation pressures are not thermodynamically specified.

Dew point temperature: the temperature at which the partial pressure of the water vapour present would be at its maximum, or saturated vapour condition, with respect to equilibrium with a plain surface of ice. It is also defined as the temperature to which the gas–water vapour mixture must be cooled isobarically (at constant pressures) to induce frost or ice (assuming no prior condensation). The dew point is the temperature at which relative humidity is 100%. In other words, the dew point is the temperature that the air must reach for the air to hold the maximum amount of moisture it can. When the temperature cools to the dew point, the air becomes saturated and fog, dew, or frost can occur. The following equations calculate the dew

point from relative humidity and temperature. All temperatures are in Celsius grades. The saturation vapour pressure over water is found from

$$EW=10^{0.66077+7.5t/(237+t)} \qquad (3)$$

While (EW: is the saturation vapour pressure over water)

The dew-point temperature is found from the approximation

$$DP = \frac{273.3(0.66077 - \log_{10} EW_{RH})}{\log_{10} EW_{RH} - 8.16077} \qquad (4)$$

$$EW_{RH} = \frac{(EW).(RH)}{100} \qquad (5)$$

The relative humidity displays an inverse relationship with the absolute temperature. The dew-point temperature is usually measured with a chilled mirror. However, below the 0°C dew point, the measurement becomes uncertain, as moisture eventually freezes and a crystal lattice growth will slowly occur, much like a snow flake. Nevertheless, moisture can exist for a prolonged time below 0°C in a liquid phase, depending on such variables as molecular agitation, rate of convection, sample gas temperature, contaminations, and so forth.

Frost point is the temperature (below 0°C) at which the vapour condenses to ice.

D/F PT is a function of the pressure of the gas but is independent of temperature and is therefore defined as absolute humidity measurement. *A part per Million (PPM)* represents water vapour content by volume fraction (PPMv) or, if multiplied by the ratio of the molecular weight of water to that of air, as PPMw.

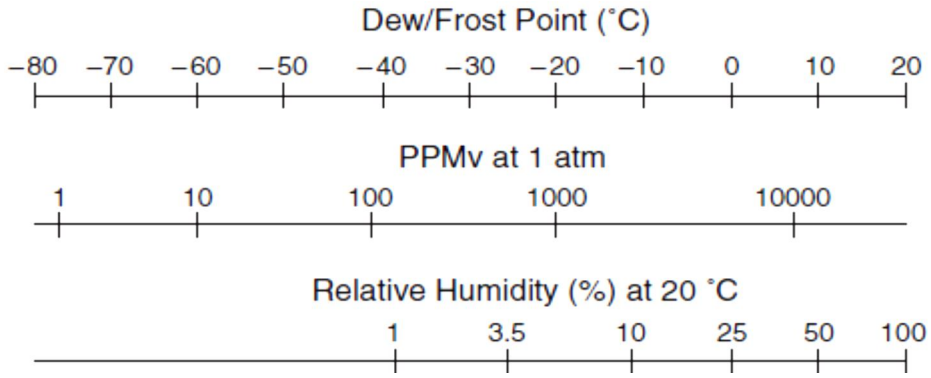

Fig.1.1 Correlation among humidity units: Relative Humidity (RH), Dew/Frost point (D/F PT), and Parts Per Million by volume fraction (PPMv).

1.3. Ceramic / Semiconductor humidity sensors:

Some ceramic oxides or composite oxides such as SnO_2, ZnO, and In_2O_3, etc. are wide-bandgap semiconductors. H_2O is adsorbed on the oxide surface in molecular and hydroxyl forms. Water molecules are observed to increase the conductivity of *n*-type ceramics and to decrease the conductivity of *p*-type ceramics. This effect has been attributed to the donation of electrons from the chemically adsorbed water molecules to the ceramic surface. Another mechanism was proposed. It was suggested that water molecules replace the previously adsorbed and ionized oxygen (O^-, O^{2-}, etc.) and therefore release the electrons from the ionized oxygen. Probably the "donor effect" could be resulted from both.

Because the conductivity is caused by the surface concentration of electrons, this sensing style is usually called "electronic type." However, the water layer formed by the physical adsorption may be somewhat proton conductive. Therefore, at room temperatures the conductivity of ceramic semiconducting materials is actually due to addition of both electrons and protons (ionic), unless at high temperatures (>100℃) moisture cannot effectively condense on the surface. In Figure 2a, the conductivity

increment is produced by surface electron accumulation resulting from the preferential alignment of the water dipoles. Hydrogen atoms contact the surface (mostly at the oxygen sites) and attract electrons outward. In Figure 2b, a depletion region forms originally due to adsorbed oxygen and the released electrons may neutralize the depletion. Since adsorbed water molecules increase the conductivity of *n*-type ceramic semiconductors, nearly all the published works deal with *n*-type ceramics [1].

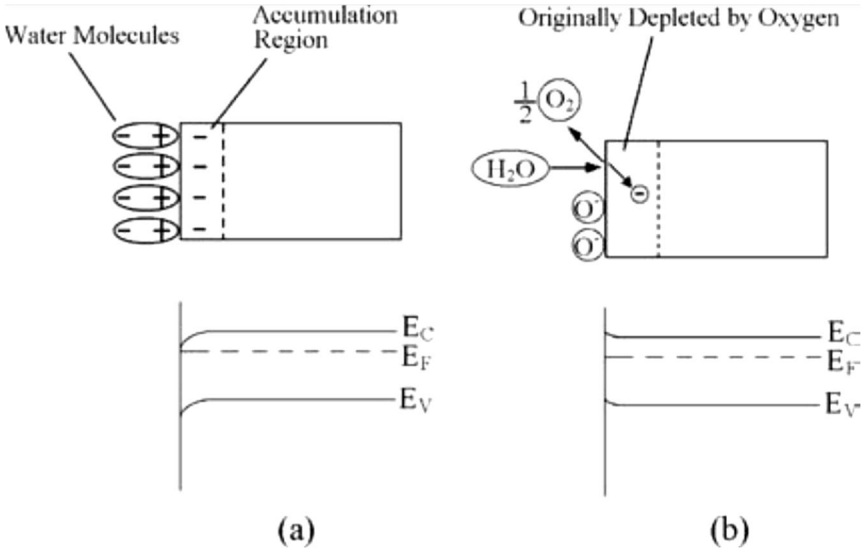

Fig.1.2. Two possible mechanisms for the "donor effect" (just for n-type): (a) Electrons are attracted by the adsorbed water molecules to the semiconductor surface and the energy bands are bended; (b) Electrons are released by the competitive adsorption.

It was reported that the change of conductivity was linear to certain exponential based on the proposed surface reaction mechanism. However, most of works lack the derivation for establishing strict reaction models.

Ceramic materials possess a unique structure consisting of grains, grain boundaries, surfaces and pores, which make them suitable for chemical sensors when they have a controlled microstructure. Compacts with a given microstructure can be produced by controlling the different steps of the ceramic production process. The modification of the microstructure and the chemical composition of ceramic materials permit both performance optimizations in sensors exploiting their electrical properties and tailoring to specific requirements. The problems for ceramic humidity sensors are mainly related to their need for periodic regeneration by heat cleaning to recover their humidity-sensitive properties; prolonged exposure to humid environments leads to the gradual formation of stable chemisorbed OH^- on the surface, causing a progressive drift in the resistance of the ceramic humidity sensor. The hydroxyl ions are removed by heating to temperatures higher than 400°C. Moreover, humidity sensors are usually exposed to atmospheres that contain a number of impurities, such as dust, dirt, oil, smoke, alcohol, solvents, etc. The adhesion or adsorption of these compounds on the ceramic surface causes irreversible changes in the sensor's response. Contaminants act in the same way as chemisorbed water, and may be removed by heating, too. Commercial sensors based on ceramic sensing elements were equipped with a heater for regeneration. The surface-related phenomena of humidity sensing by ceramics make these materials less resistant than polymers to surface contamination because of their porous structure.

Various humidity-sensing mechanisms and operating principles have been identified for ceramics. The type of conduction may be ionic or electronic. Most current humidity sensors are based on porous sintered bodies of ionic-type humidity-sensitive ceramics. Other humidity sensors using different sensing mechanisms are of the solid-electrolyte type, or use the heterocontacts between p- and n-type semiconducting

oxides. Different humidity-sensing mechanisms reported for ceramic materials are discussed, and examples of sensors are given. The relationship between electrical properties and microstructure will be focused. The recent trend towards the development of smart sensors integrated on a single chip, which needs the use of ceramic films, is discussed. The results obtained from humidity-sensitive p-n semiconducting oxide heterojunctions are also presented [5].

1.4. Water-adsorption mechanism on oxide surfaces

The electrical properties of ceramics change because of water-adsorption processes on their surface, which permit their use as humidity sensors, whatever their operating principle may be. As dry oxides are kept in contact with humid air, water molecules chemisorb on the available sites of the oxide surface, mainly at the neck parts of crystal grains, by a dissociative mechanism to form two hydroxyl ions for each water molecule; from each water molecule, the hydroxyl group adsorbs on metal cations present in the surface layer of the grains, which possess high local charge density and a strong electrostatic field, and the proton reacts with an adjacent surface O^{2-} group to form a second OH^- group. The chemisorbed layer, once formed, is not further affected by exposure to humidity. When the first layer of water molecules is formed, subsequent layers of water molecules are physically adsorbed on the first hydroxyl layer. The physisorbed water easily dissociates to form H_3O^+ because of the high electrostatic fields in the chemisorbed layer. The first layer of physisorbed water molecules is characterized by double hydrogen bonding of a single water molecule. The physisorption changes from monolayer to multilayer as the water-vapour pressure increases. Water molecules in the succeeding physisorbed layers are only singly bonded and form a liquid-like network. Therefore, singly bonded water molecules are

able to form dipoles and to reorient freely under an externally applied electric field, resulting in an increase in the dielectric constant. Physisorption of water molecules can take place at temperatures lower than 100°C. At higher temperatures, chemisorption of water molecules is only responsible for changes in the electrical conductivity of ceramics. Surface hydroxyls start to desorb at about 400°C. The interaction between the porous structure and water must also be considered. The presence of open porosity permits water condensation in the capillary pores. The quantity of condensed water depends on the available pore sizes and their distribution. It is possible to evaluate the pore radius at which capillary condensation occurs at different temperatures (T) by using the Kelvin equation

$$r_K = \frac{2\gamma M}{\rho RT \ln(P_s / P)} \qquad (6)$$

Where r_K is the Kelvin radius, P is the water-vapour pressure, P_s is the water-vapour pressure at saturation, and γ, ρ and M are the surface tension (72.75 dyn cm^{-1} at 20 °C), density and molecular weight of water, respectively. The water condensation takes place in all the pores with radii up to r_K, at given temperatures and water-vapour pressures. The smaller the r_K, or the lower the temperature, the more easily condensation occurs [6].

These physical interaction mechanisms between water and oxide surfaces are largely recognized to be the basis of the operative mechanisms of a wide range of different humidity-sensor materials.

1.5. Ionic-type humidity sensors

1.5.1 Sensing mechanism of ionic-type humidity sensors

The detection mechanism of ionic-type humidity sensors is strictly related to the above water-adsorption mechanisms. Moisture can be detected by measuring humidity-sensitive variations in conductivity, which ionic-type oxides undergo as a result of water adsorption. The oxides react to humidity by decreasing their resistivity, roughly exponentially with the relative humidity. The conduction mechanism depends on the surface coverage of adsorbed water. When only hydroxyl ions are present on the oxide surface, the charge carriers are protons, from hydroxyl dissociation, which hop between adjacent hydroxyl groups. When water is present, but surface coverage is not complete, H_3O^+ diffusion on hydroxyl groups dominates, but proton transfer between adjacent water molecules in clusters also takes place. When the first physisorbed water layer is continuous, charge transport is governed by proton hopping between neighbouring water molecules in the continuous film. The easy dissociation of physisorbed water, due to the high electrostatic fields in the chemisorbed layer, produces H_3O^+ groups. The charge transport occurs when H_3O^+ releases a proton to a nearby H_2O molecule, ionizing it and forming another H_3O^+, resulting in the hopping of protons from one water molecule to another. This process is known as the Grotthuss chain reaction, and it is assumed that it also represents the conduction mechanism in liquid water. This mechanism means that higher resistivity of the oxides is observed at low rh values. This is because mobile protons may arise from the dissociation of the hydroxyl groups or of the water molecules, but the activation energy required to dissociate hydroxyl ions is higher than that necessary to dissociate water molecules. A higher carrier concentration is found when more than one layer of physisorbed water molecule is present on the surface. These molecules are singly

hydrogen-bonded and form a liquid-like network, which greatly increases the dielectric constant and, therefore, the proton concentration. Moreover, in addition to the protonic conduction in the adsorbed layers, electrolytic conduction occurs in the liquid layer of water condensed within capillary pores, thereby resulting in an enhancement of conductivity. The rh sensitivity of a ceramic oxide is therefore related to the number of water-molecule adsorption sites, which may be increased by the presence of defect lattice sites and exogenous oxygen atoms at the oxide surface. Physisorption of water molecules plays a fundamental role in the working of this type of humidity sensor. It can operate at low temperature (<100 °C), and is widely accepted for many ionic ceramics, also of the non-oxide type.

1.5.2. Microstructure and electrical properties

The control of porosity and surface activity is of primary concern for ionic-type humidity sensors, because they rely on surface-related effects. High porosity and a large surface area are desirable to enhance sensitivity, in so far as they do not compromise mechanical stability. For all the materials investigated, from the earliest studies on, the importance of the pore-size distribution on the humidity-sensitive electrical response of ceramic porous compacts, and the intrinsic impedance of the sensing elements, have been emphasized. In order to obtain a good humidity-sensitive response, the resistivity of the materials must be high in nearly dry environments, and their total porosity and pore-size distribution must be controlled. A theoretical model for the calculation of impedance-humidity characteristics based on the use of the Kelvin equation was proposed by Shimizu et al. [7]. Knowledge of the pore size distribution, the intrinsic impedance of the sensor element and the conductivity of condensed water permits the calculation of the impedance-humidity characteristics. In

these calculations, the contribution of the thickness of the multilayer of adsorbed water on the impedance was neglected, i.e., the RH sensitivity was attributed only to the capillary condensation. This model was applied to spinel-type oxides. The relationship between the microstructure and the electrical properties of $MgAl_2O_4$ and $MgFe_2O_4$ spinel porous compacts has also been studied. Different pore-size distributions and microstructures were obtained using powders having very different porosity, surface area and grain size, which were prepared by wet-chemical methods or by solid state reactions between oxides, and sintered at various temperatures. Specimens with very different pore-size distributions were obtained, with rather high porosities. Table 1.1 shows examples of spinel-type oxide compacts with extremely different microstructures. The RH dependence of the resistance of the same samples measured at 40°C is shown in Fig.1. 3. It was observed that both total open porosity and pore-size distribution have a great influence on the resistance versus humidity sensitivity of spinel compacts. Best results were shown by samples with a wide distribution of pore sizes in the range 20-500 nm. The response time was also influenced by the microstructure. The presence of micropores, as in sample MF2, caused a slow response time, while the absence of micropores, such as in sample MF1, results in a fast response time (Fig.1.4) due to the easy adsorption and desorption of water molecules in large pores. An attempt to use the theoretical model of Shimizu et al. did not give satisfactory results for these samples. Sample MF1 only had pores larger than 100 nm. Using the Kelvin equation, at 40°C water condensation takes place in capillary pores with radii less than 10 nm at 90% RH, and therefore capillary condensation cannot be responsible for the RH sensitivity of this sample, which was of three orders of magnitude. It is likely that, in addition to capillary condensation and to the intrinsic resistance of the materials, surface conduction in

multilayered adsorbed water cannot be ignored in calculating the electrical response of humidity- sensitive ceramic oxides. For the same oxides Shimizu et al. observed good agreement between theoretical and experimental results only after boiling treatment with distilled water, which removed the surface ion impurity. This resulted in a small increase in the surface area and in the pore volume, but in a sharp lowering of sensitivity and increased impedance.

Table 1.1: pore size distribution (%) and specific surface area for $MgAl_2O_4$ and $MgFe_2O_4$ pellets.

Specimen	**Total open**	**Closed**	**<3.8 nm**	**3.8-10 nm**	**10-12 nm**	**20-100 nm**	**100-500 nm**	**>500 nm**	**BET (m^2g^{-1})**
MA1 [a]	59.6	3.4	13.3	1.0	4.4	22.4	13.9	4.6	13
MA2 [b]	56.5	6.5	5.7	9.1	35.8	5.9			65
MF1 [c]	40.0	3.0				0.8	37.3	1.9	1.3
MF2 [d]	55.7	1.3	1.0	1.1	19.5	17.8	15.3	1.0	21

[a] MA1: commercial $MgAl_2O_4$ powder sintered at 1300℃.

[b] MA2: $MgAl_2O_4$ powder from hydroxide decomposition sintered at 1100℃.

[c] MF1: $MgFe_2O_4$ powder from solid-state reaction sintered at 850℃.

[d] MF2: $MgFe_2O_4$ powder from hydroxide decomposition sintered at 750℃.

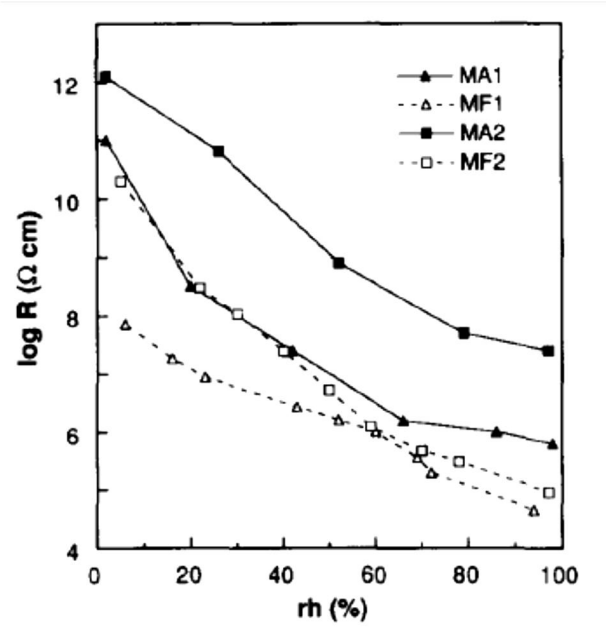

Fig.1.3. The RH dependence of the resistance of different sintered compacts of $MgAI_2O_4$ and $MgFe_2O_4$, at 40°C.

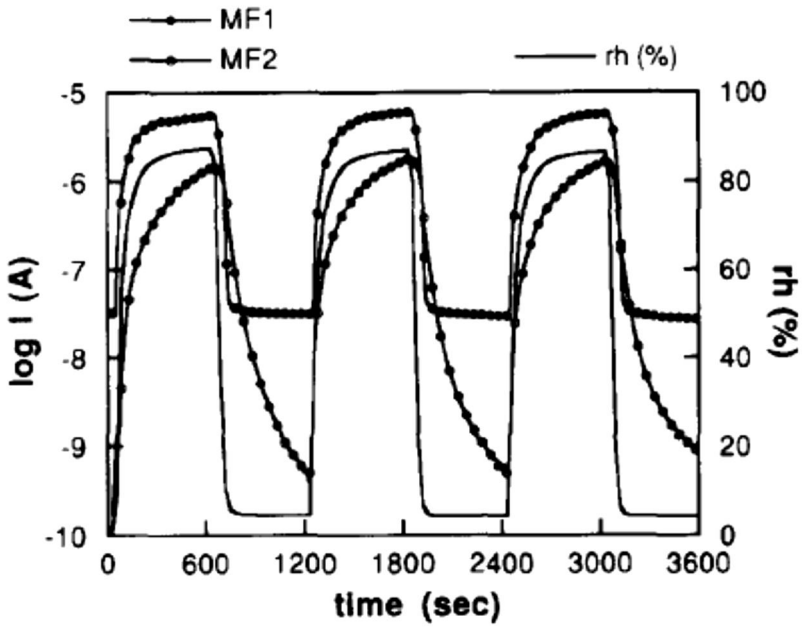

Fig.1.4. The response time of different $MgFe_2O_4$ sintered compacts to cycling RH at 40°C.

They interpreted the deviation of the calculated impedance from the experimental one as resulting from a difference between the water conductivity used in the calculation

and the actual conductivity of condensed water on the element, due to various ions dissolved from the element's surface. It may, however, also be explained in terms of a reduction in the number of water-adsorption sites after the boiling treatment.

The removal of the surface ions probably reduced the amount of adsorbed water, thereby resulting in decreased sensitivity and in increased resistivity. Indeed, the contribution of the water multilayer becomes negligible after the boiling treatment, and therefore there is better agreement between the theoretical and the experimental values. Furthermore, recent results showed the humidity dependence of the surface resistances of $LiNbO_3$ and $LiTaO_3$ single crystals. It was found that the logarithm of the surface electrical resistance decreased linearly with increasing RH. The maximum sensitivity over the RH range 30-90% was nearly two orders of magnitude for $LiNbO_3$. The humidity dependence of the electrical parameters was interpreted in terms of the water multilayer adsorption mechanism, with conduction due to the Grotthuss chain reaction. For single crystals, water condensation in capillary pores is to be excluded, again confirming the importance of the multilayered water to the humidity sensitivity of ceramics [8].

Another theoretical model has been proposed [9], which seems to follow the experimental results better. This model is based on the consideration that electronic and ionic conduction exist simultaneously in porous ceramics at any humidity. The resistance of the sensor element is given by the sum of electronic-type conduction for crystal grains and of ionic-type conduction from proton hopping between water molecules adsorbed on the grain surfaces.

The following equation was derived:

$$\lg(R_\Phi / R_0) = (\lg a - \lg \Phi)/(1 + b/\Phi) \qquad (7)$$

Where R_Φ and R_0 are the resistances of the porous ceramic element when the relative humidity is RH% and 0% respectively, Φ is the concentration of quasi liquid water (equal to $(RH)^n$, where n is the correction index) and a and b are theoretical constants depending on the composition of the ceramic and the pore structure [9]. This model takes into consideration the Grotthuss proton-transfer mechanism and the intrinsic resistivity of the materials. The same authors also proposed an interesting method for controlling the porosity of humidity-sensitive ceramics by using graphite powder as the pore former for Co-Fe and Mg-Cr spinels, which was removed during sintering. When graphite powder was added for the fabrication of porous Co-Fe spinel, the porosity of the specimen increased remarkably and graphite did not affect the composition of the matrix, thereby resulting in increased resistance versus RH sensitivity.

Summarizing, most of the ionic-type ceramic sensing elements have high porosities and wide pore-size distributions, up to radii in which capillary condensation cannot take place at any humidity at their operating temperatures. It is clear, from the empirical point of view, that one can obtain highly humidity-sensitive electrical properties using ceramics with high intrinsic impedance, a large pore volume and a wide distribution of pores over all the size ranges, i.e., micro-, meso and macropores. The behaviour of porous ceramic materials is affected by their intrinsic impedance, by water chemi- and physisorption on the oxide surface, which influences the surface resistance, and by water condensation within their porous structure leading to electrolytic conduction. Much work has still to be done to understand from the theoretical standpoint the relative weight of each of these phenomena on the RH sensitive electrical response of ionic-type porous ceramics.

1.5.3. Performance of ionic-type humidity sensors

The ionic-type humidity sensors utilize the decrease in impedance due to water adsorption. Many different kinds of materials have been used for these sensors, and new ones are continually being proposed. A resistive humidity sensor based on $MgCr_2O_4$-TiO_2 was developed for practical use in microwave ovens in 1978. The sensing element is a small, porous (35% porosity, with an average pore size of 300 nm) rectangular wafer made of a $MgCr_2O_4$-TiO_2 spinel solid solution with 35 mol% of titania, with porous RuO_2 electrodes and a coil heater for self-cleaning. The sensing element is heat cleaned at 500°C before each operation in order to eliminate the surface hydroxyl groups, which impede Grotthuss-type conduction, resulting in a drift of the resistance of the element. Fig.1. 5 shows the typical resistance-humidity characteristics of this sensor. The response time of the sensor is less than 10 s.

A ceramic sensor based on $ZnCr_2O_4$-$LiZnVO_4$ has been developed for use in air conditioners [10, 11]. The interesting feature of this sensor is that it can be operated without heat cleaning, because it does not show drifts in resistance as a result of exposure to wet environments. The resistivity of the sensor is mainly determined by water adsorbed on the amorphous phase, which has stable OH^- radicals on the surface on which water is physisorbed. Based on the same concept, a sensor using ZnO covered by a glassy porous phase of SiO_2 has been developed, showing good performance.

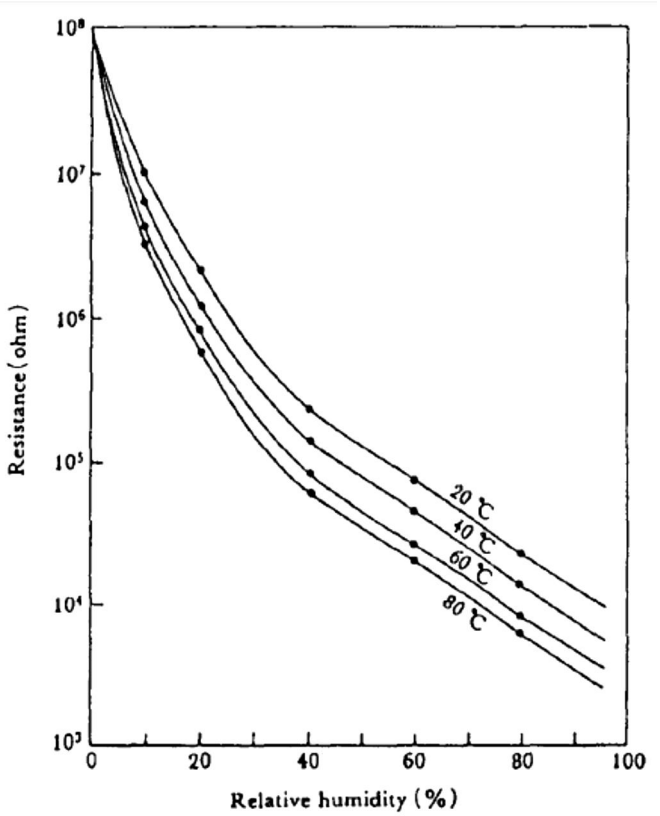

Fig.1.5. The RH dependence of the resistance of the $MgCr_2O_4$-TiO_2 sensor at different temperatures.

Many studies were devoted to TiO_2-based humidity sensitive materials as porous bodies. In general, the results obtained for pure TiO_2 were not completely satisfactory because of the high resistivity of TiO_2 and its poor long-term stability. However, the addition of Nb_2O_5 (0.5 mol %) to titania has been studied. The humidity sensitivity of Nb_2O_5-doped TiO_2 was greatly affected by the microstructure, which was varied by sintering at different temperatures. Figs.1.6 and 1.7 show the pore size distribution curves for samples sintered at various temperatures, and the corresponding impedance-RH characteristics, respectively [12]. The response time, which was rather fast for all the specimens, also depended on the microstructure of the specimens, being faster for samples with large pores. This material showed an impedance drift

during exposure to moisture, but an appropriate aging treatment at high temperature and high humidity was effective in reducing or eliminating the drift.

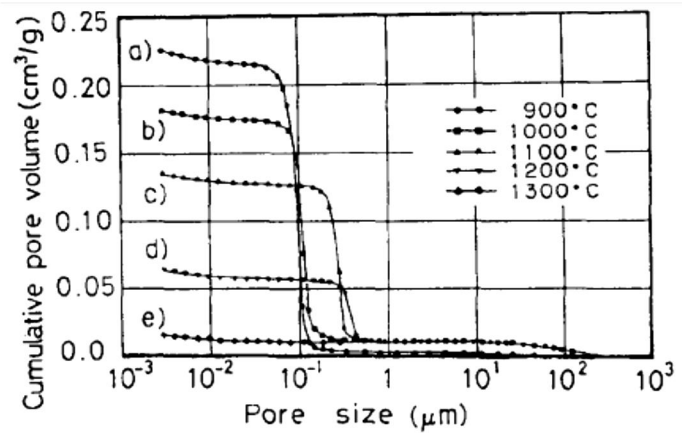

Fig.1.6. Pore-size distribution curves of Nb_2O_5-doped TiO_2 samples, sintered at (a) 900 °C, (b) 1000 °C, (c) 1100 °C, (d) 1200 °C and (e) 1300 °C.

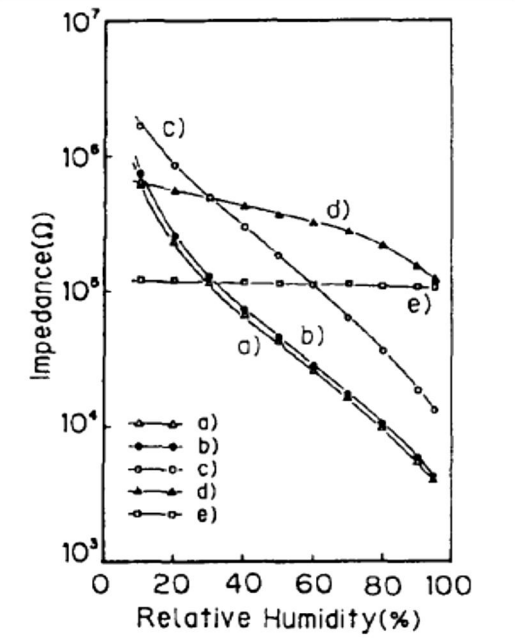

Fig.1.7. Humidity sensitivity measured at 25 °C of the Nb_2O_5-doped TiO_2 samples in Fig.1.6.

The use of porous La_2O_3-TiO_2-V_2O_5 glass ceramics has recently been proposed for humidity sensors. This is a phase-separable glass system, and the interesting feature of this kind of system is that it is possible to control the microstructure of the resulting porous glass by heat treatment to induce phase separation, and subsequent leaching to wash out the soluble phase. Moreover, it is also possible to choose from the various glass-ceramic systems one that has suitable intrinsic impedance.

Humidity sensitivity up to three orders of magnitude in the changes in impedance, in addition to good linearity of the logarithm of impedance in the whole RH range, has been reported. However, the shortest response time measured was 3 min, which is not a satisfactory value. This is probably due to the fact that the pores for this sensor are smaller than 5 nm.

1.5.4. Influence of the addition of alkali ions

The addition of alkali ions has been reported to be effective in improving the performance of many different kinds of materials. A number of different effects are related to the presence of alkalis. First, the addition of alkalis greatly affects the microstructure, thereby resulting in increased RH sensitivity. E.g. The addition of 2 mol% of potassium to $MgFe_2O_4$ produces an increase in open porosity, and a decrease in the grain size and in the average pore size (from 600 to 200 nm) for specimens sintered at 1050° [13]. Crystalline phases, such as K-Fe mixed oxides, are formed with increasing potassium content. The result of alkali addition is a great improvement in RH sensitivity over the entire RH range, as shown in Fig.1.8. The influence of alkali addition was found by Katayama et al. [14, 15] to influence the microstructure of Nb_2O_5-doped TiO_2. They found that the addition of potassium oxide was effective in decreasing the intrinsic impedance without affecting the humidity

sensitivity of Nb_2O_5-doped TiO_2, and in obtaining stable results because of the formation of physisorbed water, which was scarcely desorbed even at 50°C. The addition of K_2CO_3 allows TiO_2 to be easily sintered, with a decrease in the specific surface area and open porosity of the specimens, resulting in a decrease of physical adsorption sites. In this case, better performance of K-doped samples was observed for sintering temperatures lower than 1300°C. The addition of alkali oxides to $MgCr_2O_4$-TiO_2 has been used with the specific aim of modifying its microstructure [16].

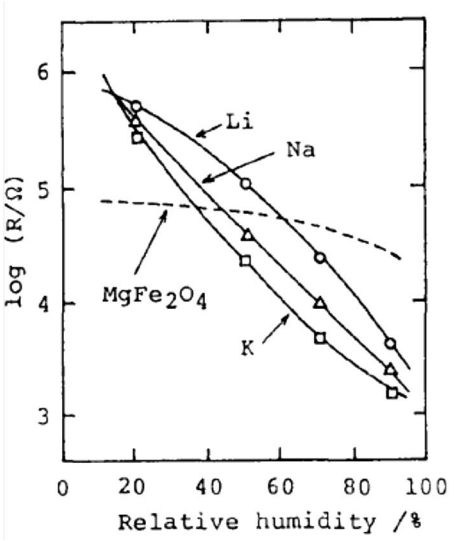

Fig.1.8. The RH dependence of the resistance of $MgFe_2O_4$ without and with alkali-ion additives at 25°C.

The creation of soluble phases is caused by alkali additives, which also affect the pore size distribution. These phases are subsequently dissolved out with the formation of micropores. The resultant material, especially after the addition of 10 wt% of Na_2O, shows improved characteristics for humidity sensing, such as sensitivity, linearity and hysteresis. On the other hand, the addition of sodium to SiO_2-based thick films lowered their intrinsic resistance without impairing the humidity sensitivity [17]. The microstructure of the film was also affected, with an increased number of large pores

in the range 1-10 μm. The conduction was ascribed to hydrated Na^+ ions moving between the adsorbed water molecules under an electric field, which explains the lowered resistance by a high number of charge carriers. The addition of alkaline oxides to zirconium phosphates, besides affecting the microstructure with a decrease in specific surface area on replacing the protons with alkali cations, also lowered the sensing material impedance and resulted in both stable humidity sensitivity over a long period of time and reduced hysteresis [18]. They interpreted these results in terms of conduction occurring also in the crystals. For these materials, the main charge carriers are the protons produced by the dissociation of the physisorbed water, but the alkali cations also act as charge carriers, and conduction takes place not only on the particle surfaces but also in the crystals. *Summarizing*, the addition of alkali ions appears to be quite effective on the humidity-sensitive electrical response of different materials, influencing their microstructure, which results in better performance, decreasing the intrinsic impedance or increasing the number of sites available for water adsorption.

1.5.5. Performance of ionic-type humidity sensors in thick-film form

One of the advantages of ceramic materials is that porous films can be produced using thick-film technology. These films have microstructural properties similar to those of sintered bodies, but can reduce the dimensions of the sensing devices, which can be used in hybrid circuits. Thick-film technology permits easy and reliable manufacturing with low-cost mass production. Many different materials have also been studied in thick-film form, using films prepared by screen printing or by dipping as coatings on a substrate with electrodes. Katayama et al. [19] developed a thick-film type sensor made of V_2O_5-doped TiO_2. The sensor was printed on an alumina

substrate by the conventional method. Its humidity-resistance characteristics are shown in Fig.1.9. The response of this kind of sensor readily changes upon exposure to humid air with contaminants. A specific filter has to be applied to the sensor to prevent contamination. With this filter, the sensor shows improved durability although its response time becomes longer. A hydroxide, such as the hydrotalcite-type $Zn_2Al(OH)_6Cl.\ nH_2O$, was used for the preparation of a new type of humidity sensor by the screen-printing technique. By using an original ink composed of an aqueous suspension of powder of the hydrotalcite type compound, very adherent deposits were obtained. The response time of this sensor was about 55 s and its RH sensitivity, evaluated as the ratio between the conductivities at 90 and at 10% RH, was about 50.

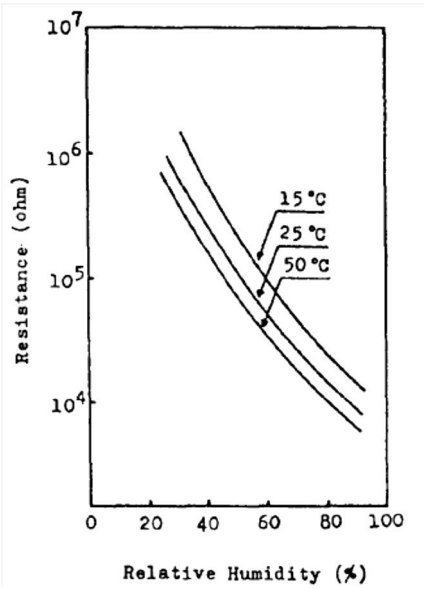

Fig.1.9. The RH dependence of the resistance of the V_2O_5-doped TiO_2 thick-film sensor at different temperatures.

A thick-film humidity sensor has been developed [20] for use in ordinary air-conditioning using NASICON, a material which had already been studied [21]. NASICON, which is a high ionic conductor, was selected in order to solve the problems generally posed by ceramic humidity sensors, i.e., high resistance at low

humidity and the need for periodic heat cleaning. NASICON was synthesized by the sol-gel method to obtain ultrafine porous powders, which were used for the preparation of thick films by screen printing. Amongst the NASICON materials, the phosphorus-free material showed comparatively low resistance at low RH and improved linearity. The relation between the logarithm of resistance and RH was nearly linear and hysteresis free in the RH range 20-90% and at operating temperatures from 0 to 60°C, as shown in Fig.1.10. When the RH was increasing, the response time was about 90 s, while it was about 130 s when the humidity was decreasing. There was very little change in the characteristics of the sensors not containing phosphorus during the operation, permitting use without heat-cleaning cycles [5].

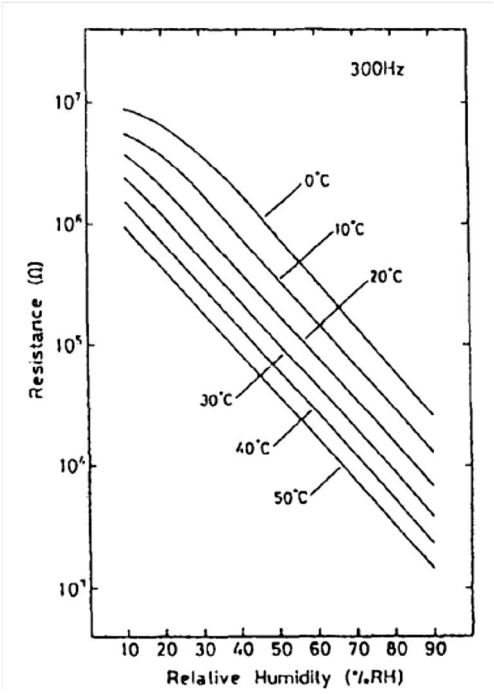

Fig.1.10. The RH dependence of the resistance of the P-free NASICON thick-film sensor at different temperatures.

1.6. Electronic-type humidity sensors

1.6.1. Sensing mechanism of electronic-type humidity sensors

The demand for humidity sensors able to operate at temperatures higher than 100°C led to the development of humidity-sensing devices based on different detection mechanisms. Semiconductor humidity sensors using metal oxides were proposed for this purpose, although some ionic conductor ceramics are also able to detect humidity at high temperatures. As the operating temperature of the sensors based on semiconductors is much higher than that of water physisorption, the observed change in electrical conductivity is based on the chemisorption of water molecules.

In this case, the sensitivity to humidity is a result of electronic conduction: when water molecules are chemisorbed on semiconducting oxides, their resistivity varies, decreasing or increasing according to the type of semiconducting oxides (n- or p-type). This indicates that electrons are apparently transferred from water molecules to oxide. The electrical behaviour of semiconductors in the presence of water vapour is thus similar to that observed when they are in contact with reducing gases. The surface of a semiconductor is adsorbed with oxygen ions in air, and these ions determine the resistivity of the oxide surface. An oxidative reaction takes place between the adsorbed oxygen and the introduced reducing gases, injecting electrons and thereby resulting in a decrease in resistivity for n-type semiconductors. It has been reported that co-adsorbed water on semiconductive oxides causes changes in the states and reactivities of adsorbed oxygen, affecting the oxide's conductivity. However, during the chemisorption reaction, when two hydroxyl groups are formed, with H^+ bonded to an oxide ion and OH^- to a metal ion, there is no electron transfer to the oxide. A different mechanism was proposed to explain the apparent electron donation from water molecules to perovskite-type oxides [22]. The humidity

sensitivity of perovskite-type oxides was attributed to the presence of surface defects with trapped electrons, such as ionized oxygen vacancies. Trapped electrons are liberated by the adsorption of water molecules.

On the basis of the experimental results of the variation of conductivity (σ) versus water partial pressure (P_{H_2O}), it was suggested that the dominant defect in $Sr_{1-x}La_xSnO_3$ is the singly ionized oxide ion vacancy ($V_o^{\cdot}$) [23]. Therefore, a dissociative adsorption reaction with one electron donation may be the mechanism of humidity sensing, for which conductivity is proportional to $P_{H_2O}^{1/3}$. On the other hand, for $SrSnO_3$ the presence of a fully ionized oxide ion vacancy (V_o^x) as the dominant surface defect was suggested, because σ was found to be proportional to $P_{H_2O}^{1/4}$ and thus a dissociative adsorption reaction with two electron donations seemed more likely. Another possible explanation of the fact that water molecules apparently behave as electron donors is that the electrons trapped by chemisorbed oxygen ions are retransferred upon exposure to water vapour pressure because of a displacement of oxygen ions by hydroxyl ions. In this case, it is supposed that one electron is retransferred to the oxide by the desorption of an oxygen ion, without electron transfer to the oxide from the subsequent chemisorption reaction of a water molecule at the available site, with the formation of two hydroxyl groups. The influence of water-vapour pressure on semiconductors at low temperatures must be also considered, where the neutralization of surface electric fields by the presence of physisorbed water takes place. It is likely that oxygen ions adsorb on the hydroxyl ions resulting from water chemisorption. In this absence of physisorbed water, the surface electric fields at the oxide surface will only be partially neutralized by chemisorbed water. Further physisorbed water molecules form dipoles that line up in the surface electric

fields in such a way as to neutralize any apparently charged sites, promoting oxygen desorption. The trapped electrons are restored to the conduction band (or to the valence band for p-type semiconductors), resulting in increased (or decreased for p-type) conductivity. This mechanism is responsible for the need to operate semiconductor gas sensors at elevated temperatures, where physical adsorption of water is minimized. In the same way, the humidity sensitivity of semiconducting oxides is affected by the presence of inflammable gases, which cause resistivity changes in the same direction as water vapour. This is one of the major problems related to the use of electronic conductivity- based humidity sensors.

1.6.2. Performance of electronic-type humidity sensors

It has been reported that perovskite-type oxides exhibit humidity sensitivity in the temperature range between 300 and 500°C [24]. Amongst the oxides tested, $SrSnO_3$ showed the best results. It was observed that n-type semiconductors are more suitable than p-type ones as humidity sensors because the conductivity changes upon water-vapour contact are greater for n-type than for p-type oxides.

One important problem of electronic-type humidity sensors is that their sensitivity is much lower than that of ionic-type sensors. Enhancement of their humidity sensitivity was obtained by partially substituting the A site element of $SrSnO_3$ with La^{3+} ions, with best results for the composition $Sr_{0.95}La_{0.05}SnO_3$, as shown in Fig.1.11. Further improvement of the sensitivity of $Sr_{0.95}La_{0.5}SnO_3$ was obtained by using Pt electrodes and by adding Pt articles, in a similar way to that observed for semiconductor gas sensors. The other important problem, the interference of reducing gases on humidity sensitivity, was overcome for humidity sensors based on $Sr_{1-x}La_xSnO_3$ by coating the sensing element with a Pt/Al_2O_3 catalyst. The effect of the sintering temperature on

the humidity sensitivity of $Sr_{0.95}La_{0.05}SnO_3$ was reported. The higher the sintering temperature, the higher the conductivity of the materials for a given water vapour pressure. This was explained in terms of a decrease in contact resistance between adjacent grains due to the sintering process. The decrease in surface area leads to a reduced number of active adsorption sites for chemisorbed water, thereby resulting in the observed reduction in humidity sensitivity with increasing sintering temperatures (Fig.1. 12). The mechanism of humidity sensing is thus related to surface phenomena. Although the influence of the microstructure on humidity sensitivity is far less for electronic-type sensors than it is for ionic-type sensors, the control of the microstructure of the sensing element is one of the important factors for the realization of improved sensitivity [5].

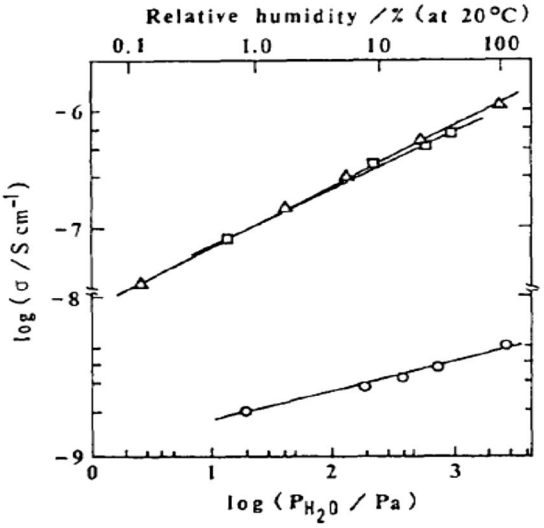

Fig.1.11. Effects of partial substitution of La^{3+} on humidity-sensitive characteristics: (O, $SrSnO_3$; Δ, $Sr_{0.95}La_{0.05}SnO_3$; □, $Sr_{0.9}La_{0.1}SnO_3$.

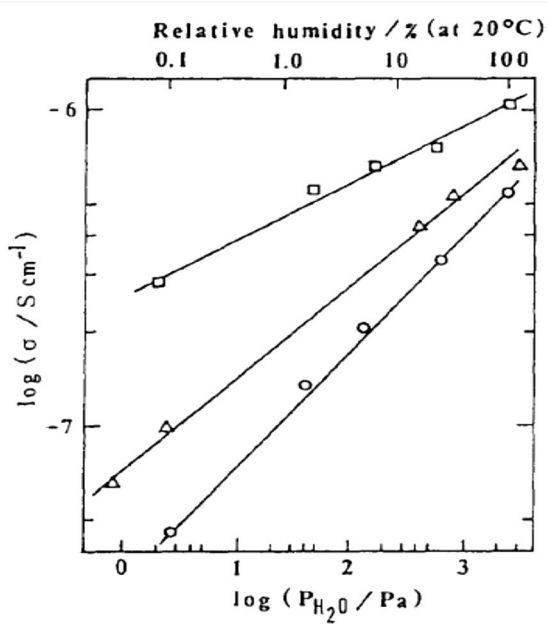

Fig.1.12. Effects of the sintering conditions of $Sr_{0.95}La_{0.05}SnO_3$ elements on their humidity-sensitive characteristics: O, 1200°C; Δ, 1300°C; □, 1400°C.

1.7. Solid-electrolyte-type humidity sensors

As already mentioned, in recent years humidity control at high temperatures has become more important for several industrial applications, such as drying processes and combustion control systems. Humidity sensors operating in the temperature range 100—300°C are required for the control of humidity in drying ovens. Solid electrolytes have also been studied for this purpose. Proton conductors have been used for humidity sensing at high temperatures. High proton conductivity, good stability at operating temperatures, low electronic conductivity and good mechanical properties are the requirements of the materials to be used as proton conductors in high-temperature electrochemical sensors. $SrCeO_3$- and $BaCeO_3$-based perovskite type oxides are stable and efficient proton conductors at temperatures above 400°C. These ceramics are only p-type electronic conductors in a hydrogen- or water vapour- free atmosphere. In the presence of these gases, electronic conduction decreases and

proton conduction appears. These materials have been used in water vapour concentration cells, the concept of which is shown in Fig.1.13. The variation of water-vapour pressure is measured by the electromotive force generated at the electrodes of the cell. The e.m.f varies linearly with the logarithm of water partial pressure. A humidity sensor using $SrCe_{0.95}Yb_{0.05}O_3$ has been studied in the temperature range 600-1000°C. The e.m.f, of the sensor had good reversibility and responded to the changes of humidity and temperature in about 1 min. The e.m.f was smaller than that expected from the Nernst equation (Fig.1.14) because the oxide is a mixed conductor of protons and positive holes. The difference between the theoretical and the experimental e.m.f, values became larger with increasing operating temperature, because p-type electronic conduction in the oxide was not negligibly small at high temperatures. The protonic conductivity in the Nd_2O_3-doped $BaCeO_3$ was found to be higher than that in the $SrCeO_3$-based proton conductor. The disadvantage of these voltammetric-type humidity sensors is that they need a reference atmosphere and this requires a complex structure for the measuring device.

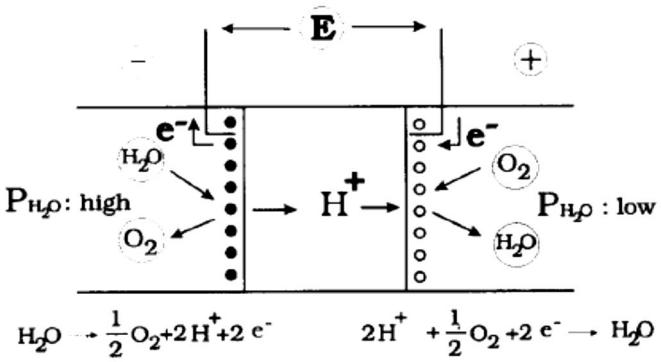

Fig.1.13. Concept of the water-vapour concentration cell.

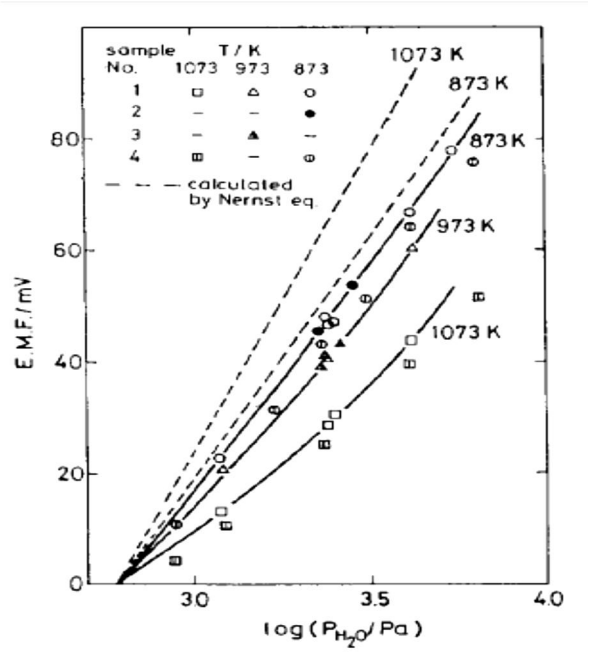

Fig.1.14. Reproducibility of e.m.f, of the $SrCe_{0.95}Yb_{0.05}O_3$ humidity sensor against changes of water-vapour pressure (P_{H_2O}) in air and temperature.

Another type of solid-electrolyte humidity sensor, which does not need a reference atmosphere, is based on yttria-stabilized zirconia , an oxide ion conductor, which uses the limiting current appearing in the diffusion- controlled electrolysis of water vapour and operates at 450°C [25]. Based on this principle, Yagi et al. developed a sensor with the cathode and the anode on the same plane; the cathode also acts as the diffusion control hole [26- 28]. The operating temperature range of this sensor is wide, from 20 to 300°C, and linear detection is available within the humidity range 0-500 mm Hg. The response time was about 1 min during adsorption and 2 min during desorption. With an additional cathode, it is possible to obtain a simple planar multifunctional sensor able to measure oxygen and humidity simultaneously [5].

1.8. Ceramic thin films: towards integrated humidity sensors

Recent trends in sensor production are towards silicon micromachining and on-chip integration technology. Miniaturization is one of the chief goals in the development of chemical sensors. Particularly in the chemical-sensor area, the development of microfabrication and micromachining technologies has provided outstanding new opportunities for advancement in this field. Many efforts are also devoted to the development of smart sensors, intended as sensors that have logic functions, ability for self calibration and/ or communication capability and for self-diagnostics. Integrated smart sensors are defined as chips that contain one or more sensors, signal conditioning, Analogic/Digital conversion, and a bus output. The final target is the development of intelligent systems, using all the aforesaid devices and technologies, which will be easy to operate and have microprocessor-compatible readouts.

However, not only electronics but also materials technology is fundamentally important in improving research and development on chemical sensors. The first step in the design of a sensing device, after establishing the sensing principle, is the choice of a suitably designed material, following the principles of materials science and technology. Complete understanding of the material's characteristics and of its sensing mechanism, using prototypes, is needed for the further development of advanced devices based on it. If the material works, the next step is miniaturization, followed by a smart structure design for reliable and advanced chemical sensors that perform well.

In the field of humidity sensors, several attempts have been made to integrate humidity sensors on silicon microchips, along with the ancillary linearization, temperature compensation and signal-conditioning circuitry needed for a practical device. Both polymeric and ceramic films have been investigated as humidity-sensitive elements. The integration of the sensing element with circuitry on a single

chip can reduce parasitic effects introduced by components of the external circuitry and increase the resolution of the measurements, especially for capacitance. Sensors using ceramic films have been reported with passive capacitive humidity-sensing elements and active humidity-sensing elements such as floating-gate FETs. These sensors use SiO_2 films, thermally grown on Si wafers or deposited by CVD. Attempts to improve the humidity sensitivity were made using porous films of $A1_2O_3$ formed by anodizing evaporated Al, or using MgF_2 deposited by vacuum evaporation. The recent development of ceramic deposition technologies is an important step towards the study of ceramics for integrated humidity sensors. Chemical and physical technologies are now available to deposit ceramic films. These technologies permit the miniaturization of humidity-sensing elements and on-chip integration capability. Using these technologies, it is possible to study the humidity-sensitive electrical properties of ceramic thin films in prototype sensors, with a view to their use in advanced devices prepared using electronics technology, should their performance be good. In recent years, the electrical response to humidity of porous films of $A1_2O_3$, grown by anodic oxidation of aluminum, by reactive ion plating or by reactive evaporation, has been studied [29].

Mainly, capacitive measurements were used for these humidity sensors. Commercial devices based on porous anodic alumina have been available for a number of years. Recently, films made of TiO_2, SiO_2 glasses or prussian blue prepared by the sol-gel method were studied,. This chemical technique is very attractive for the preparation of very uniform and highly pure ceramic powders, but its most promising feature is probably the possibility of powder-free processing of ceramics in their final shape (fibres or films), which can be used as active elements in sensing devices. A physical technique such as sputtering was used to prepare humidity-sensitive films of

$MgAl_2O_4$, of Fe_2O_3, of composite oxides with different compositions and of TiO_2. Pd-ZnO diodes produced by r.f. sputtering were studied with a view to integrating the sensor element and the processing circuits on the same silicon substrate. Sputtered $MgAl_2O_4$ thin films showed interesting characteristics in terms of their use in humidity sensors. Fig.1.15 shows the RH dependence of thin films, in comparison to that of a sintered compact of the same material. Resistance versus RH sensitivity values showed variations as high as four orders of magnitude in the whole RH range for thin films. The response time was evaluated as a few seconds. Conduction in thin films occurs through ionic carriers, while electronic conduction at low RH is negligible. The electrical response of spinel thin films depends on the number of water molecules adsorbed on their surface. The absence of capillary pores makes water condensation, and thus electrolytic conduction, impossible. These results confirm that the multilayered adsorbed water plays an important role in the humidity sensitivity of ceramics.

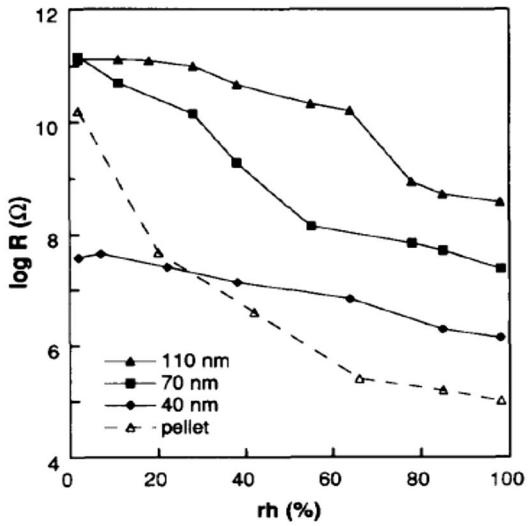

Fig.1.15. the RH dependence of $MgAl_2O_4$ sintered pellet and thin film resistance at 40°C

In the case of ceramic humidity sensors, the influence of the surface reactions and of grain boundaries is of primary importance. In order to determine all the characteristics of the materials before their use in sensors, the study of the surface of the materials intended for use in humidity sensors is of primary concern. X-ray photoelectron spectroscopy (XPS) can be very useful in the study of ceramic thin films for sensors. Detailed XPS studies of $MgAl_2O_4$ thin films and alkalidoped and undoped titania films prepared by the sol-gel method has been studied [30]. Using a combination of Ar^+ ion etching and XPS analysis of the layers at different depths, it was possible to determine the chemical composition at the film/substrate interface, and thus the compatibility between spinel films and silica substrates, which is fundamental to the evaluation of spinel films for on-chip integrated humidity sensors [5].

1.9. Humidity sensitivity of rectifying junctions

A recent approach to improving the sensitivity of gas sensors is the use of metal/semiconductor interfaces with diode behaviour. Initially, the reverse characteristics of a Schottky diode were found to be sensitive to flammable gases. However, very high sensitivity was found, exploiting changes in the non-linear part with forward-bias of current-voltage (I-V) characteristics for Schottky barriers upon exposure to different gases. Operating in the non-linear region of *I-V* curves of ZnO varistors was recently found to give very high hydrogen sensitivity. Furthermore, specific gas-sensing characteristics were reported for heterocontacts between p-type and n-type semiconductors, showing rectifying *I-V* curves typical of p-n junctions. Prototype sensors using bulk p-n heterocontacts or open p-n heterojunctions of thin films for the detection of different gases have been reported.

The concept of the use of the non-linear region of *I-V* curves was also applied for humidity detection.

1.9.1. P-n heterocontact-type humidity sensors

A new class of ceramic humidity sensors has been introduced by the discovery of Kawakami and Yanagida [31] who demonstrated that a heterocontact between p-type NiO and n-type ZnO showed *I-V* curves sensitive to humidity. P-n heterocontacts between bulk sintered bodies between CuO and ZnO have been developed. In order to overcome the poor reliability of mechanical contacts, open p-n heterojunctions of CuO/ZnO thin films were fabricated. Increasing humidity results in a substantial increase in the current flowing across the junction under a forward bias. The result is a highly rectifying device at high levels of RH, with polarity coincident with an ordinary p-n junction. These devices operate at room temperature. The mechanism attributed to these sensors is based on electrolysis of adsorbed water taking place at p-n contact sites. The amount of hydrolysis increases at higher relative humidity values, because the higher the humidity, the higher the amount of water adsorption. In the proximity of p-n junctions, electron holes are injected from the p-type semiconductor into the adsorbed water molecules, giving rise to protons in the adsorbed water phase. The positive charge is liberated at the surface of the n-type semiconductor, thereby resulting in electrolysis of the adsorbed water. The process of electrolysis provides a cleaning process during working with a self cleaning/ self-recovery mechanism. In this respect, p-n heterojunctions can be regarded as intelligent materials. However, no definitive proof is given in the relevant literature to confirm this mechanism. Other diode-type sensors used the junction between different carbon-type semiconductors. The humidity sensitivity of La_2CuO_4/ZnO heterocontacts has recently been

investigated Reference?. The heterojunctions were prepared by mechanically pressing sintered discs of the two oxides. Fig.1.17 shows the *I-V* curves of La_2CuO_4/ZnO heterocontacts measured at different RH values, which are typical of p-n diode behaviour. The rectifying character is enhanced with relative humidity. Very high sensitivity, expressed as $I/I_{4\%}$, where $I_{4\%}$ is the current recorded at 4% RH, was measured for the samples, up to about five orders of magnitude at 2.5 V and 86% RH. The RH sensitivity was bias dependent, and very large increases in current were recorded only with forward bias (Fig.1.18), whilst with reverse bias the samples were insensitive to RH. The response time at 1 V d.c. was evaluated at less than 20 s during adsorption and < 10 s during desorption. The response time was bias dependent, too: at 0.5 V it was <5 s during absorption and about 1 s during desorption. This fast response time probably indicates that the RH sensitivity relies on water physisorption. Fig.1.19 shows the high-frequency (100 kHz) capacitance- voltage (C-V) characteristic and the voltage dependence of $1/C^2$, measured at 86% RH. The diffusion potential at the junction interface is usually indicated by the intersection of the extrapolated line of $1/C^2$ in the reverse-bias region with the bias axis. However, in this case the diffusion potential value that was obtained was unrealistically large. Therefore, it was assumed that the interface barrier is not a physical diffusion barrier, but a chemical-like barrier due to the presence of a high density of interface states of external origin.

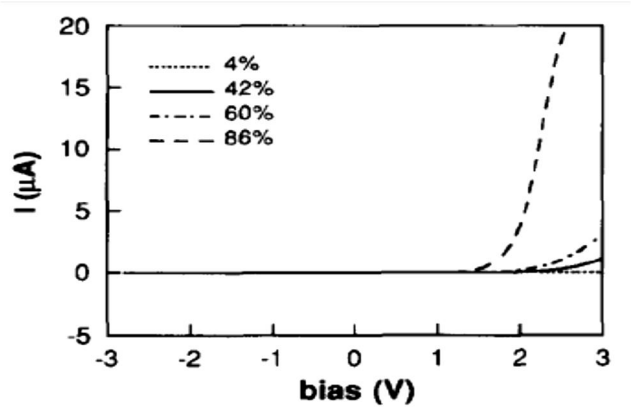

Fig.1.17. Dark I-V characteristics of ZnO/La_2CuO_4 heterocontacts at different rh values at 40°C.

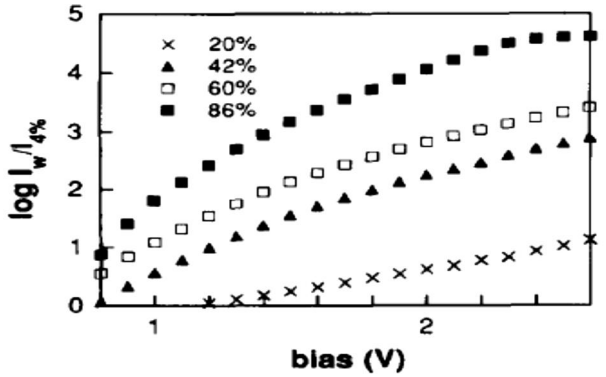

Fig.1.18. the bias-dependence of the RH sensitivity ($I/I_{4\%}$) of ZnO/ La_2CuO_4 heterocontacts at different relative humidity values, evaluated from I-V curves.

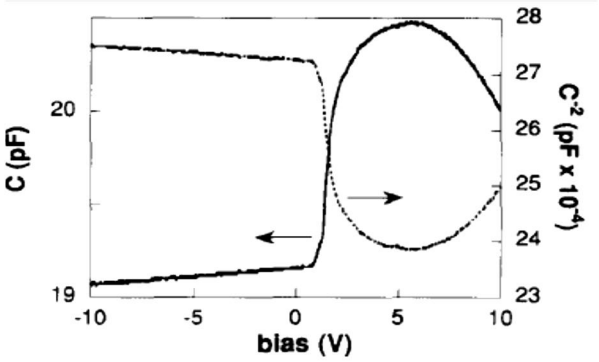

Fig.1.19. Dark high-frequency C-V characteristics and the bias dependence of $1/C^2$ of ZnO/La_2CuO_4 heterocontacts at 86% RH.

These results are largely consistent with those obtained for CuO/ZnO thin films. For these samples, it was determined that the presence of interface states is fundamental for their sensing properties. It is likely that at high RH values the saturation of the original interface states by physisorbed water leads to the release of trapped electrons, resulting in an increase in the forward current. This phenomenon may be assisted by water electrolysis, allowed by a continuous supply of water molecules.

1.9.2. Metal/semiconductor interface-type humidity sensors

Some attempts have been made to study metal/ semiconductor interface-type humidity sensors [32]. Sensing elements of perovskite-type oxides in contact with a metal needle were investigated. Diode-type *I-V* dependence was clearly observed on application of A1 or Fe needles to $LaCrO_3$ sintered bodies. Operating at temperatures between 20 and 30°C, an increase in the current flow at the same potential was recorded. This was interpreted in terms of a lowering of the potential barrier at the metal-oxide junction due to water adsorption, which facilitated electron transportation through the barrier and increased the current values. The humidity sensitivity of the rectifying *I-V* characteristics of Pd/ZnO diodes fabricated by r.f. sputtering has recently been reported [33] with increasing humidity, the current under forward bias increased remarkably with physisorption of water at the junction interface. Starting from these results, the author recently carried out several tests on ZnO dense pellets. It was observed that the introduction of a gold Schottky barrier made ZnO dense pellets sensitive to RH at room temperature. The dense ZnO pellets with two ohmic electrodes were insensitive to RH. Au/ZnO samples showed rectifying *I-V* characteristics. The RH sensitivity was bias dependent in the forward region. A maximum sensitivity $(I/I_{4\%})$ of about three was measured at 85% RH and 10 V

forward bias. A nearly linear forward current versus RH variation was observed in the RH range 4-85%.

The response time was slower than that observed for La_2CuO_4/ZnO heterocontacts.

These results may be explained in terms of a different humidity-sensing mechanism for Au/ZnO. The RH sensitivity cannot be explained in terms of ionic conduction, given the low resistivity and low porosity of ZnO. Moreover, ionic conduction cannot be dependent on the use of ohmic or non-ohmic electrodes. Also the electronic-type sensing mechanism cannot explain the results, because it takes place at high temperatures. The behaviour of Au/ZnO seems to be closer to that of p-n heterocontacts. The presence of a rectifying *I-V* characteristic, coming from a Schottky barrier in this case, or from p-n junctions, is responsible for the humidity sensitivity. The rectifying character may be related to the presence of surface/interface states. The neutralization of these states by means of physisorbed water may be the cause of the forward-current enhancement with RH. The linear relation of the forward current with RH, which shows that there is a direct proportion between forward current and the number of physisorbed water molecules, is consistent with the proposed humidity-detection mechanism of metal/semiconductor Schottky-barrier interfaces [5].

Conclusions

The continuous effort in the study of humidity sensors has led to novel sensing mechanisms that can be exploited in very different operating conditions. Although intensive studies began about 20 years ago, the influence of the microstructure on the electrical properties of ionic-type ceramic humidity sensors has yet to be clarified in terms of the influence of capillary condensation and of surface conduction in physisorbed water. In the case of thin films free of capillary pores, for certain materials it was possible to obtain a rather sensitive performance with a linear characteristic of the logarithm of resistance with RH. This is also very important for the development of integrated humidity sensors, which seems to be one of the main challenges for the future of humidity sensors.

References

1. Z. Chen and C. Lu, Humidity Sensors: A Review of Materials and Mechanisms, Sensor Lett., 3(4) (2005) 274–295
2. F. C. Quinn, The most common problem of moisture/humidity measurement and control. In: Moisture and Humidity, Proceedings of the 1985 International Symposium on Moisture and Humidity. Chaddock, J. B. ed., ISA, Washington, DC, 1985, pp. 1–5.
3. E. F. Carter, ed. Dictionary of Inventions and Discoveries. Crane, Russak and Co., New York, 1966. 3. Baughman E. H. and Mayes, D. NIR applications to process analysis. Am. Lab., 21(10) (1989) 54–58.
4. P. T. Moseley, J. O. W. Norris and D. E. Norris, Techniques and mechanisms in gas sensing, Adam Hilger Bristol, Philadelphia and New York (1991) 189-190.
5. E. Traversa, Ceramic sensors for humidity detection: the state-of-the-art and future developments, Sensors and Actuators B, 23 (1995) 135-156.
6. M. Egashira, M. Nakashima, S. Kawasumi and T. Seiyama, Temperature programmed desorption study of water adsorbed on metal oxides, Bulletin of the Chemical Society of Japan 51 (1978) 3144-3149.
7. Y. Shimizu, H. Ichinose, H. Arai and T. Seiyama, Ceramic humidity sensors. Microstructure and simulation of humidity sensitive characteristics, J. Chem. Soc. Jpn., (1985) 1270-1277.
8. J. H. Anderson and G.A. Parks, The electrical conductivity of silica gel in the presence of adsorbed water, Z Phys. Chem., 72 (1968) 3362-3368.

9. H. T. Sun, M.T. Wu, P. Li and X. Yao, Porosity control of humidity-sensitive ceramics and theoretical model of humidity sensitive characteristics, Sensors and Actuators, 19 (1989) 61-70.
10. Y. Yokomizo, S. Uno, M. Harata, H. Hiraki and K. Yuki, Microstructure and humidity-sensitive properties of $ZnCr_2O_4$- $LiZnVO_4$ ceramic sensors, Sensors and Actuators, 4 (1983) 599-606.
11. S. Uno, M. Harata, H. Hiraki, K. Sakuma and Y. Yokomizo, ZnCr204-LiZnVO4 ceramic humidity sensor, in T. Seiyama, K. Fueki, J. Shiokawa and S. Suzuki (eds.), Analytical Chemistry Symposia Series: Chemical Sensors, , Kodansha, Tokyo/Elsevier, Amsterdam, 17 (1983) 375-380.
12. Y.C. Yeh, T.Y. Tseng and D.A. Chang, Electrical properties of porous titania ceramic humidity sensors, J. Am. Ceram. Soc., 72 (1989) 1472-1475.
13. T. Suzuki and N. Matsui, Properties of humidity sensitive oxides with alkali additive, in T. Seiyama, K. Fueki, J. Shiokawa and S. Suzuki (eds.), Analytical Chemistry Symposia Series: Chemical Sensors, Kodansha, Tokyo/Elsevier, Amsterdam, 17 (1983) 381-386.
14. K. Katayama, K. Hasegawa, H. Osawa, T. Akiba and H. Yanagida, Effect of K_2HPO_4 addition on the humidity-sensitivity of Nb_2O_5-doped TiO_2, Sensors Mater., 2 (1990) 57-66.
15. K. Katayama, K. Hasegawa, T. Noda, T. Akiba and H. Yanagida, Effect of alkaline oxide addition on the humidity-sensitivity of Nb_2O_5-doped TiO_2, Sensors and Actuators B, 2 (1990) 143-149.
16. T.Y. Kim, D.H. Lee, Y.C. Shim, J.U. Bu and S.T. Kim, Effects of alkaline oxide additives on the microstructure and humidity sensitivity of $MgCr_2O_4$-TiO_2, Sensors and Actuators B, 9 (1992) 221-225.

17. F. Uchikawa and K. Shimamoto, Time variability of surface ionic conduction on humidity-sensitive SiO_2 films, Am. Ceram. Soc. Bull., 64 (1985) 1137-1141.
18. Y. Sadaoka, Y. Sakai and S. Mitsui, Humidity sensor using zirconium phosphates and silicates. Improvements of humidity sensitivity, Sensors and Actuators, 13 (1988) 147-157.
19. K. Katayama, T. Akiba and H. Yanagida, Rutile humidity sensor, in T. Seiyama, K. Fueki, J. Shiokawa and S. Suzuki (eds.), Analytical Chemistry Symposia Series; Chemical Sensors, Vol., Kodansha, Tokyo/Elsevier, Amsterdam, 17 (1983) 433 - 438.
20. H. Yagi and T. Saiki, Humidity sensor using NASICON not containing phosphorus, Sensors and Actuators B, 5 (1991) 135-138.
21. Y. Sadaoka and Y. Sakai, Humidity sensor using porous NASICON, Denld Kagaku, 53 (1985) 395-399.
22. T. Seiyama, N. Yamazoe and H. Arai, Ceramic humidity sensors, Sensors and Actuators, 4 (1983) 85-96.
23. Y.Shimizu, M. Shimabukuro, H. Arai and T. Seiyama, Humidity- sensitive characteristics of La3+-dope d and undoped SrSnO3, J. Electrochem. Soc., 136 (1989) 1206-1210.
24. H. Arai, S. Ezaki, Y. Shimizu, O. Shippo and T. Seiyama, Semiconduetive humidity sensor of perovskite-type oxides, in T. Seiyama, K. Fueki, J. Shiokawa and S. Suzuki (eds.), Analytical Chemistry Symposia Series: Chemical Sensors, Vol., Kodansha, Tokyo/Elsevier, Amsterdam, 17 (1983) 393 - 398.

25. T. Usui, Y. Kurumiya, K. Nuri and M. Nakazawa, Gaspolarographic multifunctional sensor: oxygen-humidity sensor, Sensors and Actuators, 16 (1989) 345-358.
26. H. Yagi and K. Ichikawa, Humidity sensing characteristics of a limiting current type planar oxygen sensor for high temperatures, Sensors and Actuators B, 13 (1993) 92-95.
27. H. Yagi and K. Ichikawa, High temperature humidity sensor using a limiting current type plane oxygen sensor, J. Cerant Soc. Jpn., 100 (1992) 282-286.
28. H. Yagi and K. Horii, Humidity sensing characteristics of a limiting current type plane oxygen sensor in high temperature environment, Denki Kagaku, 60 (1992) 220-225.
29. Z. Chen, M.C. Jin and C. Zhen, Humidity sensors with reactively evaporated A1203 films as porous dielectrics, Sensors and Actuators B, 2 (1990) 167-171.
30. R. Zanoni, G. Righini, A. Montenero, G. Gnappi, G. Montesperelli, E. Traversa and G. Gusmano, XPS analysis of sol-gel processed doped and undoped TiO2 films for sensors, Surface Interface Anal., 22 (1994) 376-379.
31. K. Kawakami and H. Yanagida, Effects of water vapor on the electrical conductivity of the interface of semiconductor ceramic-ceramic contacts, Z Cerant Soc. Jpn., 87 (1979) 112-115.
32. J. P. Lukaszewicz, Diode-type humidity sensor using perovskitetype oxides operable at room temperature, Sensors and Actuators B, 4 (1991) 227-232.
33. S. Tsurumi, K. Mogi and J. Noda, Humidity sensors of Pd-ZnO diodes, Tech. Digest, 4th Int. Conf. Solid-State Sensors and Actuators (Transducers '87), Tokyo, Japan, June 7-10, (1987) 661-664.

Chapter 2 - NO_X sensors

2.1. Development of air pollution emissions

The major classical air pollutants emitted into the atmosphere in Europe are sulphur dioxide (SO_2), nitrogen oxides (NO_X), ammonia (NH_3), non-methane volatile organic compounds (NMVOC) and particulate matter (PM).

Air pollutants have direct and indirect effects on human health. Sulphur and nitrogen compounds emitted into the air are potentially acidifying and can cause harm when deposited into sensitive terrestrial or aquatic ecosystems. Nitrogen compounds are also potentially eutrophying, i.e. can cause an oversupply of nutrients in soils and water bodies (Figure 2. 1).

Particulate matter emissions include primary PM and secondary particulates, formed from so-called PM precursor gases (SO_2, NO_X, NH_3, VOC and NMVOC). Primary PM is the fraction of PM that is directly emitted into the atmosphere, whereas secondary PM is the fraction of PM created in the atmosphere through oxidation of precursor gases, e.g. of SO_2, NO_X into sulphuric acid (liquid) and nitric acid (gaseous), respectively. Secondary organic PM can also be formed from the oxidation of volatile organic compounds (VOCs). Ozone (O_3) is formed in the atmosphere by reaction between NO_X and NMVOC gases in the presence of heat and sunlight. Ozone pollution is thus a major concern during the summer months. Presently, more than 2300 air quality monitoring stations report air pollution data to the European Environment Agency (EEA). Widespread observations started to become available at the European level in 1996/1997 [1].

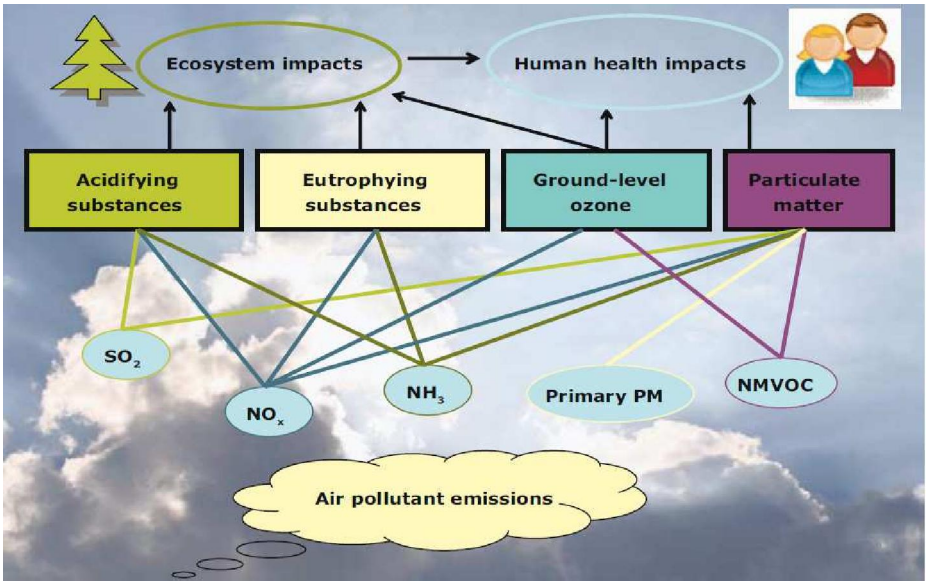

Fig.2.1.Major air pollutants in Europe clustered according to human health and ecosystem impacts [2]

The main air pollution issues in Europe are presently in the human health impact of exposure to particulate matter and ozone (and to a lesser extent NO_2, SO_2, CO, lead and benzene), in the acidification and eutrophication of ecosystems, in the damage to ecosystems and crops through exposure to ozone, in the damage to materials and cultural heritage due to exposure to acidification and ozone and in the impacts of heavy metals and persistent organic pollutants on human health and ecosystems.

The main sectors emitting air pollutants are road transport, power and heat production sectors, industry and agriculture (Table 2.1). Widespread exposure of the human population as well as ecosystems and materials to adverse air quality and deposition is the result. The household sector (e.g. home heating by wood and coal burning) can be an important source of air pollutants, especially PM, in some European areas.

Pollutant emissions are dispersed in air and are removed from the atmosphere by chemical reaction and deposition. The resulting pollutant concentrations vary strongly

by pollutant, location and time. The pollutants principally having high concentrations close to their emission sources include sulphur dioxide (SO_2), carbon monoxide (CO), nitrogen oxides (NO_X and NO_2) and benzene from streets and industrial plants. Other pollutants generally occur on a broader scale as a consequence of their formation and transformation under atmospheric transport. Ozone and the deposition of acidifying compounds fall into this category. These are observed typically as 'regional background' pollution levels, subject only to limited local modification.

The driving forces behind air pollution are directly associated with human activity, for which one priority measure is the gross domestic product (GDP). Energy consumption, industrial activities, transport demand and agriculture husbandry are the specific forces most directly linked to air emissions [2].

Table 2.1: Summary of impacts by sector upon acidification, eutrophication, particulate matter and ground level ozone production [2]

Economic sector	Issue contributed to	Pollutant of concern
Energy industrial	All four issue, but largest contributions to acidifying substances and particular matter (PM)	Mainly SO_2, but also NO_x and PM
Road transport	All four issue ,largest contributions to ozone formation precursors	Mainly NO_x and PM but also NMVOC and CO to ozone formation
Agriculture	Eutrophication and acidifying substances as	Mainly NH_3, but also PM

	well as to ozone formation	
Industrial energy and processes	Smaller contribution of four issues	Mainly SO_2 and NO_x
Residential	All four issues	Mainly SO_2 and NO_x and PM
Other energy	Mainly to ozone formation	NO_x and CO

The aim of European air quality legislature in recent years has been to coordinate an EU strategy through the twin-track approach of long-term air quality objectives together with air pollutant emission abatement measures.

Many chemical species of nitrogen oxides (NO_x) exist, but the air pollutant species of most interest from the point of view of human health is nitrogen dioxide (NO_2). Nitrogen dioxide is soluble in water, reddish-brown in colour, and a strong oxidant.

Nitrogen dioxide is an important atmospheric trace gas, not only because of its health effects but also because (*a*) it absorbs visible solar radiation and contributes to impaired atmospheric visibility; (*b*) as an absorber of visible radiation it could have a potential direct role in global climate change if its concentrations were to become high enough; (*c*) it is, along with nitric oxide (NO), a chief regulator of the oxidizing capacity of the free troposphere by controlling the build-up and fate of radical species, including hydroxyl radicals; and (*d*) it plays a critical role in determining ozone (O_3) concentrations in the troposphere because the photolysis of nitrogen dioxide is the only key initiator of the photochemical formation of ozone, whether in polluted or unpolluted atmospheres [3].

2.2. Sources, occurrence in air and effects of NO_2

2.2.1. Sources

On a global scale, emissions of nitrogen oxides from natural sources far outweigh those generated by human activities. Natural sources include intrusion of stratospheric nitrogen oxides, bacterial and volcanic action, and lightning. Because natural emissions are distributed over the entire surface of the earth, however, the resulting background atmospheric concentrations are very small. The major source of anthropogenic emissions of nitrogen oxides into the atmosphere is the combustion of fossil fuels in stationary sources (heating, power generation) and in motor vehicles (internal combustion engines). In most ambient situations, nitric oxide is emitted and transformed into nitrogen dioxide in the atmosphere. Oxidation of nitric oxide by atmospheric oxidants such as ozone occurs rapidly, even at the low levels of reactants present in the atmosphere. Altshuller [4] calculated that 50% conversion of nitric oxide would take less than 1 minute at a nitric oxide concentration of 120 $\mu g/m^3$ (0.1 ppm) in the presence of an ozone concentration of 200 $\mu g/m^3$ (0.1 ppm). Consequently, this reaction is regarded as the most important route for nitrogen dioxide production in the atmosphere. Other contributions of nitrogen dioxide to the atmosphere come from specific non combustion industrial processes, such as the manufacture of nitric acid, the use of explosives and welding. Indoor sources include tobacco smoking and the use of gas-fired appliances and oil stoves. Differences in the nitrogen oxide (nitric oxide and nitrogen dioxide) emissions of various countries are due mainly to differences in the consumption of fossil fuels. Worldwide emissions of nitrogen oxides in the early 1980s were estimated at approximately 150×10^{12} g/year [3].

2.2.2. Occurrence in air

Maximum 30-minute or 1-hour average and maximum 24-hour average outdoor nitrogen dioxide concentrations of up to 940 μg/m3 (0.5 ppm) and 400 $\mu g/m^3$ (0.21 ppm), respectively, have been reported [5-8]. Annual mean concentrations in urban areas throughout the world are generally in the range 20–90 $\mu g/m^3$ (0.01–0.05 ppm). Urban outdoor levels vary according to the time of day, the season of the year and meteorological factors. Typical daily patterns comprise a low background level on which are superimposed one or two peaks of higher levels that correspond to rush-hour traffic emissions of nitrogen oxides. Hourly average nitrogen dioxide concentrations near very busy roads often exceed 940 $\mu g/m^3$ (0.5 ppm). Maximum hourly concentrations in the United Kingdom are generally of the order of 470–750 $\mu g/m^3$ (0.25–0.4 ppm). From 1988 to 1990, highest 1-hour averages in the United States ranged from 75 to 1015 $\mu g/m^3$ (0.04–0.54 ppm). Thus, the maximal hourly mean value may be several times the annual mean. Long-term monitoring activities during the 1960s and 1970s indicated an increase in concentrations of nitrogen oxides in many urban areas throughout the world. Recent reports from the United States, however, show a decrease in nationwide nitrogen dioxide concentrations, resulting from a decrease in nitrogen oxides emissions, from 1981 to 1990. Whether nitrogen dioxide concentrations are increasing in urban areas in other parts of the world is unknown, although it is known that, at least in the United States, concentrations are highly correlated with population level and population levels worldwide continue to grow. Nevertheless, indoor sources, such as cooking with gas or cigarette smoking, may be the main contributors to individual exposure.

Owing to the widespread use of unvented combustion appliances, nitrogen dioxide concentrations in homes may exceed considerably those found outdoors. The average

concentration over a period of several days may exceed 200 μg/m^3 (0.1 ppm) when unvented gas stoves are used for supplementary heating or clothes drying, or when kerosene heaters are used; typically, means are lower. Maximum brief (minutes to 1-hour) concentrations in kitchens are in the range 230–2055 μg/m^3 (0.12–1.09 ppm) during cooking. The highest 15-minutes concentration recorded for a home with an unvented gas space heater was 2716 μg/m^3 (1.44 ppm) [3].

2.2.3. Effects of NO_2

Health effects can result from short-term exposure to NO_2 (e.g. changes in lung function in sensitive population groups) and long-term exposure (e.g. increased susceptibility to respiratory infection). Epidemiological studies have shown that symptoms of bronchitis in asthmatic children increase in association with long-term exposure to NO_2. Reduced lung function is also linked to NO_2 at concentrations currently found in cities of Europe and North America [9]. It should be noted that as NO_2 is highly correlated with other pollutants (in particular PM) it is difficult to differentiate the effects of NO_2 from those of other pollutants in epidemiological studies.

Nitrogen compounds have acidifying effects but are also important nutrients. Excess deposition of reactive nitrogen can lead to a surplus of nutrient nitrogen in ecosystems, causing eutrophication (nutrient oversupply) in terrestrial and aquatic changes in unique terrestrial, aquatic or marine animal and plant communities, including biodiversity loss [10].

Nitrogen oxides play a major role in the formation of O_3. They also contribute to the formation of secondary inorganic aerosols (SIA), through nitrate formation, contributing to PM_{10} and $PM_{2.5}$ concentrations [11].

2.3. Environmental monitoring of NO_X

Nitrogen oxide is an important gaseous air pollutant. It plays a major role in atmospheric chemistry, particularly in the formation of secondary air pollutants such as ozone, peroxyacyl nitrate (PAN), nitrate aerosols, and contributes to environmental acidification. A comprehensive assessment of NO_X levels in the atmosphere is required for developing effective strategies to control air pollution and to improve air quality.

Consequently, spatial NO_X monitoring has become an important aspect of air quality assessment. Present NO_X monitoring networks are mostly confined to urban areas, having a limited number of monitoring sites.

Wide spatial NO_X monitoring is constrained because of the limited availability of the monitoring equipment, such as continuous chemiluminescence monitors, high volume, handy samplers and high prize. Moreover, they require elaborate infrastructures, scientific personnel, technical support and uninterrupted power supply. In an effort to overcome the above shortcomings, passive samplers have been successfully used for large scale monitoring of NO_X in the ambient environment [2].

2.4. European air quality standards for NO_2 and NO_X

European air quality standards for NO_2 and NO_X as set by the 2008 Air Quality Directive (EU, 2008c) are shown in Table 2.2. For NO_2 two limit values and an alert threshold are defined for the protection of human health. The limit values are specified for short-term (one-hour) and long-term (annual) exposure and EU Member States were obliged to meet them by 1 January 2010. The one-hour value can be exceeded up to 18 times per year before the limit value is breached. A critical level is

set for the annual mean of NOX for the protection of vegetation, defined as the sum of NO and NO_2 expressed in units of mass concentration of NO_2.

The 2008 Air Quality Directive (EU, 2008c) also defines an alert threshold value of 400 µg/m^3. When exceeded over three consecutive hours in areas of at least 100 km^2 or an entire air quality management zone, authorities have to implement short-term action plans. These action plans may include measures in relation to limiting motor-vehicle traffic, construction works, ships at berth, and the use of industrial plants or products and domestic heating. Specific actions aiming at the protection of sensitive population groups, including children, by reducing their exposure to high NO_2 levels may also be considered in the framework of those plans.

The threshold values used in the human health objectives set by the 2008 Air Quality Directive are identical to the WHO air quality guidelines for NO_2, shown in Table 2. 2 [12].

Table 2.2: Limit and threshold Values for NO_2 and NO_x as set out in the Air Quality Directive

Objective	**Averaging period**	**Limit or threshold Value**	**Number of allowed exceedances**
Human health	One hour	200 µg/m^3	18 hours per year
Human health	Calendar year	40 µg/m^3	
Alert [(a)]	One hour	400 µg/m^3	
Vegetation [(b)]	Calendar year	30 µg/m^3	

Note: (a) To be measured over three consecutive hours at locations representative of air quality over at least 100 km^2 or an entire zone or agglomeration, whichever is smaller.

(b) As NO_X, expressed as μg NO_2/m^3.

Source: EU, 2008c [13].

μg/m³	**1-hour mean**	**Annual mean**
NO_2	200	40

2.5. Europe-wide survey of NO_2 and NO_X

2.5.1. Exceedances of limit values

The limit value of the annual mean NO_2 concentration is set at 40 μg/m3 and countries were obliged to meet this by 2010. In 2010, 22 of the 27 EU Member States recorded exceedances of the limit value at one or more stations (orange and red spots in Fig.2. 2, 4). The distance-to-target plots show that the lowest concentration levels and fewest exceedances occur at rural stations and the highest concentrations and exceedances are at traffic stations (Figure 2. 3). Guerreiro et al. [14] provide a thorough discussion of NO_2 concentrations at hotspots close to traffic and also in the urban background.

2.5.2. NO_2 in rural, urban and traffic locations

Nitrogen dioxide concentrations vary between rural, urban and traffic sites in a different manner from PM and O_3. Nitrogen dioxide concentrations are higher close to the sources and at traffic stations, decreasing in quantity in urban background areas. The lowest concentrations are found in rural areas (Figure 2. 3 and Figure 2. 5). While

secondary PM and O_3 are formed regionally from precursor gases, chemical reactions are less likely to create NO_2 on this geographical scale. For most NO_X sources, the share of NO in NO_X emissions is much greater than that of NO_2, typically 10–20 times higher. The NO_2 concentration is then increased at the expense of NO, due to reactions with O_3. In traffic and urban areas with fresh inputs of NO, some of the O_3 present is depleted while oxidising NO to NO_2. In rural areas relatively limited fresh NO emissions are available, except near highways and near combustion plumes. The reaction between NO, NO_2 and O_3 leads to chemical equilibrium.

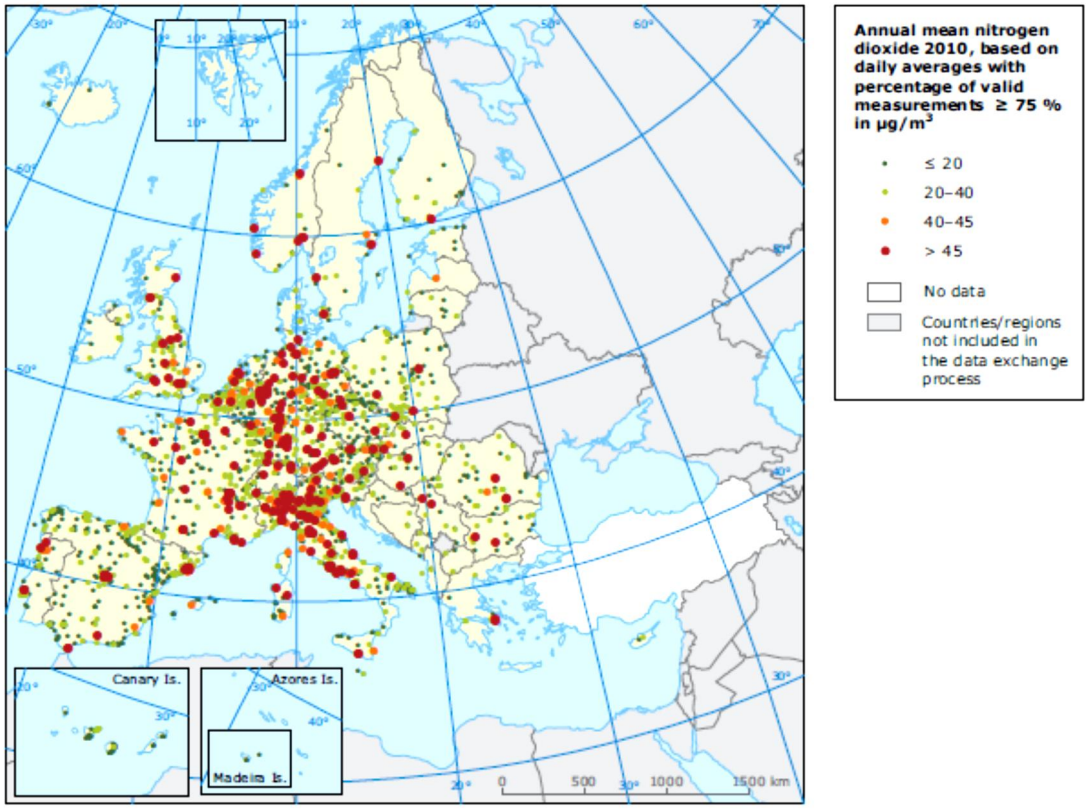

Note: Orange and red dots correspond to exceedances of the annual limit value (40 µg/m^3). Red dots correspond to exceedances of the annual limit value + 5 µg/m^3.

Source: AirBase v. 6.

Fig.2.2: Annual mean concentration of NO_2 in 2010.

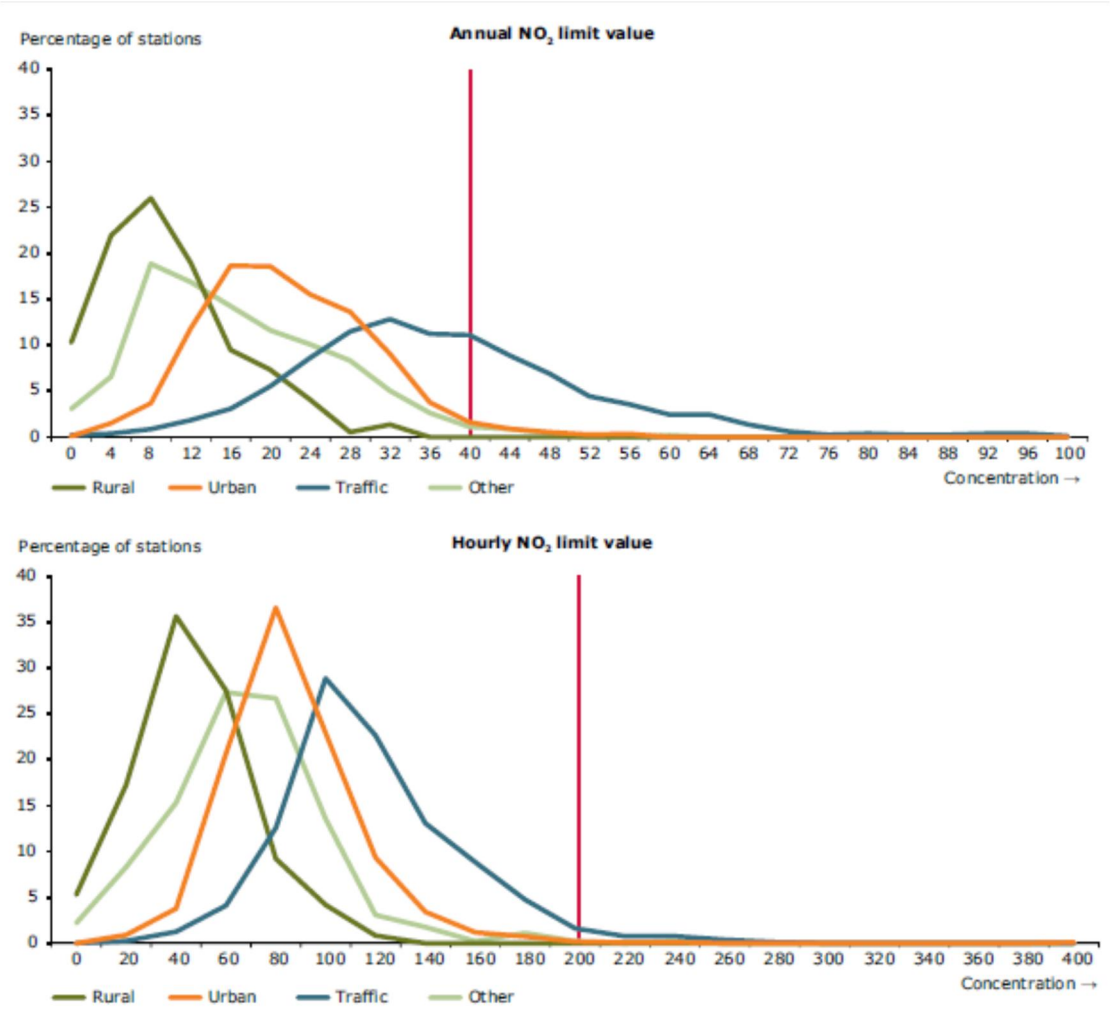

Note: The graphs show the percentage frequency distribution of stations (on the y-axis) in the EU Member States versus the various concentration classes (on the x-axis, in µg/$^{m3)}$. Vertical lines correspond to limit values set by the EU legislation.

Source: AirBase v. 6.

Fig.2.3: Distance-to-target graphs for the annual (top) and hourly (bottom) NO_2 limit value, for different station types, 2010.

Fig.2.4: shows the annual mean NO_2 values for 2010, 2005 and 2001 for all EU Member States.

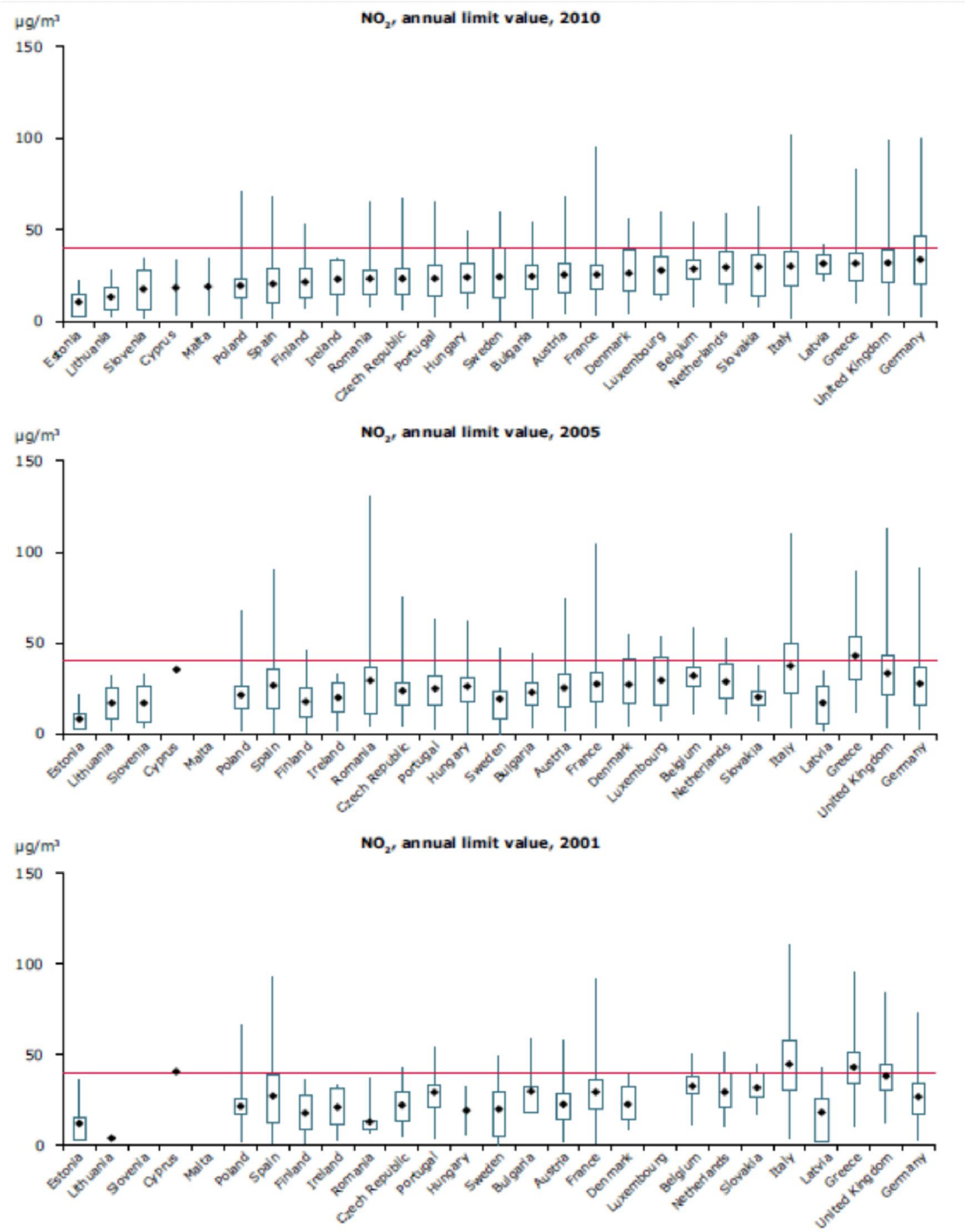

Note: The graphs are based on the annual mean concentration values; they present the range of concentrations at all station types (in µg/m^3) officially reported by the EU Member States and how the concentrations relate to the limit value set by EU legislation (marked by the red line).

The diagram indicates the lowest and highest observations, the means and the lower and upper quartiles. The lower quartile splits the lowest 25 % of the data and the upper quartile splits the highest 25 % of the data.

Source: ETC/ACM (The European Environment Agency's Topic Centre for Air and Climate Change Mitigation).

Fig.2.4: Attainment situation for NO_2, reference years 2010, 2005, 2001.

2.5.3. Distance to target

While the annual limit value is exceeded at only a very few rural background stations, it is exceeded at 4% of all urban background stations. The annual limit value is identical to the WHO AQG value. Exceedance of the limit value was reported at 44% of traffic stations, with a maximum observed concentration of 102 $\mu g/m^3$ in 2010, i.e. 2.5 times the threshold.

It clearly indicates that exceedance of the annual limit value and the WHO AQG value was observed in most EU Member States at one or more stations in 2010, with only Cyprus, Estonia, Ireland, Latvia, Malta, and Slovenia, in attainment. The only countries, with complete NO_2 data for the years 2001, 2005 and 2010, which did not register an exceedance of the NO_2 annual limit value in any of the three years were Estonia, Ireland and Latvia.

The hourly limit value threshold for NO_2 is less stringent. About 0.4 % of urban background stations reported exceedances and 4 % of traffic stations.

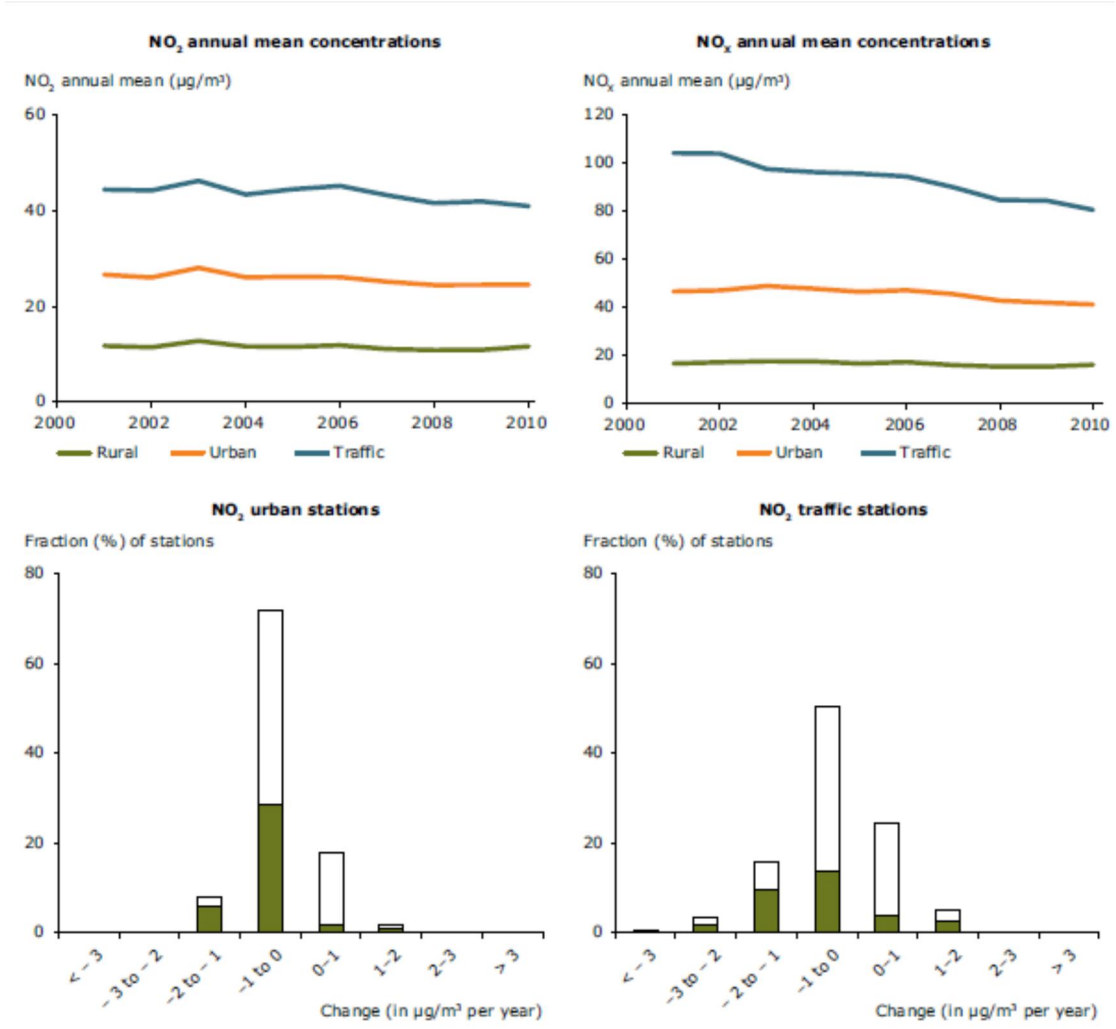

Note: All stations in EU Member States, with at least 75% data coverage for at least eight years were included in the analysis. Concentrations per station type are given in µg/m^3. In the top two diagrams a geographical bias exists towards central Europe where there is a higher density of stations.

In the percentage frequency distribution graphs, closed bars denote stations showing a statistically significant trend, open bars denote stations with a non-significant trend. Statistically significant trends (level of significance 0.1) are calculated by applying the Mann-Kendall test. The applied method is described in de Leeuw, 2012 [15].

Source: ETC/ACM.

Fig.2. 5: Trend in NO_2 and NO_X annual mean concentrations (2001–2010) per station type (top); percentage frequency distribution of estimated annual change of NO_2 annual mean concentrations at urban stations and at traffic stations (bottom)

These findings demonstrate that NO_2 concentrations must be reduced substantially in large areas of Europe (focusing on traffic and urban locations) for the annual limit value to be met. Exceedances of this objective are rather persistent: 12% of the stations operational in the period 2006–2010 in the EU showed exceedances each year. Similar figure 2.s were found in the period 2005–2009. The long-lasting exceedances are mostly observed at traffic stations [15].

2.5.4. Trends in NO_2 and NO_X concentrations

The trends in NO_2 and NO_X concentrations over the period 2001–2010 are summarized in Fig.2. 5, 6. A consistent set of stations is used for both NO_2 and NO_X but the distribution of the stations differs, therefore influencing the comparison. The concentration time series in Figure 2. 4 show slightly decreasing NO_2 annual mean concentrations at all station types, with the exception of NO_2 concentrations at rural sites. The proportional fall in NO_X is larger than the reduction in NO_2, attributed to the increase in primary NO_2 emissions from diesel vehicles and the shift in the photostationary state [14].

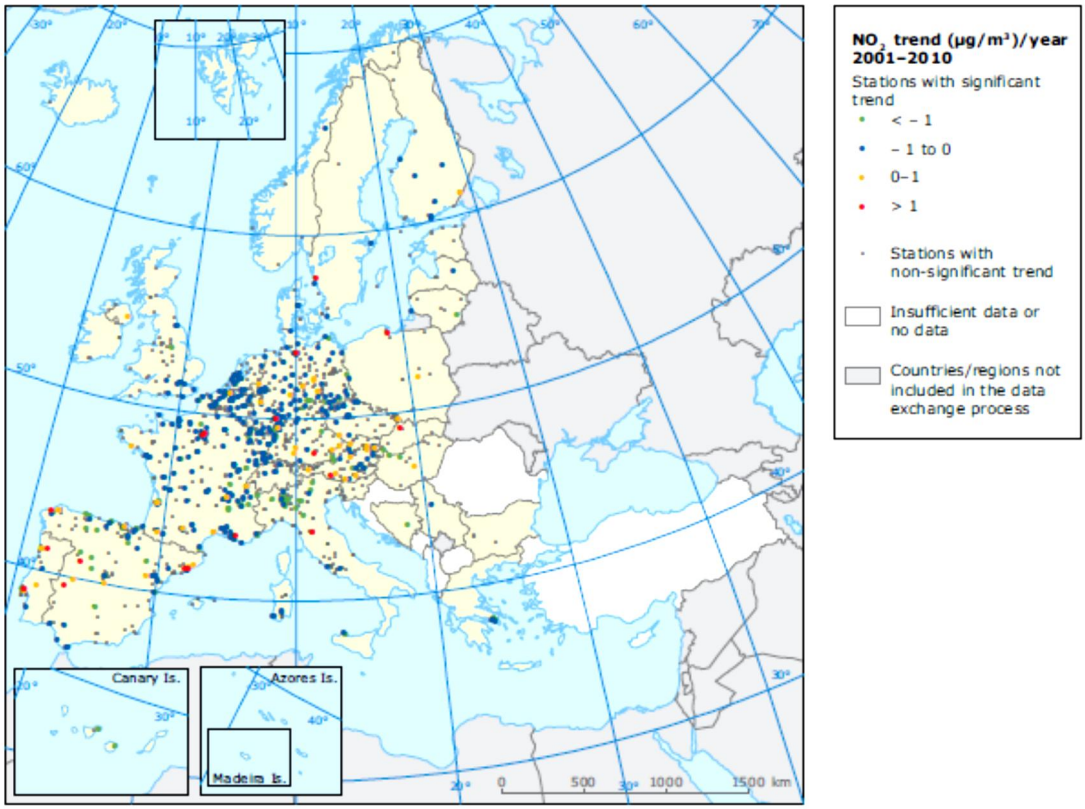

Note: Statistically significant trends (level of significance 0.1) are calculated by applying the Mann-Kendall test. The trend slopes are indicated with coloured dots when statistically significant. Red dots indicate increasing concentrations. The applied method is described in de Leeuw, 2012 [15].

Source: de Leeuw, 2012 [15].

Figure 2.6: Changes in annual mean concentrations of NO_2 in the period 2001–2010

2.5.5. NO_X emissions

As shown in Figure 2. 6, EU emissions of NO_X fell by 26 % in the period 2001–2010 and by 1.4 % from 2009 to 2010. Nevertheless, total NO_X emissions in 2010 were about 10% higher than the emissions ceiling for the EU as a whole set in the NEC Directive for 2010 [16].

Transport is the dominant sector for NO_X emissions, accounting for 48% of the total in 2010, followed by the energy sector, which contributed 20% of the total (Figure 2. 2.7). These two sectors have substantially reduced emissions since 2001. Over the period 2001–2010 emissions from transport decreased by 27% and from industry by 19%, while emissions from the energy sector decreased by 17%. The commercial, institutional and households' fuel combustion sector as well as the agriculture sector have decreased their NO_X emissions by only 6% in the same period.

Actual emissions from vehicles (often termed 'real world emissions') may exceed the allowed test cycle emissions specified in the Euro emission standards for each vehicle type. This is particularly the case for NO_X emissions from light-duty diesel vehicles. EU Member States regularly update the emission factors used in their emission inventories and their previously reported emissions. Reported developments in emissions should therefore include 'real world' emission factors.

2.5.6. Relationship of NO_X emissions and NO_2 concentrations

Nitrogen oxides emissions primarily comprise NO but also include some directly emitted NO_2, which countries are not currently required to report as a separate compound under the relevant EU legislation (EU, 2001b). The concentrations of NO_2 found in air originate both from directly emitted NO_2 and from chemical reactions forming NO_2 in the atmosphere, predominantly between NO and O_3.

An EEA analysis of source apportionment in the notifications submitted by sixteen EU Member States for time extension of NO_2 limit values shows that the urban and local traffic contribution to NO_2 levels measured at 74 urban traffic sites averages at 64%, ranging from 33% (Essen) to 91% (Catania). The higher fraction of NO_2 in NO_X

emissions from diesel vehicles could lead to increased NO_2 concentrations in traffic exposed areas and possibly also in urban areas in general.

The time series and frequency distributions in Figure 2. 5 show the differing trends in NO_2 concentrations recorded at rural, urban and traffic stations. At urban background locations the situation is relatively clear: the NO_2 levels are decreasing at 92% of the stations registering a trend. At traffic locations, NO_2 concentrations are decreasing at fewer stations (80% of traffic stations registering a trend). These trends reflect the increase in the share of NO_2 in the NO_X emissions from traffic and the shift in the photostationary state in favour of NO_2 that results from a decrease in NO_X, without an equivalent decrease in O_3 concentrations [14]. These are probably also the main reasons for the much lower average decrease in NO_2 concentrations measured over Europe (8% decrease measured at stations closed to traffic) (see Figure 2. 4) than the decrease in NO_X transport emissions (27% decrease in the EU) between 2001 and 2010.

Fig.2.6 shows the spatial distribution of NO_2 trends at station locations between 2001 and 2010, based on the same data and trend analysis as presented in Figure 2. 4.3. Although some countries have clusters of stations reporting an upward trend (e.g. Austria), most regions have stations with both upward and downward trends with the latter dominating. It is important to note that the number of stations with data covering the period 2001 to 2010 is very low in some parts of Europe, notably in parts of Eastern Europe and Scandinavia [11].

2.6. Exposure to NO_2 pollution in Europe

2.6.1. Human exposure

The NO_2 monitoring data in AirBase provide the basis for estimating the exposure of the European population to exceedances of the NO_2 annual mean limit value of 40 $\mu g/m^3$. Figure 2. 5 presents the data for the period 2001–2010, based on NO_2 measured at urban background monitoring stations. For each city an average concentration is calculated. It is considered that the whole population is exposed to these concentrations, since people move freely within the city. Close to traffic people are in reality exposed to higher NO_2 concentrations than in the urban background. This renders an underestimation of the estimated impact of exposure. According to this method, about 7% of the EU and EEA-32 urban population was exposed to NO_2 above the annual limit value and the WHO AQG for NO_2 in 2010. Exposure above the limit value varied between 6% and 27 % since 2001, with same percentages estimated for the EEA-32. There is a decreasing trend over this period with a decrease also observed between 2009 and 2010. The range partly reflects variations caused by meteorology.

2.6.2. Exposure of ecosystems

Nitrogen compounds emitted as NO_X and NH_3 are now the principal acidifying components and also cause eutrophication in sensitive ecosystems. Eutrophication is enrichment with nutrients, here by airborne reactive nitrogen, which creates damage to the ecosystems. Acidification of ecosystems is in addition to NO_X and NH_3 caused by the SO_X emissions.

The acidification and eutrophication effects are estimated using the concept of 'critical load': the ecosystem's ability to absorb deposited atmospheric acidifying and eutrophying pollutants without negative effects on the natural environment.

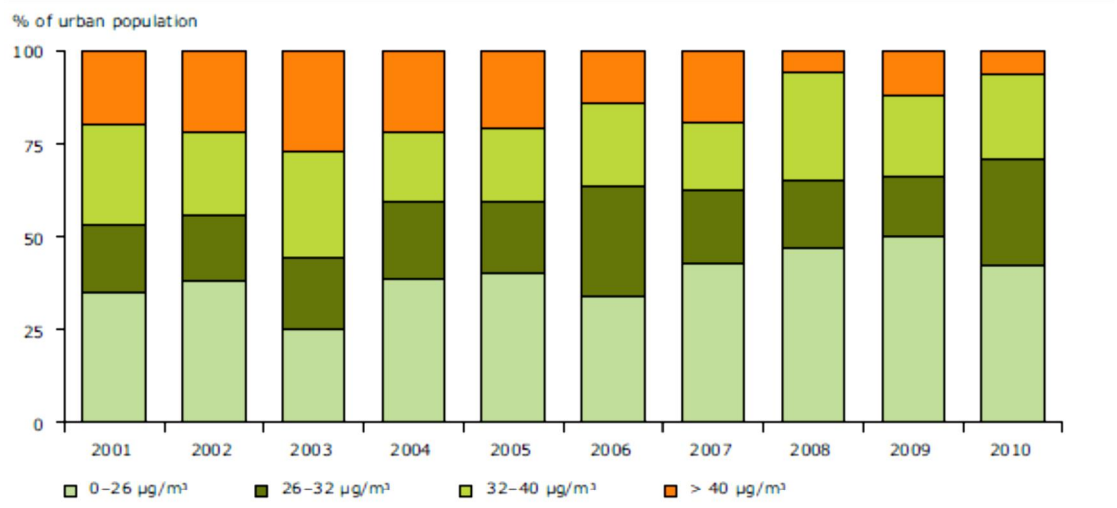

Source: EEA, 2012d (CSI 004).

Fig.2.7: Percentage of the EU urban population exposed to NO_2 concentration over the limit value set for protection of human health, 2001–2010.

Exceedances of spatially determined 'critical loads' present a risk of damage. Such exceedances are calculated based upon measurement data and model calculations. EEA showed calculated exceedances of critical loads for acidity and nutrient nitrogen in 2010. High exceedances of critical loads of acidity were evidenced in Belgium, at the north-west coast of France, the Netherlands and Poland. In the case of acidification, the situation has considerably improved and it is predicted to improve further. The area of sensitive ecosystems in Europe where the critical load of acidity is exceeded is estimated to have declined by more than 80% compared with the 1990 base year. This improvement is primarily attributed to heavily decreased SO_X emissions in the past two decades.

Concerning eutrophication, calculated exceedances for 2010 cover most of continental Europe as well as Ireland and southern areas of the United Kingdom and Sweden (EEA, 2010a). The risk of ecosystem eutrophication and its geographical coverage have diminished only slightly over the last decade and is still widespread over Europe. This conflicts with the EU's long-term objective of not exceeding critical loads of airborne acidifying and eutrophying substances in European ecosystem [11].

2.7. Responses

The most relevant EU legislative instruments addressing NO_X emissions and concentrations of NO_X and NO_2 relate to motor vehicle emissions (Euro emission standards) and emissions from combustion of fuel in industry and power production (the LCP " Large Combustion Plants Directive" and IPPC " The integrated pollution prevention and control directive" Directives). The legislation has resulted in an overall reduction of NO_X emissions. However, 'real-world emissions' of NO_X from diesel passenger cars have decreased very little over the last decade (both per-vehicle emissions and total emissions) and are considered to be the main driver of the exceedances of the NO_2 limit value found across the EU. The upcoming Euro 6 standard will focus on real-world emissions.

As explained above, concentrations of NO_2 in the atmosphere and at rural, urban and traffic locations originate partly from direct NO_2 emissions, and partly from NO emissions transformed into NO_2. A negative effect of some technologies used in diesel vehicles to meet the Euro emission limits is that the fraction of direct NO_2 emissions in total NO_X emissions is increasing [11].

2.8. Semiconducting metal oxides as environmentally hazardous gas sensors

The gas sensing properties of differently-prepared metal oxides and loaded metal oxides towards the environmentally hazardous gas NO_2 discussed in following subsections.

2.8.1. Nitrogen dioxide sensors

Sensors for NO_2 detection have been the most widely studied because NO_2 is regarded as the most dangerous gas. Table 2.3 shows a summary of NO_2 gas-sensing properties of loaded/unloaded metal oxide semiconductors. From most reported data, unloaded WO_3 is demonstrated as the most promising metal oxide for NO_2 gas sensing. Nevertheless, its performances considerably depend on its structure and preparation method. The structure of modern WO_3 gas sensors may be classified into two main types, thick/thin films and nanoparticles. Thick/thin WO_3 film gas sensors have been developed by many groups using various preparation methods. Following highlights important results achieved to date. WO_3 sensitive films fabricated by atmospheric plasma spraying technique with a heat-treatment gave the response of 77–450 ppb NO_2 at 130°C. In addition, the obtained WO_3 sensors were found to exhibit different sensing behaviors depending on operating temperature and NO_2 concentration. The electrical resistance of WO_3 sensor increased at low working temperature and high NO_2 concentration in humid air. On the other hand, the resistance decreased when NO_2 concentration was lower than 93 ppb and the working temperature was higher than 130°C. The deposition of WO_3 thin films using reactive direct current magnetron sputtering with different discharge gas pressures has been reported [17]. Gas sensing properties of WO_3 thin films in reaction to 1 ppm NO_2 gas and 1000 ppm H_2 gas were investigated at operating temperature in the range of 50 to

300°C. The peak response for NO_2 was found to be 460 at 200°C. A simple and cost effective electrostatic spray deposition technique for the fabrication of WO_3 films to detect different pollutant gases has been presented [18]. The films obtained from tungsten ethoxide as precursor produced good quality films in terms of microstructure and morphology. The films were able to detect very small amount of NO_2 (less than 1 ppm) at low operating temperature (150°C). However, the sensor could be easily interfered by H_2S: the films were highly sensitive to low H_2S concentrations (10 ppm) at low operating temperature of 200°C. The sensing films had relative selectivity to H_2S in the presence of other gases (20 ppm SO_2 and 1 ppm NO_2). NO_2 sensors based on WO_3 nanoparticles have recently gained much attention and been reported by several researchers. Tungsten oxide nanoparticles were synthesized and characterized using high resolution TEM [19]. The material was deposited on patterned alumina substrates through low frequency AC electrophoresis and used as NO_2 sensor, presenting a stable device sensitive to NO_2 in a dilute range. The highest response was 50-500 ppb at 200°C. However, a lower response was seen at higher temperature due to decreased adsorption at those temperatures. WO_3 nanoparticles using gas evaporation method with tungsten filament under low pressure of oxygen gas has been prepared [20]. With gas sensor made of WO_3 nanoparticles smaller than 100 nm, the highest response to 1 ppm NO_2 was 4700 at 50°C. The response of unloaded WO_3 nanoparticles to ppb level of NO_2 was also reported [19, 21], which were relatively lower than Meng's report [20]. Thus, WO_3 nanoparticles prepared by gas evaporation method represent the best NO_2 reported to date [22].

Table 2.3: A summary on the gas sensing properties of unloaded/loaded metal oxide semiconductors for NO_2 gas.

Sensing material	**Method**	**Gas concentration**	**Sensing performance**	**Reference**
Unloaded WO_3 nanorods/microspheres	Hydrothermal	20 ppm	Response: 525 to 20 ppm at 350°C	[23]
Unloaded WO_3	Low frequency AC Electrophoretic deposition	50-500 ppb	Response: 50 to 500 ppb at 200°C	[24]
Unloaded ZnO	DC magnetron reactive sputtering	5 ppm	Response: ~6 to 5 ppm at 300°C	[25]
Unloaded WO_3	Atmospheric plasma spraying	0-450 ppb	Response: 77 to 450 ppb at 130°C	[26]
Unloaded WO_3	Evaporation of W filament	1 ppm	Response: 4700 to 1 ppm at 50°C	[27]
Unloaded WO_3	Reactive magnetron direct current sputtering	1 ppm	Response: ~460 to 1 ppm at 200°C	[28]
Unloaded WO_3	Electrostatic spray	0.25 – 1 ppm	Response: 30	[29]

	deposition		to 1 ppm at 150°C	
1.67 wt% Pd/TiO_2	Calcination of electrospun PVP/TiO2/Pd composite	0.8 – 2.8 ppm	Response: 28 to 2.1 ppm NO_2 at 180°C	[30]
Unloaded ZnO	Hydrothermal	1 ppm	Response: ~1.8 to 1 ppm at 300°C	[31]
0.11 and 15 wt% WO_3/TiO_2	Screen-printing	0 – 300 ppm	Response: 145 (15% WO_3) to 500 ppm at 180°C	[32]

Apart from WO_3, ZnO is another potential candidate for NO_2 sensing. Baratto et al. [33] reported the gas sensing properties of ZnO nanopowders synthesized by an aerosol method. Two different nanopowder morphologies, fibre-mats and cauliflower, were obtained. Both sensors showed high response against sub-ppm concentration of NO_2 at low operating temperature. At 100°C, the fibre nanopowder showed a high response of 50 towards 0.4 ppm of NO_2, while that of cauliflower nanopowder was 8. The fibre-mats nanopowder sensor could detect 0.1 ppm of NO_2 with a relative response of 3 with no interference from CO or ethanol, which could be due to low

working temperature. Tamaekong et al. [34] reported the synthesis of unloaded ZnO by flame spray pyrolysis (FSP) for NO_2 sensing at 1, 5 and 10 ppm with response of 2.7, 6.2 and 11.8 respectively. Unloaded ZnO and Nb/ZnO nanoparticles containing 0.25, 0.5 and 1 mol% Nb were produced in a single step by FSP [35].The influence on a low dynamic range of Nb concentration on NO_2 response (0.1–4 ppm) of thick film sensor elements was studied at the operating temperatures ranging from 250–350◦C in the presence of dry air. The optimum Nb concentration was found to be 0.5 and 0.5 mol% Nb exhibited an optimum NO_2 response of ∼1640 and a very fast response time (27 s) for NO_2 concentration of 4 ppm at 300◦C. Another approach for the enhancement of gas-sensing especially towards NO_2 can be achieved by the use of organic materials.

For instance, ZnO nanowire incorporated with poly (3-hexylthiophene) (P3HT) by Saxena was reported to exhibit enhanced NO_2 selectivity, which could be attributed to the reduction of the organic materials by the metal oxide semiconductors [22].

References

1. C.K. Varshney and S. Abhai Pratap, Passive Samplers for NO_X Monitoring: A Critical Review, the Environmentalist, 23 (2003) 127–136.
2. Air pollution in Europe 1990–2004, EU air quality directive 2001/81/CE.
3. World Health Organization, Regional Office for Europe, Copenhagen, Denmark, Nitrogen dioxides Chapter 7.1 , Air Quality Guidelines - Second Edition, 2000.
4. A. P. Altshuller, Thermodynamic considerations in the interactions of nitrogen oxides and oxy-acids in the atmosphere. Journal of the Air Pollution Control Association, 6 (1956) 97–100.
5. Air quality criteria for oxides of nitrogen. Research Triangle Park, NC, US Environmental Protection Agency 1993 (EPA Report No. EPA/600/8-91/049aF-cF. 3v).
6. Health risk evaluation of nitrogen oxides. Scandinavian journal of work, environment and health, 19 (Suppl. 2) (1993).
7. Advisory group on the medical aspects of air pollution episodes. Third report: oxides of nitrogen. London, H.M. Stationery Office, 1993.
8. Quality of Urban air review group. Urban air quality in the United Kingdom. London, Department of the Environment, 1993.
9. Air quality and health - Fact sheet no 313 - Updated August 2008 (http://www.who.int/mediacentre/ factsheets/fs313/en/) , 8 July 2012.
10. The European environment state and outlook 2010, European Environment Agency (http://www.eea. europa.eu/soer) , 05 July 2012.
11. Air quality in Europe — EEA Report No 4/2012, 104 pp., ISBN 978-92-9213-328-3, doi: 10.2800/55823.

12. Air quality guidelines - global update 2005, World Health Organization Regional Office for Europe, Copenhagen.
13. Directive 2008/50/EC of the European Parliament and of the Council of 21 May 2008 on ambient air quality and cleaner air for Europe (OJ L 152, 11.6.2008, p. 1–44) .
14. C. Guerreiro, J. Horálek, F. de Leeuw, C. Hak, , C. Nagl, , P. Kurfürst and J. Ostatnicka, Status and trends of NO_2 ambient concentrations in Europe, ETC/ACC Technical (2010).
15. F. de Leeuw, AirBase: a valuable tool in air quality assessments at a European and local level, ETC/ACM Technical (2012).
16. Directive 2001/81/EC of the European Parliament and of the Council of 23 October 2001 on national emission ceilings for certain atmospheric pollutants (OJ L 309, 27.11.2001, p. 22-30) .
17. Y. Shen, T. Yamazaki, Z. Liu, D. Meng, T. Kikuta and N. Nakatani, Influence of effective surface area on gas sensing properties of WO_3 sputtered thin films, Thin Solid Films, 517 (2009) 2069–2072.
18. C. M. Ghimbeu, M. Lumbreras, M. Siadat and J. Schoonman, Detection of H_2S, SO_2, and NO_2 using electrostatic sprayed tungsten oxide films, Mater. Sci. Semiconduct. Proc., 13 (2010) 1–8.
19. E. K. Heidari, C. Zamani, E. Marzbanrad, B. Raissi and S. Nazarpour, WO_3-based NO_2 sensors fabricated through low frequency AC electrophoretic deposition, Sens. Actuators B: Chem., 146 (2010) 165–170.
20. D. Meng, T. Yamazaki, Y. Shen, Z. Liu and T. Kikuta, Preparation of WO_3 nanoparticles and application to NO_2 sensor, Appl. Surf. Sci., 256 (2009) 1050–1053.

21. C. Zhang, M. Debliquy, A. Boudiba, H. Liao and C. Coddet, Sensing properties of atmospheric plasma-sprayed WO_3 coating for sub-ppm NO_2 detection, Sens. Actuators B: Chem., 144 (2010) 280–288.

22. K. Wetchakun, T. Samerjai, N. Tamaekong, C. Liewhiran, C. Siriwong, V. Kruefu, A. Wisitsoraat, A. Tuantranont and S. Phanichphant, Semiconducting metal oxides as sensors for environmentally hazardous gases, Sensors and Actuators B, 160 (2011) 580– 591.

23. Z. Liu, M. Myauci, T. Yamazaki and Y. Shen, Facile synthesis and NO_2 gas sensing of tungsten oxide nanorods assembled microspheres, Sens. Actuators B: Chem., 140 (2009) 514‑519.

24. E. K. Heidari, C. Zamani, E. Marzbanrad, B. Raissi and S. Nazarpour, WO_3-based NO_2 sensors fabricated through low frequency AC electrophoretic deposition, Sens. Actuators B: Chem. 146 (2010) 165‑170.

25. Y. Min, H. L. Tuller, S. Palzer, J.W. llenstein and H. Bo, Gas response of reactively sputtered ZnO films on Si-based micro-array, Sens. Actuators B: Chem., 93 (2003) 435‑441.

26. C. Zhang, M. Debliquy, A. Boudiba, H. Liao and C. Coddet, Sensing properties of atmospheric plasma-sprayed WO_3 coating for sub-ppm NO_2 detection, Sens. Actuators B: Chem. 144 (2010) 280‑288.

27. D. Meng, T. Yamazaki, Y. Shen, Z. Liu and T. Kikuta, Preparation of WO_3 nanoparticles and application to NO_2 sensor, Appl. Surf. Sci., 256 (2009) 1050‑1053.

28. Y. Shen, T. Yamazaki, Z. Liu, D. Meng, T. Kikuta and N. Nakatani, Influence of effective surface area on gas sensing properties of WO_3 sputtered thin films, Thin Solid Films, 517 (2009) 2069‑2072.

29. C.M. Ghimbeu, M. Lumbreras, M. Siadat and J. Schoonman, Detection of H_2S, SO_2, and NO_2 using electrostatic sprayed tungsten oxide films, Mater. Sci. Semiconduct. Proc. 13 (2010) 1–8.

30. J. Moon, J. A. Park, S. J. Lee, T. Zyung and I. D. Kim, Pd-doped TiO_2 nanofibers networks for gas sensor applications, Sens. Actuators B: Chem., 149 (2010) 301–305.

31. P. S. Cho, K. W. Kim and J. H. Lee, NO_2 sensing characteristics of ZnO nanorods prepared by hydrothermal method, J. Electroceram., 17 (2006) 975–978.

32. S. U. Jo, B. G. Kang, S. Heo, S. Song and Y. J. Kim, Gas sensing properties of WO_3 doped rutile TiO_2 thick film at high operating temperature, Curr. Appl. Phys. 9 (2009) e235–e238.

33. C. Baratto, G. Sberveglieri, A. Onischuk, B. Caruso and S. d. Stasio, Low temperature selective NO_2 sensors by nanostructured fibres of ZnO, Sens. Actuators B: Chem. 100 (2004) 261–265.

34. N. Tamaekong, C. Liewhiran, A. Wisitsoraat and S. Phanichphant, Flame-spraymade unloaded zinc oxide film for gas sensing applications, sensors, 10 (2010) 7863–7873.

35. V. Kruefu, C. Liewhiran, A. Wisitsoraat and S. Phanichphant, Selectivity of flamespray- made Nb/ZnO thick films towards NO_2 gas, Sens. Actuators B: Chem., 156 (2011) 360–367.

Chapter 3 - Clays and sepiolite

3.1. Introduction

Sepiolite is a kind of clay minerals,an important group of hydrous aluminum silicates with a layer (sheetlike) structure and very small particle size. They may contain significant amounts of iron, alkali metals, or alkaline earths.

The term clay is generally applied to (1) a natural material with plastic properties, (2) particles of very fine size, customarily those defined as particles smaller than two micrometres, and (3) very fine mineral fragments or particles composed mostly of hydrous-layer silicates of aluminum, though occasionally containing magnesium and iron. Although, in a broader sense, clay minerals can include virtually any mineral of the above-cited particle size, the definition adapted here is restricted to represent hydrous-layer silicates and some related short-range ordered alumino-silicates, both of which occur either exclusively or frequently in very fine-size grades. [1]

The development of X-ray diffraction techniques in the 1920s and the subsequent improvement of microscopic and thermal procedures enabled investigators to establish that clays are composed of a few groups of crystalline minerals. The introduction of electron microscopic methods proved very useful in determining the characteristic shape and size of clay minerals. More recent analytical techniques such as infrared spectroscopy, neutron diffraction analysis, Mössbauer spectroscopy, and nuclear magnetic resonance spectroscopy have helped advance scientific knowledge of the crystal chemistry of these minerals.

Clay minerals are composed essentially of silica, alumina or magnesia or both, and water, but iron substitutes for aluminum and magnesium in varying degrees, and appreciable quantities of potassium, sodium, and calcium are frequently present as well. Some clay minerals may be expressed using ideal chemical formulas as the

following: $2SiO_2.Al_2O_3.2H_2O$ (kaolinite), $4SiO_2.Al_2O_3.H_2O$ (pyrophyllite), $4SiO_2.3MgO.H_2O$ (talc), and $3SiO_2.Al_2O_3.5FeO.4H_2O$ (chamosite). The SiO_2 ratio in a formula is the key factor determining clay mineral types. These minerals can be classified on the basis of variations of chemical composition and atomic structure into nine groups: (1) kaolin-serpentine (kaolinite, halloysite, lizardite, chrysotile), (2) pyrophyllite-talc, (3) mica (illite,glauconite, celadonite), (4) vermiculite, (5) smectite (montmorillonite, nontronite, saponite), (6) chlorite (sudoite, clinochlore, chamosite), (7) sepiolite-palygorskite, (8) interstratified clay minerals (e.g., rectorite, corrensite, tosudite), and (9) allophane-imogolite. [1]

Kaolinite is derived from the commonly used name kaolin, which is a corruption of the Chinese Gaoling (Pinyin; Wade-Giles: Kao-ling) meaning “high ridge,” the name of a hill near Ching-te-chen where the occurrence of the mineral is known as early as the 2nd century BC. Montmorillonite and nontronite are named after the localities Montmorillon and Nontron, respectively, in France, where these minerals were first reported. Celadonite is from the French céladon (meaning grayish yellow-green) in allusion to its colour. Because sepiolite is a light and porous material, its name is based on the Greek word for cuttlefish, the bone of which is similar in nature. The name saponite is derived from the Latin sapon (meaning soap), owing to its appearance and cleaning ability. Vermiculite is from the Latin vermiculari (“to breed worms”), because of its physical characteristic of exfoliation upon heating, which causes the mineral to exhibit a spectacular volume change from small grains to long wormlike threads. Baileychlore, brindleyite, corrensite, sudoite, and tosudite are examples of clay minerals that were named after distinguished clay mineralogists—Sturges W. Bailey, George W. Brindley, Carl W. Correns, and Toshio Sudō, respectively [1].

Sepiolite and attapulgite naturally occur in soils, in sedimentary "clay deposits," and are alteration products of certain basic igneous rocks, and they are not uncommon as minor constituents of many sedimentary rocks. The literature, however, presents an ambiguous picture of the genesis of these minerals. Their presence is often reported, but detailed descriptions of their relation to accompanying minerals are frequently missing. Although both minerals are found in similar environments, the presence of both in the same deposit is not common [2].

Lapparent (1936) states that sepiolite is formed by the action of magnesium-rich solutions upon siliceous gels in the presence of lime. Longchambon (1935) attributes the origin of palygorskite to the alteration of pyroxenes and amphiboles, while Kerr (1937) suggests that the attapulgite from Georgia was formed by the alteration of montmorillonite minerals. Caillere and Henin (1949) have said that certain sepiolites are secondary products resulting from the weathering of enclosing serpentine bodies. Sepiolite, resembling metacolloidal asbestos, has been reported by Serdyuchenko (1949) to occur in silicified serpentinites accompanied by veinlets of quartz, opal, and calcite, replacing older carbonate host rock. Gerasimov, Grushko, and Chirvinsky (1949) state that palygorskite has been found as a fibrous vein mineral in cellular limestones and dolomites. Both fibrous and lamellar sepiolite was reported from solution cavities in a Madagascar limestone (LaCroix, 1940). 60 years ago, Heystek and Schmidt (1953) suggested that in the progressive weathering of a basalt, it alters first to montmorillonite and then to attapulgite. The amount of attapulgite in any one weathering zone of this basalt can be correlated roughly with the quantity of carbonate present.

From these reports a further question may he raised: if the sepiolite and attapulgite grains in certain sediments are not detrital, why should Mg^{2+}, SiO_4^{2-}, etc., have

combined to form sepiolite (or attapulgite) rather than a montmorillonite or talc? This problem is accentuated by the inability to synthesize sepiolite or attapulgite [2].

Sepiolite requires alkaline conditions and high Si and Mg activities for stability (Singer, 1989). Most major deposits were originally formed in shallow seas and lakes as chemical sediments or by the reconstitution of smectites, in open oceans by the hydrothermal alteration of volcanic materials, and in calcareous soils by direct crystallization (Callen, 1984).

That's why we could find it near to oceans, seas and volcanic places as we can see in Fig.3. 1 [2]. Sepiolite is known from many localities, but not in large amounts. A few localities affording good material include: from antiquity, at Eskishehir, in Turkey, from Vallecas, near Madrid, and Cabanas, near Toledo, in Spain, at Nugssuaq, in western Greenland, n the USA, from Middletown, Delaware Co., Pennsylvania, at Gouverneur, St. Lawrence Co., New York, in Little Cottonwood Canyon, Salt Lake Co., Utah, from Crestmore, Riverside Co., California, on the southern High Plains, from Amarillo, Texas to Hobbs, New Mexico, at Ash Meadows, Nye Co., Nevada, from Cerro Mercado, Durango, in Mexico, from near Lake Amboseli, in Kenya, at Lake Natron, in Tanzania, from Ampandrandava, in Madagascar and at Kuzuu, Tochigi Prefecture, in Japan [3].

Fig.3.1: Map shows the distribution of Sepiolite sedimentation all over the world [4]

Owing to its absorptive properties, sepiolite is used commercially as carriers, fillers, clarifying agents, and in used lubricant reclamation.

It has been previously shown that several silicates, including sepiolite, have different industrial applications when modified chemically or thermally [5].

3.2. Sepiolite structure

Sepiolite is a papyrus-like or fibrous hydrated magnesium silicate mineral and is included in the phyllosilicate group because it contains a continuous two-dimensional tetrahedral sheet of composition Si_2O_5. It differs, however, from the other layer silicates because it lacks continuous octahedral sheets.

The structure of sepiolite can be regarded as consisting of narrow strips or ribbons of 2:1 layers that are linked stepwise at the corners. One ribbon is linked to the next by inversion of the direction of the apical oxygen atoms of SiO_4 tetrahedrons; in other

words, an elongated rectangular box consisting of continuous 2:1 layers is attached to the nearest boxes at their elongated corner edges. Therefore, channels or tunnels due to the absence of the silicate layers occur on the elongated sides of the boxes. The elongation of the structural element is related to the fibrous morphology of the minerals and is parallel to the axis.

Since the octahedral sheet is discontinuous, some octahedral magnesium ions are exposed at the edges and hold bound water molecules (H_2O). In addition to the bound water, variable amounts of zeolitic (i.e., free) water (H_2O) are contained in the rectangular channels. The width of the ribbons in sepiolite is great. The width determines the number of octahedral cation positions per formula unit. Thus, sepiolite has an ideal composition $Mg_8Si_{12}O_{30}(OH)_4(OH_2)_4(H_2O)_8$. [6]

Sepiolite has internal channels called “zeolitic channels” which run the length of its structure and open via pores of varying shapes and dimensions at the surface. Along the edges of the tetrahedral sheets are silanol ($SiOH_4$) groups which can readily hydrogen bond with water and other polar molecules. The magnesium layer also provides adsorption sites.

A highly porous mineral with low bulk density, sepiolite is an effective absorbent. At the same time, due to its rigid structure, sepiolite will not swell in the presence of water or other liquids. An approximate empirical formula for sepiolite is: $Si_{12}Mg_8O_{30}(OH)_4(OH_2)_4.8H_20$ [7].

The unit cell of the clay, shown in Figure 3. 2, has orthorhombic symmetry with lattice parameters a = 1.35 nm, b = 2.70 nm, and c = 0.53 nm [10]. Like palygorskite, rectangular channels forms parallel the c-axis of the unit cell and often contain zeolitic water or hydroxyl groups. A trivalent cation (Mn^{3+}, Al^{3+}, or Fe^{3+}) is often

found as a substitutional impurity occupying a silicon site in a tetrahedral sheet [8].

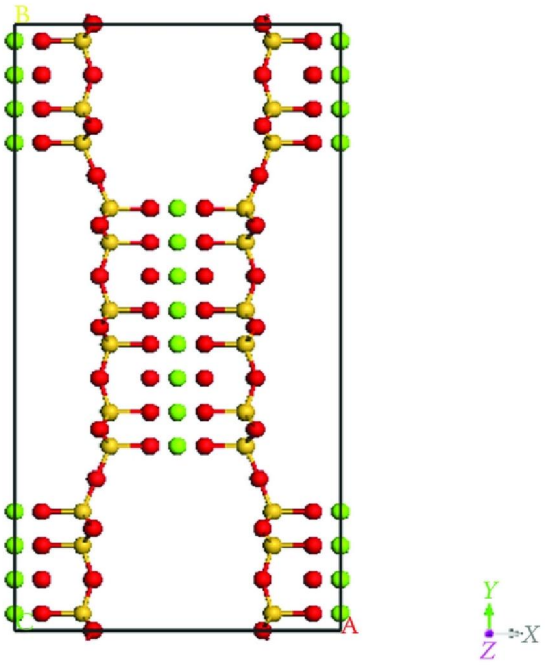

Fig.3.2: Unit cell of sepiolite, showing magnesium (green) octahedrally coordinated between chains of SiO_4 (silicon shown in orange, oxygen in white). View is along the c-axis [8].

Clay materials contain water in several forms. The water may be held in pores and may be removed by drying under ambient conditions. Water also may be adsorbed on the surface of clay mineral structures and in smectites, vermiculites, hydrated halloysite, sepiolite, and palygorskite; this water may occur in interlayer positions or within structural channels. Finally, the clay mineral structures contain hydroxyls that are lost as water at elevated temperatures.

The water adsorbed between layers or in structural channels may further be divided into zeolitic and bound waters. The latter is bound to exchangeable cations or directly to the clay mineral surfaces. Both forms of water may be removed by heating to temperatures on the order of 100°–200°C and in most cases, except for hydrated

halloysite, are regained readily at ordinary temperatures. It is generally agreed that the bound water has a structure other than that of liquid water; its structure is most likely that of ice. As the thickness of the adsorbed water increases outward from the surface and extends beyond the bound water, the nature of the water changes either abruptly or gradually to that of liquid water. Ions and molecules adsorbed on the clay mineral surface exert a major influence on the thickness of the adsorbed water layers and on the nature of this water. The non liquid water may extend out from the clay mineral surfaces as much as 6–10 nm.

Hydroxyl ions are driven off by heating clay minerals to temperatures of 400°–700°C. The rate of loss of the hydroxyls and the energy required for their removal are specific properties characteristic of the various clay minerals. This dehydroxylation process results in the oxidation of Fe^{2+} to Fe^{3+} in ferrous-iron-bearing clay minerals. The water-retention capacity of clay minerals is generally proportional to their surface area (see Table 3.1).

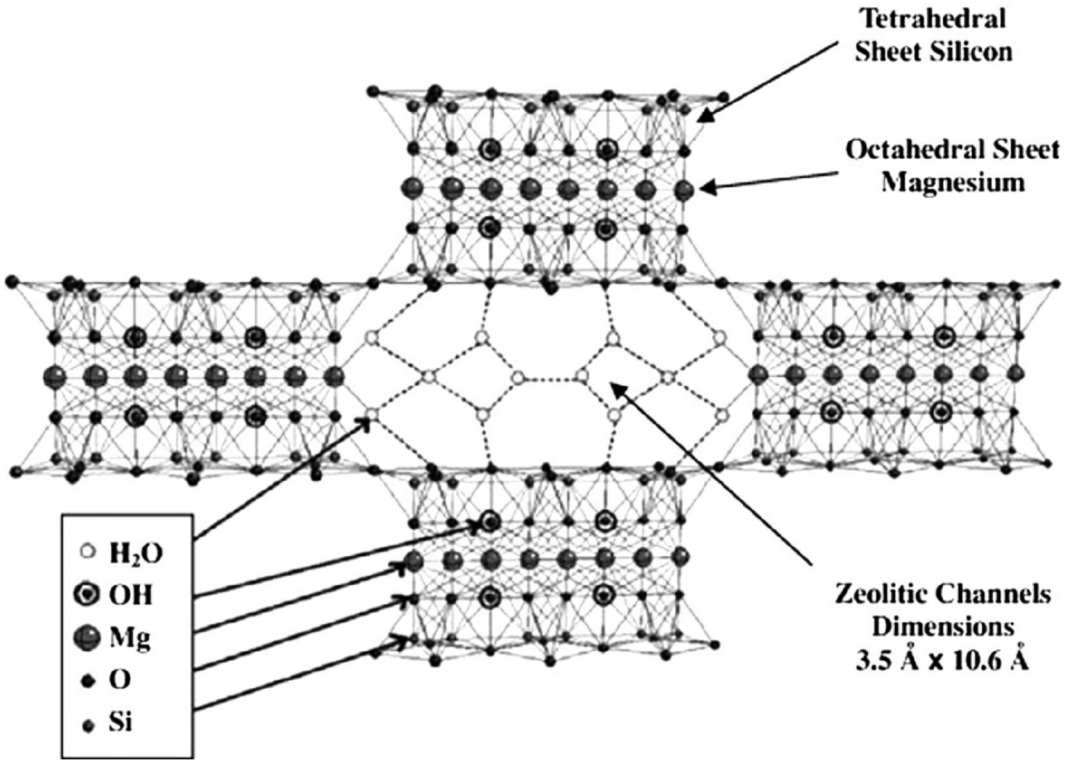

Fig.3.3: Schematic representation of the sepiolite structure [9].

3.3. Ion exchange

Depending on deficiency in the positive or negative charge balance (locally or overall) of mineral structures, clay minerals are able to adsorb certain cations and anions and retain them around the outside of the structural unit in an exchangeable state, generally without affecting the basic silicate structure. These adsorbed ions are easily exchanged by other ions. The exchange reaction differs from simple sorption because it has a quantitative relationship between reacting ions. The range of the cation-exchange capacities of the clay minerals is given in the Table 3.1.

Table 3.1: Cation-exchange capacities and specific surface areas of clay minerals

Mineral	**Cation-exchange capacity at pH 7 (milliequivalents per 100 grams)**	**Specific surface area (square metre per gram)**
kaolinite	3–15	5–40
halloysite (hydrated)	40–50	1,100*
illite	10–40	10–100
chlorite	10–40	10–55
vermiculite	100–150	760*
smectite	80–120	40–800
palygorskite-sepiolite	3–20	40–180
allophane	30–135	2,200*
imogolite	20–30	1,540*

*Upper limit of estimated values.

Exchange capacities vary with particle size, perfection of crystallinity, and nature of the adsorbed ion; hence, a range of values exists for a given mineral rather than a single specific capacity. With certain clay minerals—such as imogolite, allophane, and to some extent kaolinite—that have hydroxyls at the surfaces of their structures,

exchange capacities also vary with the pH (index of acidity or alkalinity) of the medium, which greatly affects dissociation of the hydroxyls.

Under a given set of conditions, the various cations are not equally replaceable and do not have the same replacing power. Calcium, for example, will replace sodium more easily than sodium will replace calcium. Sizes of potassium and ammonium ions are similar, and the ions are fitted in the hexagonal cavities of the silicate layer. Vermiculite and vermiculitic minerals preferably and irreversibly adsorb these cations and fix them between the layers. Heavy metal ions such as copper, zinc, and lead are strongly attracted to the negatively charged sites on the surfaces of the 1:1 layer minerals, allophane and imogolite, which are caused by the dissociation of surface hydroxyls of these minerals.

The ion-exchange properties of the clay minerals are extremely important because they determine the physical characteristics and economic use of the minerals [1].

3.4. Clay-water relations

3.4.1. Solubility

The solubility of clay minerals in acids varies with the nature of the acid and its concentration, the acid-to-clay ratio, the temperature, the duration of treatment, and the chemical composition of the clay mineral attacked. In general, ferromagnesian clay minerals are more soluble in acids than their aluminian counterparts. Incongruent dissolutions may result from reactions in a low-acid-concentration medium where the acid first attacks the adsorbed or interlayer cations and then the components of the octahedral sheet of the clay mineral structure. When an acid of higher concentration is used, such stepwise reactions may not be recognizable, and the dissolution appears to be congruent. One of the important factors controlling the rate of dissolution is the

concentration in the aquatic medium of the elements extracted from the clay mineral. Higher concentration of an element in the solution hinders to a greater degree the extractions of the element.

In alkaline solutions, a cation-exchange reaction first takes place, and then the silica part of the structure is attacked. The reaction depends on the same variables as those stated for acid reactions [1].

3.4.2. High-temperature reactions

When heated at temperatures beyond dehydroxylation, the clay mineral structure may be destroyed or simply modified, depending on the composition and structure of the substance. In the presence of fluxes, such as iron or potassium, fusion may rapidly follow dehydroxylation. In the absence of such components, particularly for aluminous dioctahedral minerals, a succession of new phases may be formed at increasing temperatures prior to fusion. Information concerning high-temperature reactions is important for ceramic science and industry [2].

As already mentioned, sepiolite contains four different types of water molecules:

(i) Hygroscopic, (ii) zeolitic, (iii) bound and (iv) hydroxyl water. The most probable binding sites on the sepiolite surface are surface hydroxyls and Lewis acidic centers.

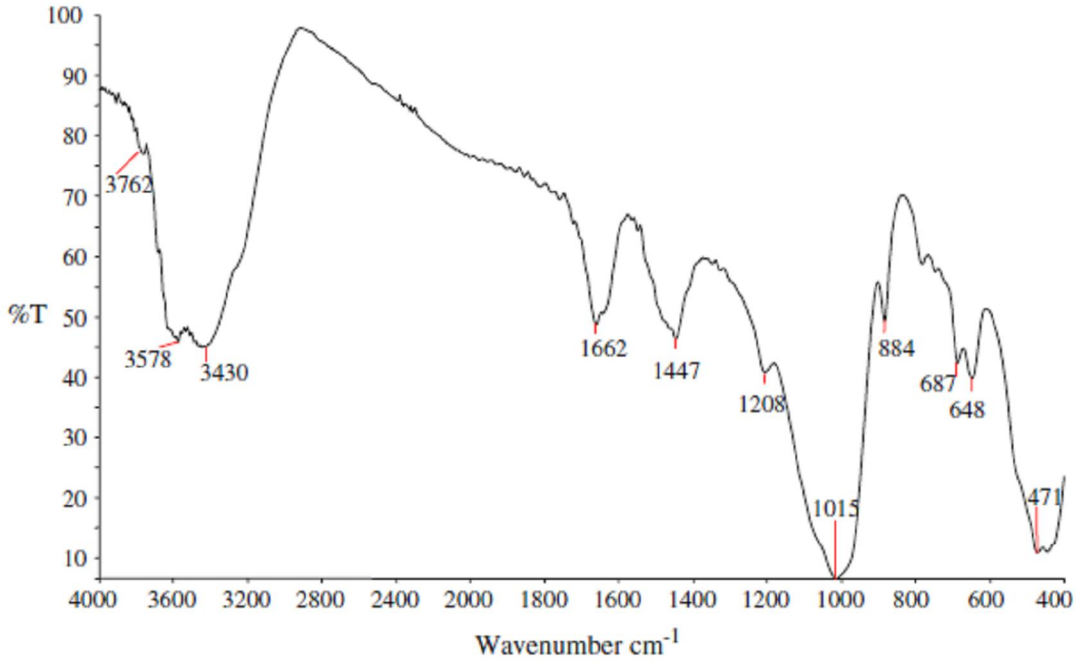

Fig.3.4: FTIR spectrum of sepiolite

FTIR spectrum of sepiolite sample is shown in Fig.3. 4. The Mg_3OH band at 3762–3578 cm^{-1} characterized by weak bonding strength is ascribed to the presence of OH groups in the octahedral sheet and the OH stretching vibration in the external surface of sepiolite. On the other hand, the 3430 and 1662 cm^{-1} bands are respectively assigned to the OH stretching, representing the zeolitic water in the channels and bound water coordinated to magnesium in the octahedral sheet. The band at 1447 cm^{-1} developed due to the hydroxyl bending vibration again reflects the presence of bound water.

The Si–O coordination bands at 1208 and 1015 cm^{-1} represent the stretching of Si–O in the Si–O–Si groups of the tetrahedral sheet [10].

IR spectra of untreated and heat treated sepiolites are reported in Fig.3. 5. Increasing the treatment temperature produced a decrease in the bands corresponding to OH groups (647, 689, 1625, 3500, 3700 cm^{-1}) of water bonded to magnesium ions in the octahedral layer of the sepiolite. On the other hand, the thermal treatment produces a

decrease in the intensity of the Si-O band at 1210 cm^{-1} which is typical of the tetrahedral layer of sepiolite. The higher temperature of treatment of the sepiolite produces more noticeable changes in the IR spectra. Therefore, the surface chemistry of the sepiolite is modified by thermal treatment [5].

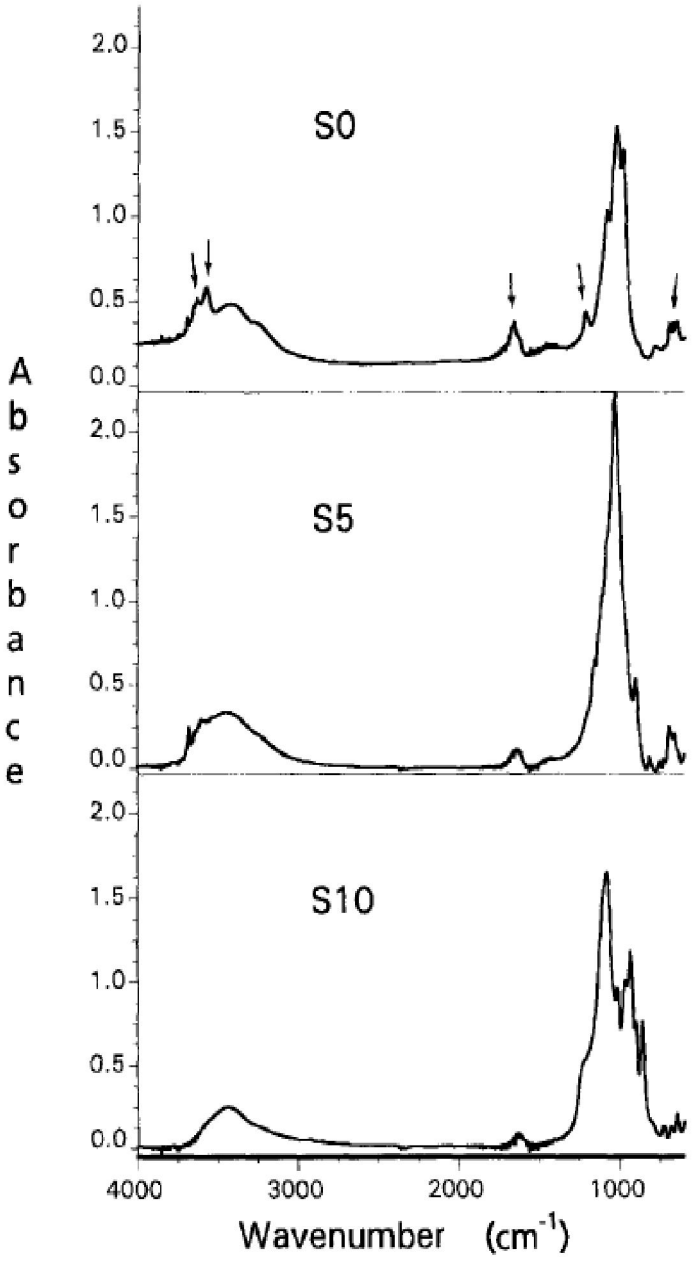

Fig.3.5: IR spectra of untreated sepiolite (SO), heat treated sepiolite at 550°C (S5) and heat treated sepiolite at 1000°C (S10)

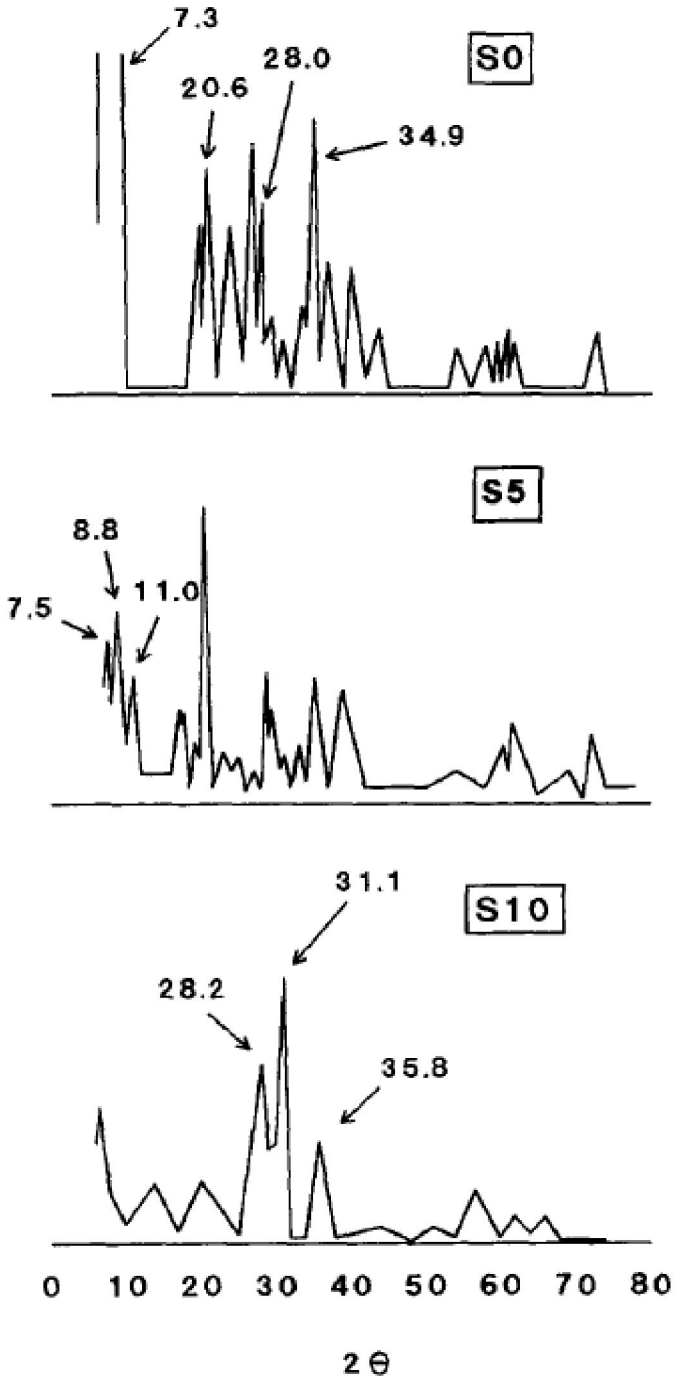

Fig.3.6: X-ray diffractograms of untreated sepiolite (SO), heat treated sepiolite at 550°C (S5) and heat treated sepiolite at 1000°C (S10)

Thermal treatment also modifies the structure of the sepiolite, as evidenced by X-ray diffraction patterns reported in Fig.3. 6. The diffractogram of the untreated sepiolite (SO) shows typical reflections of the mineral, corresponding to 20 values of 7.3° [(110) reflection], 20.6° [(131) reflection], 28° [(331) reflection] and 34.9° [(191) reflection]. The more intense diffraction signal corresponds to 2θ=7.3° (Table 3.2) 13. Thermal treatment of sepiolite at 550°C (S5) reduces the intensity of the line at 2θ=7.3° and two new diffraction signals appear at 2θ=11° [(120) reflection] and 2θ=18.8° [(110) reflection] (Table 3.2), which have been ascribed to the removal of crystallization water in sepiolite. The heat treatment at 1000°C (S10) changes the X-ray diffractogram and new lines appear (Table 3.2) which correspond to the formation of smectite (magnesium silicate), a silicate with a different structure from that of sepiolite. Thus, the thermal treatment modifies the surface chemistry and the crystalline structure of the sepiolite [5].

Table 3.2. Experimental data obtained from X-ray diffractograms of untreated (SO) and thermal treated (S5 and S10) sepiolites [5].

Sepiolite	**2θ**	**Intensity**
S0	7.3	380.6
	20.6	66.1
	28	56.1
	34.9	80.7
S5	7.5	48.3
	8.8	57.2
	11	38.1
S10	28.2	53.2
	31.1	79.0
	35.8	30.5

3.5. Characterization and experimental results

Plenty of articles have shown the advantage of reducing the metal oxide grain size down to nanometer scale in order to improve the sensing properties (mainly sensitivity and selectivity), as well as stability over time of the oxide layer [11, 12]. Indeed, such nanostructured semiconductor oxides offer some advantages: a large surface-to-volume ratio, the realization of single crystalline structures (with expected high stability) and a grain size (few nanometers) which is comparable to the depth of the space-charge layer that surrounds the nanograin [13].

Zinc oxide, a n-type semiconductor, has been intensely studied for its versatile physical properties and characterized in literature as gas sensing material showing good stability and gas sensing properties to a wide range of chemical compounds. Recently, substantial efforts have been devoted to realize ZnO-nanostructured materials in order to improve the performances of ZnO based sensor devices [13, 14, 15].

In the present work, we have studied the possibility to synthesize ZnO into the sepiolite structure by means of different acid treatments in order to check the sensitivity of the resulting material towards humidity and NO_2.

Commercial sepiolite powder (Pangel S9, Tolsa, Spain) was first dispersed into distilled water at 10 wt% concentration. Then, the suspension was progressively acidified with HCl to reach a final pH = 0 for 1, 2, 6 and 24 hours at room temperature (24°C ± 1°C). From now on, samples are labeled with the symbols S0 for "as received sepiolite" and S1, S2, S6 and S24 for the samples acidified for 1, 2, 6 and 24 hours, respectively.

The obtained dispersion was vacuum filtered by means of a vacuum pump and washed with distilled water (2 - 3 times). The samples were finally mixed with 1.0 L

of aqueous solution of $ZnSO_4.H_2O$. Thereafter, the pH of the dispersion was adjusted with NaOH to stabilize the suspension at pH 9 and to precipitate all the zinc ions species. The suspension was vacuum filtered and washed with distilled water 3 times to remove all the by-products. Finally, the obtained cake was dried overnight at 150°C in an oven. Calcination was performed at 550°C for 1 h under air and the powder was investigated by X-ray diffraction by means of a Philips PW 3830 X-ray generator ($Cu_{K\alpha}$ radiation, $\lambda = 0.154056$ nm).

Particle size distribution was determined after calcinations by means of a laser granulometer (Malvern 3600D, Great Britain) on the powder as such and after planetary milling for 1 hour.

Thermal analysis (Netzsch STA 409, Germany) was also used to evidence the changes on the sepiolite structure after acid leaching on 150 mg of sample. The analysis were done under static air, and with a heating rate of 10°C.min^{-1} in the temperature range 25-550°C; The investigated and the reference samples were placed into alumina crucibles.

The specific Surface Area (SSA) has been determined by means of an ASAP 2010 (micromeritics, USA) under N_2. The BET method is the most widely used procedure for the determination of the surface area of solid materials and involves the use of the BET equation (eq. 1):

$$\frac{1}{\left(v(\frac{P_0}{P}-1)\right)} = \frac{c-1}{v_m c}\left(\frac{P}{P_0}\right) + \frac{1}{v_m c} \quad (eq.\ 1)$$

where P and P_0 are the equilibrium and the saturation pressure of adsorbates at the temperature of adsorption, v is the adsorbed gas quantity (for example, in volume units), and v_m is the monolayer adsorbed gas quantity, c is the BET constant, related to the energy of adsorption in the first adsorbed layer. The BET equation requires a

linear plot of $\frac{1}{\left(v(\frac{P_0}{P}-1)\right)}$ in function of $\frac{P}{P_0}$ which for most solids, using nitrogen as the adsorbate, is restricted to a limited region of the adsorption isotherm, usually in the range of 0.05 to 0.35.

Finally, the prepared material was uniaxially pressed at 370 MPa, prior to screen-printing interdigitated gold electrodes (ESL Europe 8835(520C), USA) by using a rubber squeegee and a 270 mesh steel screen. After drying overnight, the sensors were heated at 520°C for 18 min with a 2°C/min heating ramp, to optimize the electrical conductivity of the electrodes, as recommended by the ink's manufacturer.

3.5.1. Humidity test

The devices were electrically characterized by using a laboratory apparatus, made of a thermostated chamber working at 25°C in which RH could be varied manually from 0% to 96%. In this system, referring to figure 3.7, compressed air was separated into two fluxes: one was dehydrated over a chromatography alumina bed, while the second one was directed through two water bubblers, generating, respectively, a dry and a humid flow [16].

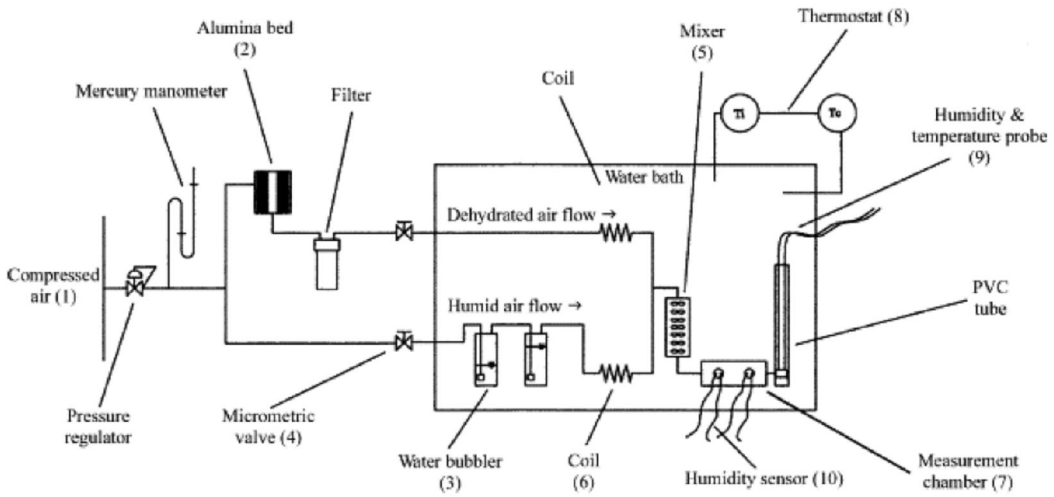

Fig.3.7 Schematic representation of the laboratory apparatus for sensors testing[16]

Two precision microvalves allowed to recombine the two fluxes into one by means of a mixer and to adjust the RH content while keeping constant the testing conditions: a flow rate of 0.05 L/s. The laboratory apparatus for sensors testing was calibrated such that to ensure a constant air flow during electrical measurements and RH was varied by steps, each one of 3 minutes. An external alternating voltage (V = 3.6 V at 1 kHz) was applied on each tested sensor, placed into a PVC tube, acting as a variable resistance of the electrical circuit described above. The sensor resistance was determined by a calibration curve figure 3.8, drawn by substituting the sensors, in the circuit, by known resistances.

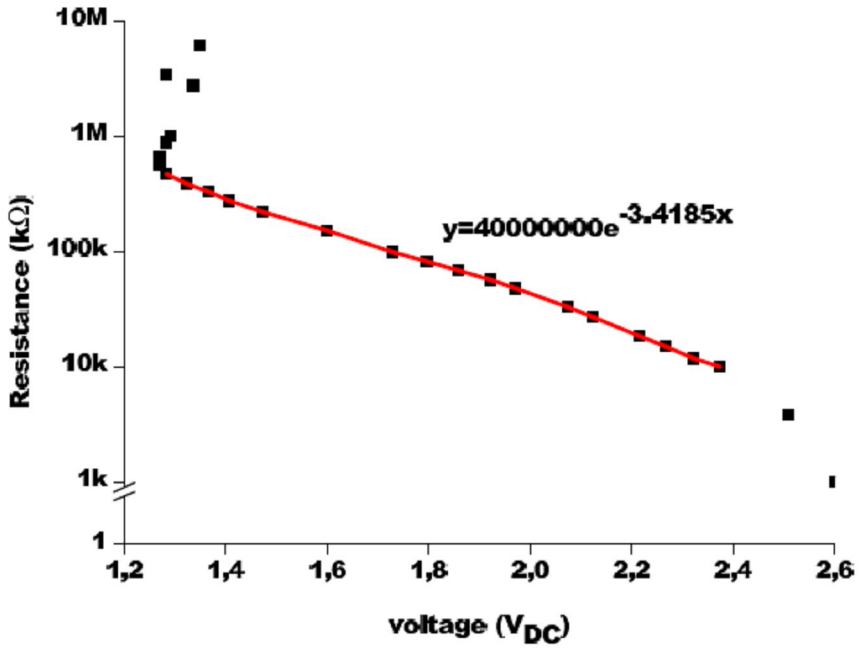

Fig.3.8 Calibration curve for sensors testing: the red fit indicates the range of voltage in which the sensors operated. In the equation, y indicates the resistance, x the voltage.

In particular, the sensors operated from about 1.3 V to 2.4 V, corresponding to about 700 kΩ to 7 kΩ: by increasing the electrical resistance, the continuous voltage measured by the multimeter decreased. In order to obtain the fit of the calibration curve, only the points in which the resistance was linear with respect to the voltage (V_{DC}) were considered, so those from 1.2 to 2.4 V. RH values were measured by means of a commercial humidity and temperature probe (Delta Ohm DO9406, Italy, accuracy: ± 2.5% in the 5-90% RH range).

The sensor response (SR), expressed in %, was defined as the relative variation of the starting resistance, compared with the resistance measured under gas exposure (eq. 2):

$$SR(\%) = 100\frac{|R_0 - Rg|}{R_0} \quad (eq.\ 2)$$

Where R_0 and R_g are the starting (in the absence of the test gas) and the gas exposed measured resistances of the sensors, respectively.

The one hour planetary milling was sufficient to make the dimensions of the obtained powders to be compatible with the openings of the steel screen mesh (45 microns) used for the screen printing process (Fig.3.9).

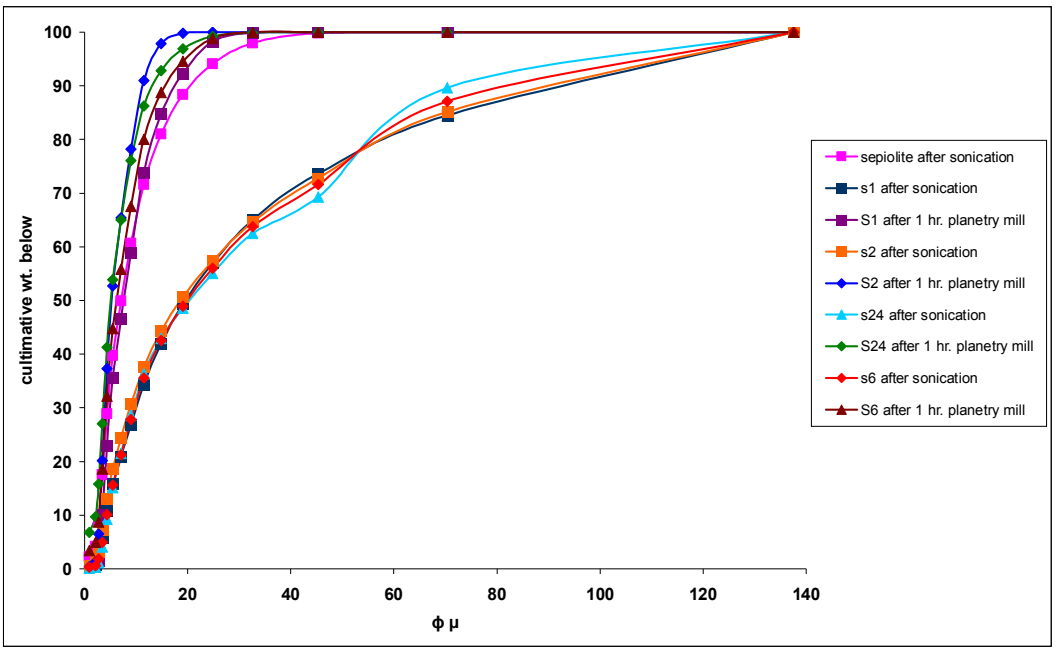

Fig.3. 9: Particle size distribution of the different powders used in this work

Table 3.3. Diameters at 10, 50 and 90 wt% of the cumulative curve for the different powders after sonication and before planetary mill

Cumulative wt%	**Sepiolite (µm)**	**S1 (µm)**	**S2 (µm)**	**S6 (µm)**	**S24 (µm)**
10	3.06	3.95	4.60	4.23	4.67
50	7.06	19.37	18.84	19.53	19.69
90	19.45	74.93	74.31	72.69	70.66

Table 3.4. Diameters at 10, 50 and 90 wt% of the cumulative curve for the different powders after 1 hour planetary mill

Cumulative wt%	**S1 (µm)**	**S2 (µm)**	**S6 (µm)**	**S24 (µm)**
10	3.36	4.10	3.10	2.22
50	7.56	5.22	6.14	5.10
90	18.62	11.42	15.05	14.40

X-Ray diffraction patterns (Fig.3. 10) evidenced that the sepiolite structure seemed to be strongly present in most of the samples but started to be altered after 1 h acid treatment and then turned to a fully amorphous structure in sample S24. ZnO has been detected in all the investigated compositions, from S1 to S24.

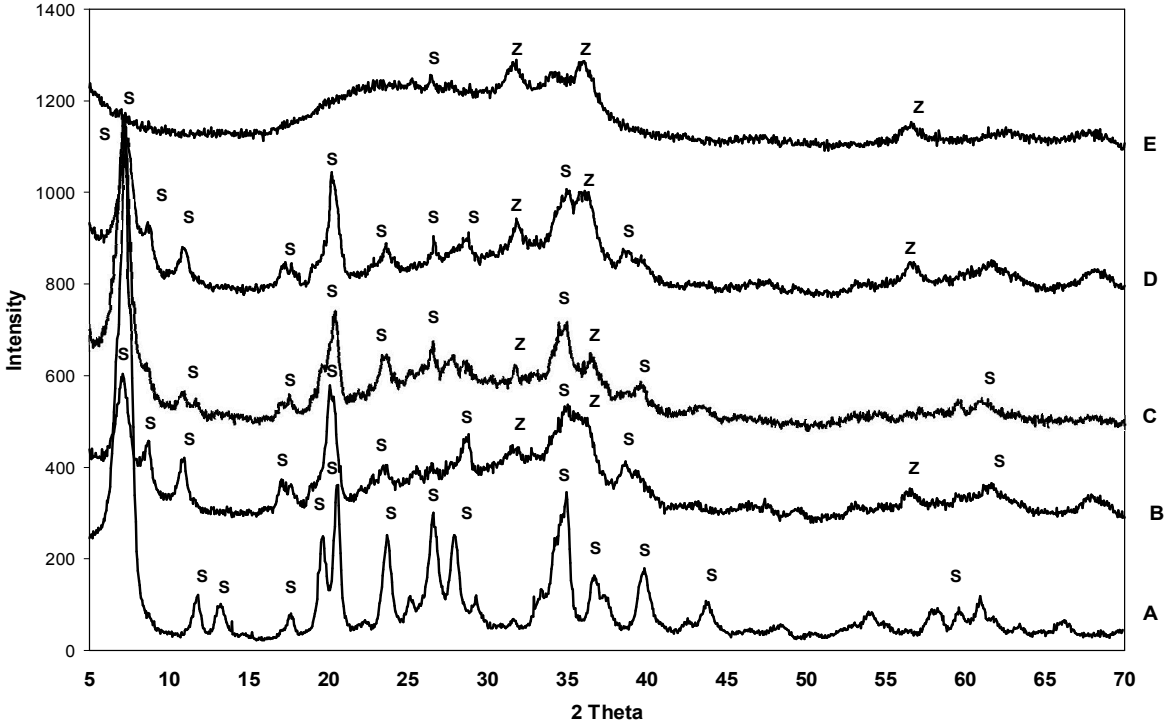

Fig.3.10 XRD patterns of: As received Sepiolite (A) and ZnO-sepiolite treated at pH 0 for 1 h (B), 2 h (C), 6 h (D) and 24 h (E), while (S) refers to Sepiolite peaks and (Z) refers to ZnO phase. JCPDS cards: 36 – 1451 for ZnO and 26 – 1226 for Sepiolite.

Acid treatment of sepiolite removes Mg^{2+} located in its octahedral layer but leaves Si^{4+} coordinated in its tetrahedral layer [17]. The Si-O-Mg-O-Si bond in sepiolite turns into two Si-0-H bonds after acid treatment with H_2SO_4 (Fig.3. 9) [18]. So the internal channels are connected, and the specific surface area becomes larger. When most magnesium is removed, part of micropores and mesopores expand to maxipores. Nonetheless, acid treatment of sepiolite causes the formation of silica [19].

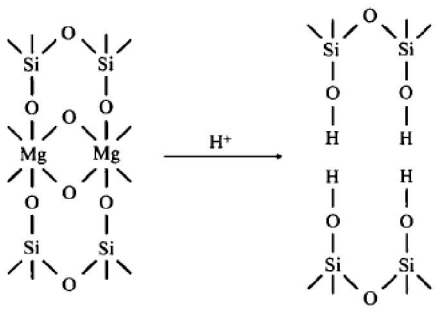

Fig.3.11 Sketch map of ion exchange in sepiolite acid treatment

When sepiolite is acid pre-treated and enough silica is formed, all the ribbons that conform the structure are not interconnected, because some of them have lost their octahedral sheet forming a layer structure [19]. So, a channel structure coming from the sepiolite crystal and a sheet structure corresponding to silica coexist in a singular fiber. Thus, only ribbons present on the channel structure have a tendency to fold, whereas unconnected neighboring silica does not participate in this process. Hence, the torque necessary to fold the structure is not applied, and therefore the crystal remains unfolded with the open channels but without the water of coordination (this fact stabilizes the structure of the original sepiolite) [19]. According to these experimental results, Valentín et al. concluded that an anhydrous sepiolite structure with nanosize channels was formed, in which, the coexistence of both sepiolite and silica in the same fiber was responsible for the thermal stabilization of the structure [19]. This novel structure of the sepiolite is of particular interest, since it can permit the insertion of other molecules into the channels; in our case, ZnO.

The formation of the anhydride sepiolite structure is clearly evidenced when comparing both X-ray diffraction patterns of sepiolite, before and after the thermal treatment [19]. That is, several reflections, such as the reflection of the main peak of the pristine sepiolite that occur at 1.200 nm (110) or reflections at 0.757 nm (130), 0.662 nm (040) and 1.970 nm (060) disappeared, whereas two new reflection peaks at 0.999 nm (110) and 0.795 nm (120) corresponding to the folded monoclinic structure appear [19]. In this case, the reflection of the main peak occurs at 0.439 nm (121). The presence of both folded and unfolded sepiolite has been confirmed by XRD patterns reported on figure 3. 10.

It is known in the literature that hydrochloric-, sulfuric-, or nitric-acid treatment at or below 80°C not only leaches Mg^{2+} from sepiolite, but also forms micro-pores, thereby increasing the specific surface area of sepiolite. The leached amount increases with the soaking time, temperature, and concentration of the acid, and the sepiolite phase disappears over time [17]. The thermal behavior of sepiolite has been extensively studied in the literature too [5,19-23]: in the first step, water superficially adsorbed and zeolitic water are removed up to 170°C (eq. 3), while, between 300° and 350°C, a half of the coordination water molecules is removed and the structure folds (eq. 4). These weight losses have been evidenced on pure sepiolite during thermal treatment (Fig.3.10). However, when sepiolite will rehydrate its structure will also unfold [5]. When coordinated water is lost, a phase transformation takes place, folding the structure of the sepiolite. Consequently, the surface area of the sepiolite is reduced to half because the channels are collapsed [19]. The second half of the coordination water remains entrapped in the collapsed channels and is removed between 350 and 650°C (eq. 5), leading to the formation of anhydride sepiolite. In this case, the structure folding is irreversible at room temperature, even under 100% RH for three months [23]. Above 750-800°C, when dehydroxylation of Mg-OH occurs, the anhydride sepiolite transforms into enstatite (eq. 6).

$$Mg_8Si_{12}O_{30}(OH)_4.(H_2O)_4.8H_2O \rightarrow Mg_8Si_{12}O_{30}(OH)_4.(H_2O)_4 + 8H_2O \quad \text{(eq. 3)}$$

$$Mg_8Si_{12}O_{30}(OH)_4.(H_2O)_4 \rightarrow Mg_8Si_{12}O_{30}(OH)_4.(H_2O)_2 + 2H_2O \quad \text{(eq. 4)}$$

$$Mg_8Si_{12}O_{30}(OH)_4.(H_2O)_2 \rightarrow Mg_8Si_{12}O_{30}(OH)_4 + 2H_2O \quad \text{(eq. 5)}$$

$$Mg_8Si_{12}O_{30}(OH)_4 \rightarrow 8MgSiO_3 + 4SiO_2 + 2H_2O \quad \text{(eq. 6)}$$

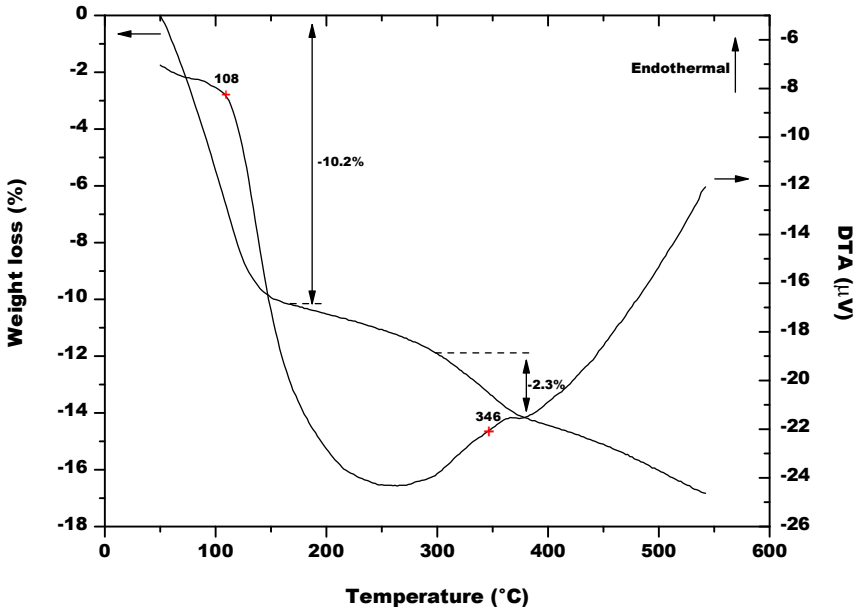

Fig.3.12: TG-DTA of pure sepiolite

The TG-DTA curve of acid-washed sepiolite (Fig.3. 13) is similar to the one of heated pure sepiolite (Fig.3. 12), with a reduced weight loss below 170°C. This indicates that a certain amount of sepiolite channels remain unfolded in the sample after thermal treatment. The two weight loss steps observed in the sepiolite are attributed to superficial adsorbed water and dehydroxilation of Mg–OH groups.

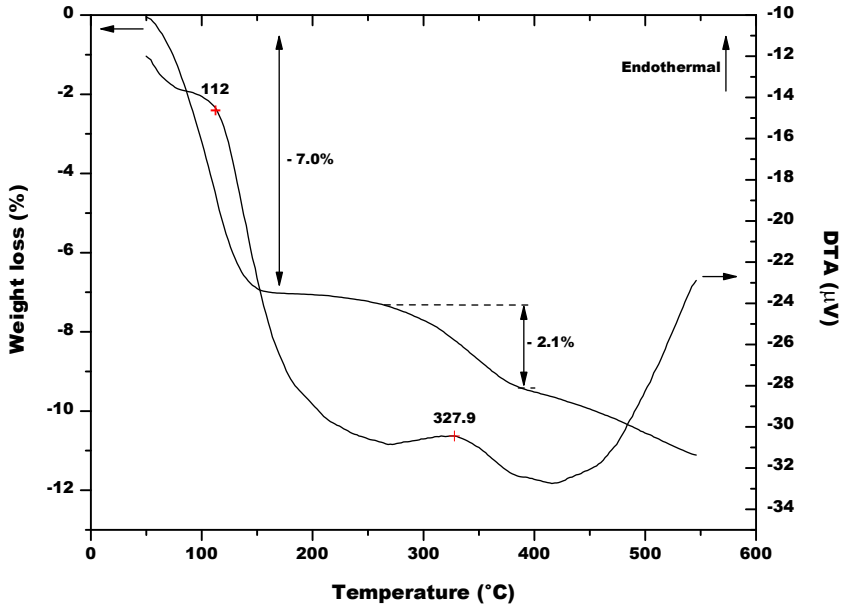

Fig.3.13: TG-DTA of acid-washed sepiolite

No differences have been observed between the TG-DTA curve related to the acid-washed sepiolite (Fig.3. 13) and the sample S2 (Fig.3. 14).

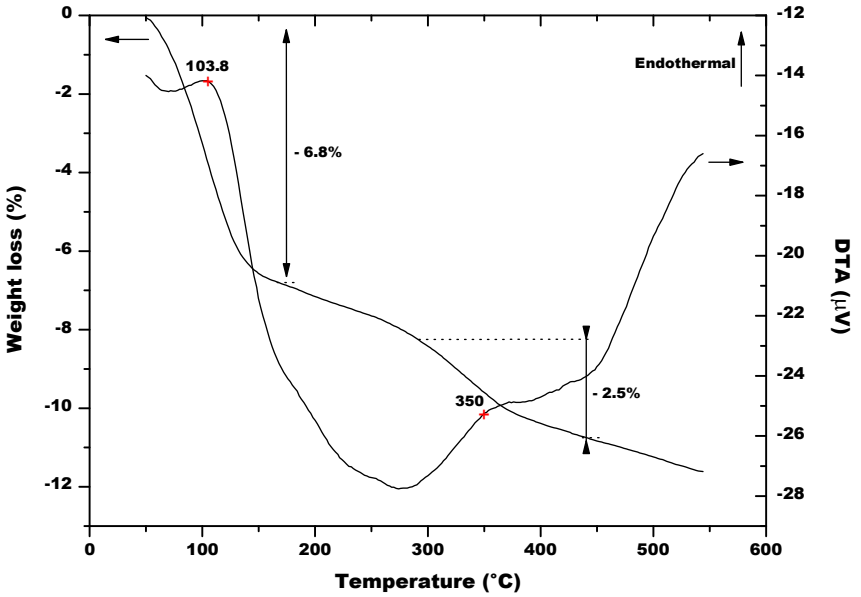

Fig.3.14: TG-DTA of S2 powder

From EDS of S2 (Fig.3.15), we could say that both Mg^{+2} and Zn^{+2} well distributed in all the samples. sepiolite has a rigid ion exchange but Zn^{+2} exist and it could be a result of Mg^{+2} replacements or because of adsorption.

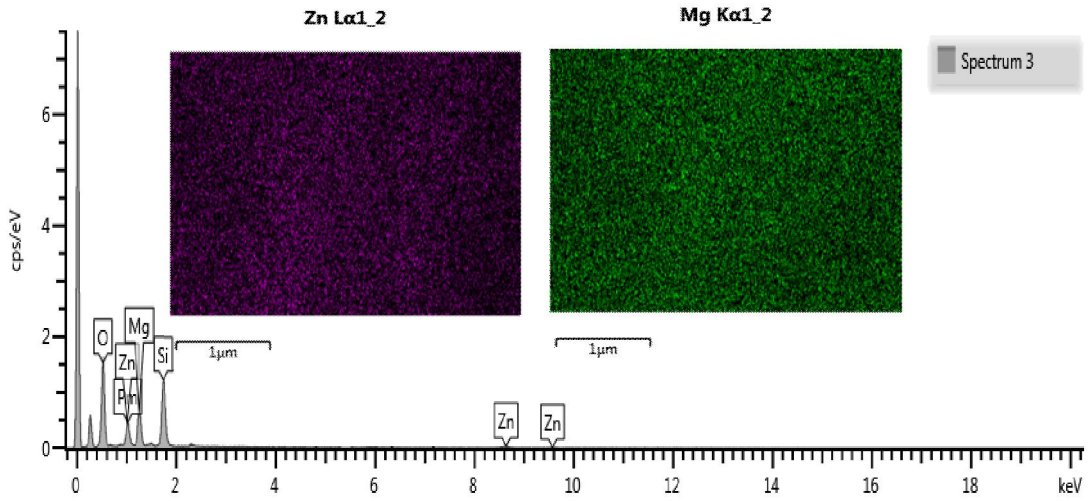

Element	Wt%
O	44.63
Mg	11.41
Si	20.11
Zn	12.18

Fig.3.15: EDS results of S2

FE-SEM observations corresponding to as received and treated sepiolite at pH 0 for 2, 6 and 24 h are shown in Fig.3.16. For times longer than 2 hours, silica fibers breaks steeply till they turned to amorphous silica when increasing the leaching times, because of the progressive sepiolite structure collapsing.

a

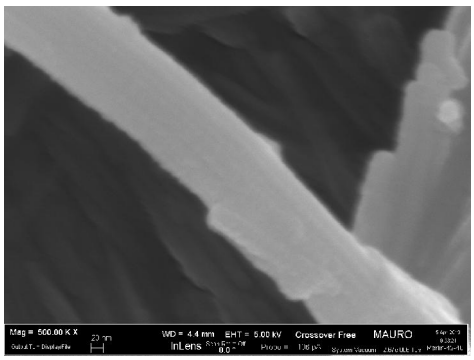

b

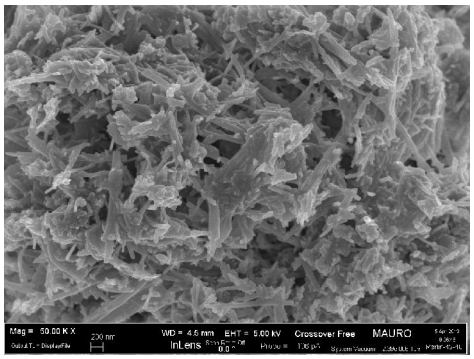

c

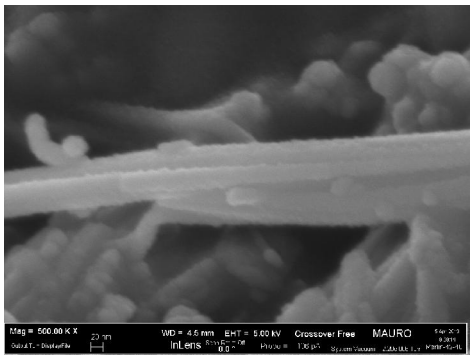

d

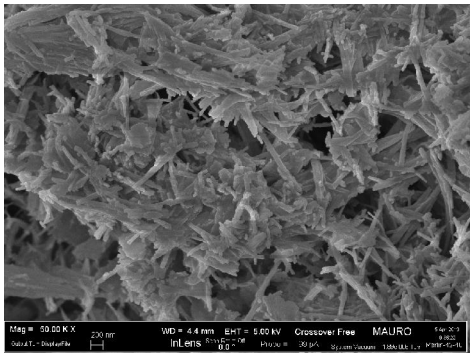

e

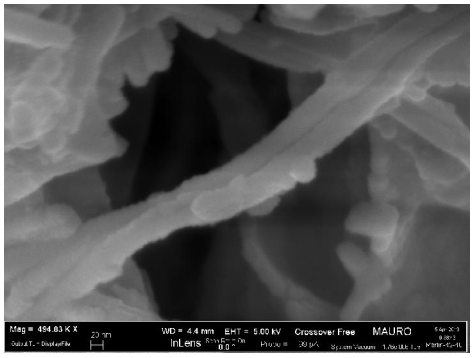

f

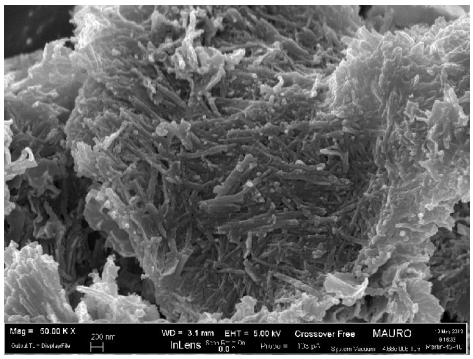

i

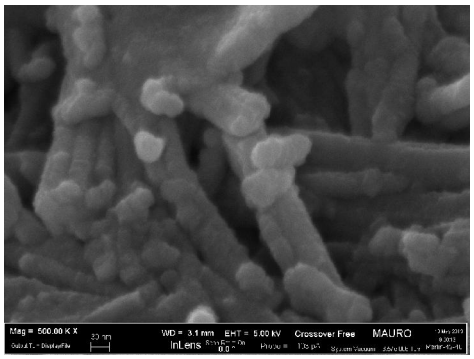

j

Fig.3. 16: FE-SEM observation for: Sepiolite (a, b), ZnO-sepiolite treated at pH 0 for 2 h (c, d), 6 h (e, f) and 24 h (i, j)

SSA decreases with the increasing leaching time (Tab. 5). These results are in contrast with literature [18, 19], but can be explained by the possible precipitation of zinc hydroxide particles into the sepiolite channels.

Table 3.5. Specific Surface Area of S0, S2, S6 and S24 samples measured using N_2 – BET.

Sample	**S0**	**S2**	**S6**	**S24**
SSA (m^2/g)	285.8	125.8	75.7	65.5

It was observed that the electrical resistance of samples S2 and S1 were higher than the others in sequence. Sample S2 starts to detect RH values higher than 28% and S1, 45%, while the other compositions were sensitive to RH values higher than 75%, as the untreated received sepiolite.

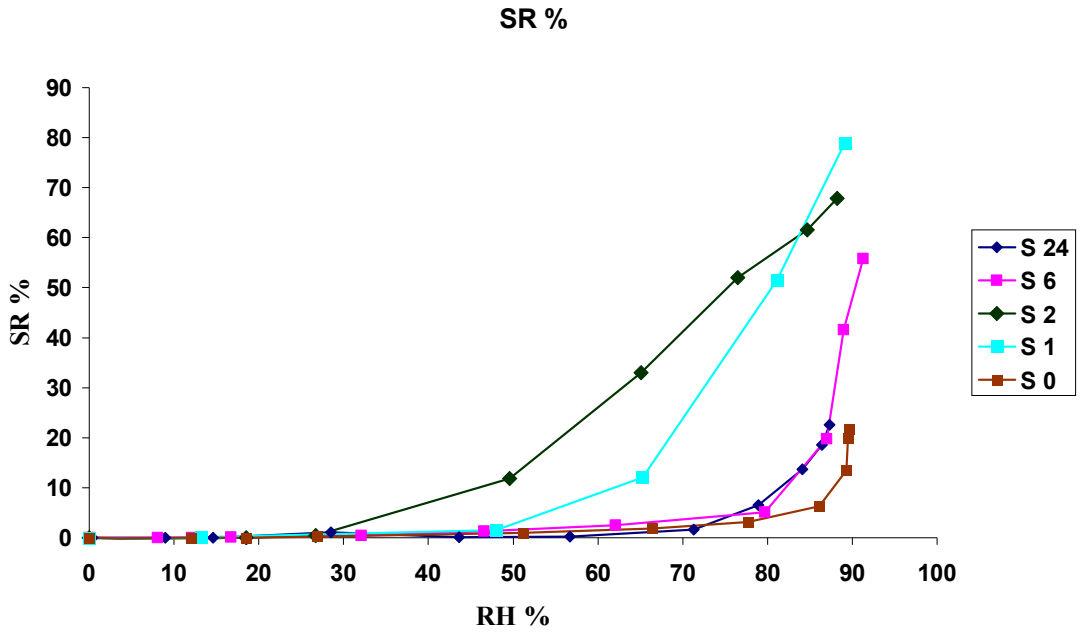

Fig.3.17: Sensors response in function of relative humidity.

The hydration process of clays has been studied in details too, and the mechanism of water retention is based on the following steps: water first adsorbs on hydrophilic sites of the material (the four water molecules coordinated to magnesium in unheated samples [24], at low relative pressures, then, there is a multilayer adsorption on the free "surfaces" inside or outside the pores, in a wide range of relative pressures (0.2 – 0.95) and finally, capillary condensation occurs at high relative pressures in pores [24].

It is well known in the literature that water molecules chemisorb on the available sites of the oxide surface by a dissociative mechanism to form two hydroxyl ions for each water molecule [25, 26]. These hydroxyl groups adsorb on the metal cations and the

protons react with an adjacent surface O^{2-} group to form a second OH^- group. Once formed, this chemisorbed layer is no more affected by surrounding humidity. From spectroscopic experiments on defective single crystals surfaces [27], it is known that chemisorption in perovskites is likely to be completed at a water pressure of the order of 0.1 Pa. At temperatures lower than 100°C, subsequent layers of water molecules are physically adsorbed on the first hydroxyl layer when relative humidity increases. Water molecules in the succeeding physisorbed layers are singly bonded, dissociate to H_3O^+ and form a liquid-like network. The conduction mechanism depends on the surface coverage of adsorbed water. When only hydroxyl ions are present on the oxide surface, the charge carriers are protons, from hydroxyl dissociation, which hop between adjacent hydroxyl groups. When water is present, but surface coverage is incomplete, H_3O^+ diffusion on hydroxyl groups dominates, but proton transfer between adjacent water molecules in clusters also takes place. When the first physisorbed water layer is continuous, charge transport is governed by proton hopping between neighboring water molecules in the continuous film (Grotthus chain reaction). This mechanism means that higher resistivity of the oxides is observed at low RH values [25, 26].

When the pores are cylindrical with one end closed, condensation occurs in all pores with radii up to the Kelvin radius given by the Kelvin equation (7), at given temperatures and water vapor pressures:

$$r_K = \frac{2\gamma M}{\rho RT \ln(P_s/P)} \quad \text{(eq. 7)}$$

where rK stands for the Kelvin radius, γ, ρ, and M for the surface tension, density and molecular weight of water respectively, and P and Ps for water vapor pressures in the surrounding environment and at saturation, respectively [28]. Pores of minor

dimensions are then first filled with condensed water respect to pores having more important radii: water vapor starts to condense at room temperature in mesopores of size 2 nm around 15% RH and continues to around 100 nm under saturated atmosphere. At this time, the electrical conduction is likely to occur through the continuous water layers within the porous sample [29].

Moreover, at 20°C and under atmospheric pressure, the mean free path of water vapor molecules decreases from 84.82 to 85.44 nm in dry air containing humidity traces and up to the water vapor saturation. The molecular entry into the pore is possible if the free path of the incident vapor molecule is less than the pore size [30]. The desired pore size should be one that is comparable to the molecular free path of vapor at all humidity conditions, so that the molecules can impinge and adsorb on the pore wall [29]. Finally, in addition to the protonic conduction in the adsorbed layers, electrolytic conduction occurs in the liquid layer of water condensed within capillary pores, thereby resulting in an enhancement of conductivity. These mechanisms explain why SR, defined in equation (1), tends to decrease with increasing RH, for all the prepared sensors (Fig.3.17).

Conclusions:

- The possibility to synthesize nanoparticles of metal oxide monodispersed and fully protected into the structural channels of an inert matrix (sepiolite) avoiding the inherent and manipulation problems of the small nanoparticle size materials.
- The ability to detect quite low RH values by benefiting of the two advantages: the high SSA of sepiolite and the growth of the second phase ZnO within the sepiolite sheets by low cost procedure.

3.5.2. Measurements under NO_X and H_2

On the other hand, As received and treated sepiolite samples have been tested with DC resistance measurements with gas mixing system under oxidizing NO_2 and reducing gas H_2 at Universität Tübingen, Institut für Physikalische und Theoretische Chemie, Tubingen, Baden-Wurttemberg, Germany

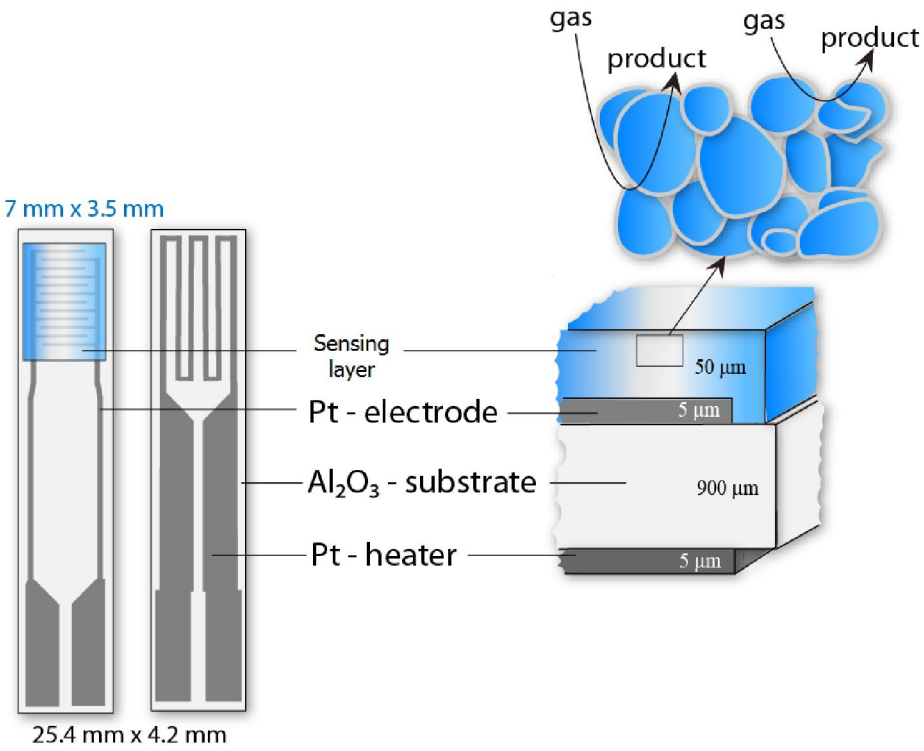

Fig.3.16: Substrate with the pt. electrodes and the pt. heater with the screen-printed sensing layer

The samples S2, S6 and S24 have been prepared as mentioned above (section 1) then the ink was prepared by adding 2- propandiol and mixed in a mortar till getting an acceptable viscous paste. The ink has been printed over an alumina substrate onto Pt electrodes (Fig.3.16).

The prepared samples fired at 550 for 1 h were then tested by DC resistance measurements with gas mixing system under a different concentration of an oxidizing

NO_2 1, 2.5, 5 ppm and reducing gas H_2 20, 50, 100 ppm in a dry and humid air (50%) for 24 hours at different temperatures. The detailed pulse program is shown in table 6.

NO_2 Concentration (ppb)	**H_2 concentration (ppm)**	**Humidity**	**Flux**	**Time (min.)**
0	0	0	200	600
1000	0	0	200	10
0	0	0	200	30
2500	0	0	200	10
0	0	0	200	30
5000	0	0	200	10
0	0	0	200	60
0	20	0	200	10
0	0	0	200	30
0	50	0	200	10
0	0	0	200	30
0	100	0	200	10
0	0	0	200	30
0	0	50	200	240
1000	0	50	200	10
0	0	50	200	30
2500	0	50	200	10
0	0	50	200	30
5000	0	50	200	10
0	0	50	200	60
0	20	50	200	10
0	0	50	200	30
0	50	50	200	10
0	0	50	200	30
0	100	50	200	10
0	0	50	200	30

Tab. 6: pulse program used for the examined samples in DC resistance gas mixing system.

As received sepiolite gave no response neither NO_2 nor H_2, as well as samples S6 and S24 gave poor signals towards both gases at 300^{o}C (Fig.3. 17).

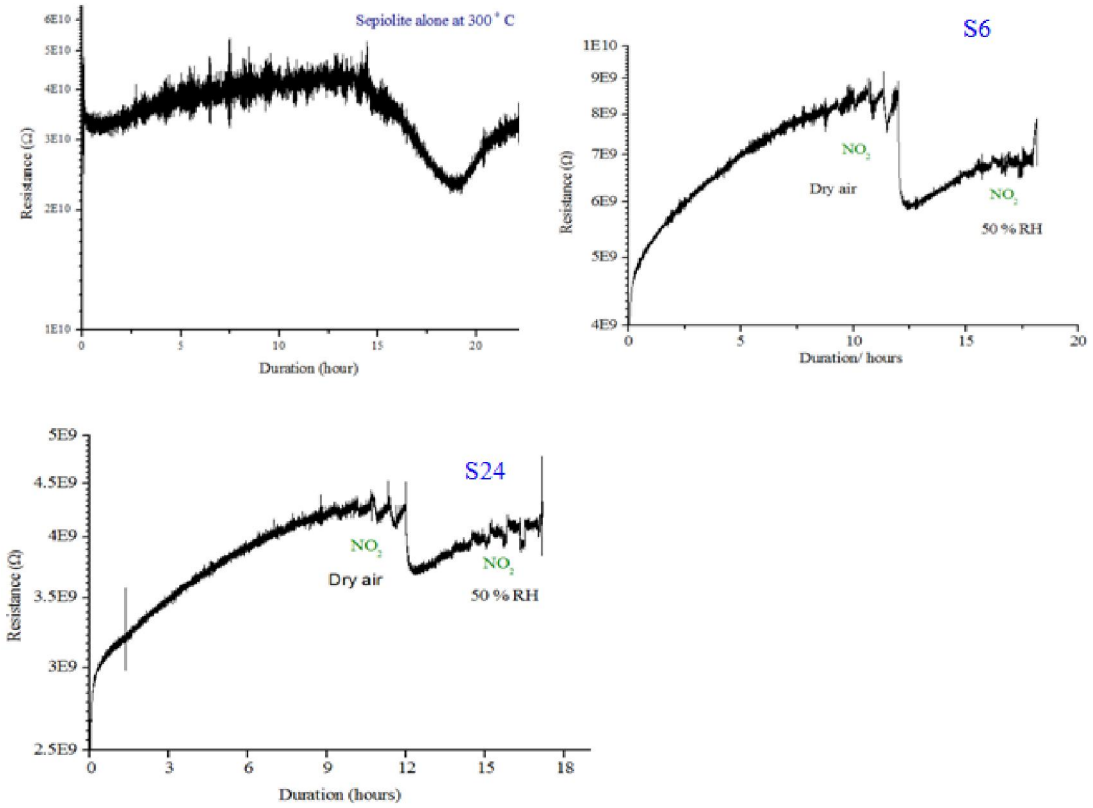

Fig.3. 17: Response curves of as received sepiolite, S6 and S24 samples at 300°C under NO_2 (0.3, 0.5,1,2,3 and 5 ppm) in dry air and 50% RH

While S2 gave a good response to both gases under dry and humid air 50% (Fig.3.18)

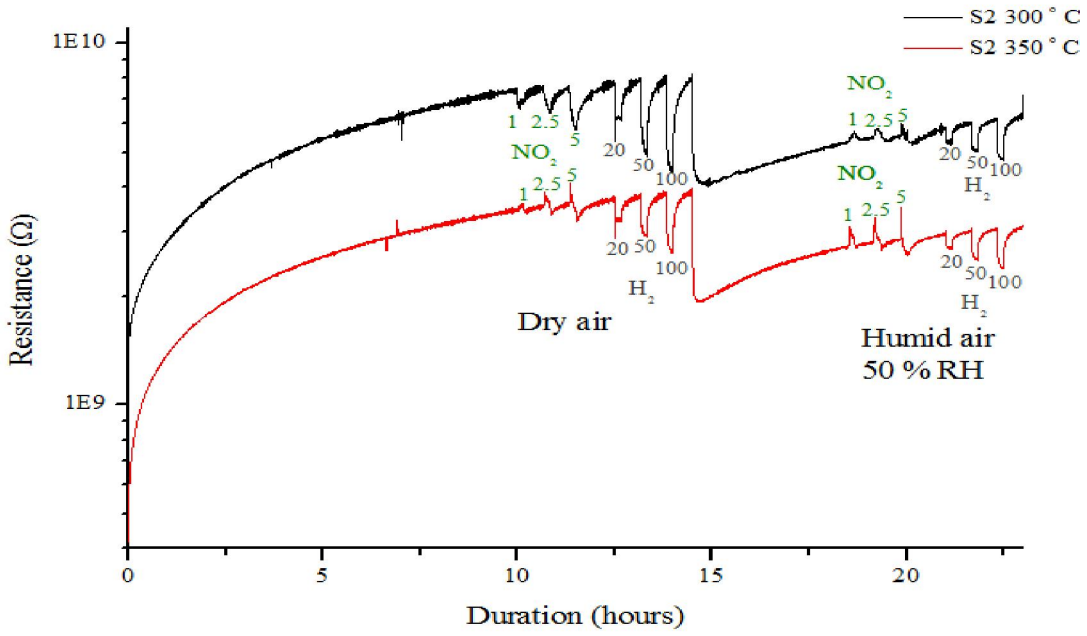

Fig.3.18: Response curves of S2 sample at 300 and 350°C under NO_2 and H_2 in dry air and 50% RH

Zinc oxide (ZnO) is well known as an intrinsic n-type direct wide band gap (3.37 eV) semiconductor with high electron mobility and large exciton binding energy at room temperature. With these properties ZnO is used in optoelectronics, transparent electronics, spintronic devices, and sensor applications [31].

The sensor response is determined mainly by the quantity of active sites on the surface of gas sensors. When an n-type material exposed to the atmosphere of NO_2 which is an oxidizing gas, NO_2 can not only capture the electronics of the semiconductor due to its higher electrophilic property, but also react with the adsorbed oxygen ion leading to the formation of adsorbed NO_2^-, the process of the reaction can be described as follows:

$NO_2(g) + e^- \rightarrow NO_2^-(ads)$ (eq. 8)

$NO_2(g) + O_2^-(ads) + 2e^- \rightarrow 2NO_2^-(ads) + 2O^-(ads)$ (eq. 9)

The above reactions were all decreased the concentration of electron on the surface of the material, thus results in an increase of the material resistance. In addition, the reaction is happened between NO_2^-(ads) and O_2^-(ads):

$NO_2^-(ads) + O_2^-(ads) \rightarrow 2O_2^-(ads) + NO_2$ (eq. 10)

Thus the cycling reaction continued:

$NO_2(g) + e^- \rightarrow NO_2^-(ads)$ (eq. 11)

These series of reactions resulted in the concentration of conduction electrons on the surface of the material further decreased, which led to the conductivity decrease of the material (increase of the resistance), and then the detection of NO_2 is achieved.

As we can see in figure 3.18, the resistance increased upon exposure to NO_2, suggesting that the detection mechanism can be associated with the previous reactions which reported in the literatures [32].

When the metal oxide surface is exposed to reducing gas, the gas reacts with the chemisorbed oxygen thereby releasing electrons back to the conduction band. The overall reducing reactions between H_2 gas and the chemisorbed oxygen species (O^- and O_2^-) are given by:

$H_2 + O^-(ads) \rightarrow H_2O + e^-$ (eq. 12)

$H_2 + O_2^-(ads) \rightarrow H_2O + 2e^-$ (eq. 13)

As a result, the concentration of electrons on the surface of metal oxide increases and the resistance of n-type metal oxide layer decreases and it's also associated with our experimental data, see figure 3.18 [33].

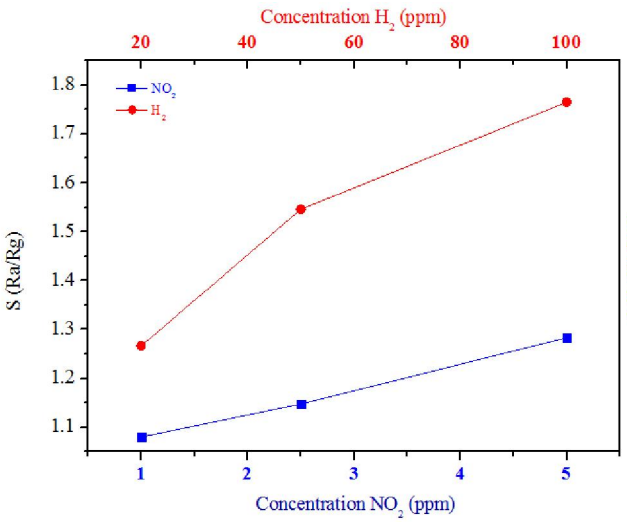

Fig.3.19: Sensor responses of S2 300°C in dry air

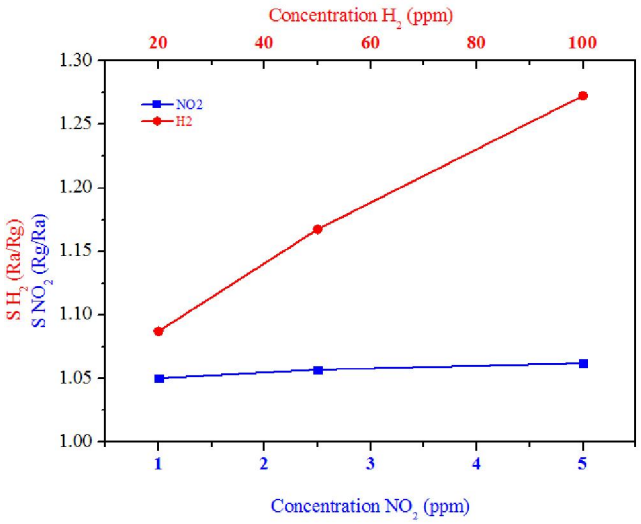

Fig.3.20: Sensor responses of S2 300°C in 50% RH

Conclusions:

Sepiolite leached for 2 h (S2) seems to be capable of detecting NO_2 and H_2 in an optimal working temperature 300°C.

References

1- R. E. Grim, H. Kodama, www.britannica.com, 18/10/2013.

2- F. A. Mumpton and R. Roy, new data on sepiolite and attapulgite, clays and Clay Minerals 5 (1956) 136-143.

3- S. A. McLean, B.L. Allen, and J.R. Craig, the occurrence of sepiolite and attapulgite on the southern High Plains, Clays and Clay Minerals 20 (1972) 143-149.

4- J. Ralph, www.mindat.org, 18/10/2013.

5- A. Torro-Palau and J. C. Fernandez-Garcia, A. C. Orgiles-Barcelo, M. M. Pastor-Bias and J. M. Martin-Martinez, Structural modification of sepiolite (natural magnesium silicate) by thermal treatment: effect on the properties of polyurethane adhesives, Int. J. Adhesion and Adhesives 17 (1997) 111-119.

6- H. Kodama, www.britannica.com, 18/10/2013.

7- R. E. Grim, H. Kodama, www.rsminerals.co.uk, 18/10/2013.

8- M. A. Jr., R. C. Chianelli, and R. M. Arrowood, Computational Study of the Structure of a Sepiolite / Thioindigo Mayan Pigment, Bioinorganic Chemistry and Applications (2012) 1-6.

9- C. Beaugera, G. Lainéa, A. Burrb, A. Taguetc, B. Otazaghinec, A. Rigaccia, Nafion–sepiolite composite membranes for improved proton exchange membrane fuel cell performance, Journal of Membrane Science 430 (2013) 167–179.

10- M. Alkan, G. Tekin and H. Namli, FTIR and zeta potential measurements of sepiolite treated with some organosilanes, Microporous and Mesoporous Materials 84 (2005) 75–83.

11- C. Xu, J. Tamaki, N. Miura and N. Yamazoe, Sens. Actuators B 3 (1991) 147-14 9.

12- N. Yamazoe, New approach for improving semiconducting gas sensors, Sens.Actuators B 5 (1991) 7–19.

13- A. Forleo, L. Francioso, S. Capone, P. Siciliano, P. Lommens and Z. Hens, Synthesis and gas sensing properties of ZnO quantum dots, Sensors and Actuators B, 146 (2010) 111–115.

14- H. Gong, H. J.Q., J. H. Wang, C.H. Ong and F. R. Zhu, Nano-crystalline Cu-doped ZnO thin film gas sensor for CO, Sens. Actuators B 115 (2006) 247–251.

15- L. F. Dong, Z. L. Cui and Z. K. Zhang, Gas sensing properties of nano-ZnO prepared by arc plasma method, Nanostruct. Mater. 8 (7) (1997) 815–823.

16- J. M. Tulliani and P. Bonville, Influence of the dopants on the electrical resistance of hematite-based humidity sensors. Ceram. Int. 31 (2004) 507–514.

17- A. Miuraa, K. Nakazawaa, T. Takeia, N. Kumadaa, N .Kinomuraa, R. Ohkib and H. Koshiyamab, Acid-, base-, and heat-induced degradation behavior of Chinese sepiolite, Ceramics International, 38 (2012) 4677–4684.

18- W. Fei, L. Jin-sheng, T. Qing-Guo, M. Jun-Ping, W. Zi-Zhao, L. Guo-Sheng, Microstructure of sepiolite and its adsorbing properties to dodecanol, Trans. Nonferrous Met, SOC. China 16 (2006) 406 - 410.

19- J.L. Valentín , M.A. López-Manchado, A. Rodríguez, P. Posadas, L. Ibarra, Novel anhydrous unfolded structure by heating of acid pre-treated sepiolite, Applied Clay Science 36 (2007) 245–255.

20- H. Nagata, S. Shimoda, T. Sudo, On dehydration of bound water in sepiolite, Clays and Clay Minerals, 22 (1974) 285 - 293

21- C. Serna, J. L. Ahrlichs and J. M. Serratosa, Folding in sepiolite crystals, Clays and Clay Minerals, 23 (1975) 452 -457.

22- M. Molina-Sabio, F. Caturla, F. Rodríguez-Reinoso and G. V. Kharitonova, Porous structure of a sepiolite as deduced from the adsorption of N_2, CO_2, NH_3 and H_2O, Microporous and Mesoporous Materials, 47 (2001) 389-396.

23- M. V. Kok, Thermal Characterization of Sepiolite Samples, Energy Sources, Part A, 35 (2013) 173–183.

24- T. Seiyama, N. Yamazoe and H. Arai, Ceramic humidity sensors, Sensors and Actuators, 4(1) (1983) 85-96.

25- E. Traversa; Ceramic sensors for humidity detection: the state-of-the-art and future developments, Sensors and Actuators B, B23 (2-3) (1995), 135-156.

26- E. McCofferty and A.C. Zettlemoyer, Adsorption of water vapour on α-Fe_2O_3, discussion of Faraday Society, 52 (1971) 239-254.

27- V. E. Henrich, Electron spectroscopic determination of the electronic, geometric and chemisorption properties of oxide surfaces. In: L.C. Dufour, C. Monty and G. Petot-Ervas (Eds), Surfaces and Interfaces of Ceramic Materials, Kluwer Academic Publishers, Dordrecht (1989) 1-28.

28- N. Yamazoe, Y. Shimizu, Humidity sensors: principles and applications, Sensors and Actuators, 10 (1986) 379-398.

29- K.S. Chou, T. K. Lee and F.J. Liu, Sensing mechanism of a porous ceramic as humidity sensor, Sensors and Actuators B: Chemical, 56 (1–2) (1999) 106-111.

30- G. Banerjee and K. Sengupta, Pore size optimization of humidity sensor – a probabilistic approach, Sensors and Actuators B, 36 (2002) 34-41.

31- S. Öztürk , N. Kılınç , N. Taşaltin , Z. Z. Öztürk, A comparative study on the NO_2 gas sensing properties of ZnO thin films, nanowires and nanorods, Thin Solid Films, 520 (2011) 932–938.

32- B. Shoulia, C. Liangyuanb, L. Dianqinga, Y. Wenshenga, Y. Pengchenga, L. Zhiyonga, C. Aifana and C. C. Liub, Different morphologies of ZnO nanorods and their sensing property, Sensors and Actuators B, 146 (2010) 129–137.

33- K. Wetchakun, T. Samerjai, N. Tamaekong, C. Liewhiran, C. Siriwong, V. Kruefu, A. Wisitsoraat, A. Tuantranont, S. Phanichphant, Semiconducting metal oxides as sensors for environmentally hazardous gases, Sensors and Actuators B 160 (2011) 580– 591.

Chapter 4- Hematite and ferrites materials

4.1. Principal iron oxides

Iron oxide materials are chemical compounds composed of iron and oxygen. Natural iron oxides include a combination of one or more ferrous or ferric oxides, and impurities, such as manganese, clay, or organics.

There are sixteen known iron oxides and oxyhydroxides, reported in Table 4.1. The uses of these various oxides and hydroxides are diverse ranging from pigments in ceramic glaze, to use in thermite [1].

One of the most important iron oxides, hematite (α-Fe_2O_3), a n-type semiconductor, features non-toxicity, low cost, high stability, and environmental compatibility, has been intensively investigated, due to its potential application in gas sensors, rechargeable lithium ion batteries, catalysts, pigments, magnetic devices, photo-anodes for efficient water splitting by sunlight, waste-water treatment, and in other biological and medical fields [2].

Table 4.1. Principal iron oxides [3]

	Name	Formula	Description
Oxides	Iron (II) oxide or wüstite	FeO	black to brown; cubic; periclase group
	Iron(II,III) oxide or magnetite	Fe3O4	greyish black; cubic; spinel group
	Iron(III) oxide - hematite (α phase) - β phase - maghemite - ε phase	α-Fe2O3 β-Fe2O3 γ-Fe2O3 ε-Fe2O3	reddish brown;hexagongal; hematite group / dark brown; cubic; /

Hydroxide	Iron (II) hydroxide	Fe(OH)2	/
	Iron (III) hydroxide	$Fe(OH)_3$	/
Oxide/ hydroxide	Goethite	α-FeOOH	blackish brown; orthorhombic
	Akaganeite	β-FeOOH	yellowish brown; monoclinic
	Lepidocrocite	γ-FeOOH	ruby-red to reddish brown; orthorhombic
	feroxyhyte	δ-FeOOH	brown, yellow-brown; hexagonal
	ferrihydrite	5Fe2O3 9H2O	yellow-brown to dark brown; hexagonal
	schwertmannite	$Fe_{16}O_{16}(OH)_{12}(SO_4)_2$	orange-brown; tetragonal
	limonite	$FeO(OH)\cdot nH_2O$	yellow-light brown

In literature only hematite and magnetite have been proposed as sensing materials, magnetite was studied for CO detection [4] and as humidity sensor in magnetite/silicon composite thin films [5, 6]. Hematite will be discussed in detail as a humidity and gas sensor.

Chemical compounds of iron (III) oxide are called ferrites. Many of them are magnetic materials and they are used to make permanent magnets, ferrite cores for transformers, and in various other applications.

A large part of ferrites are spinels with the formula AB_2O_4, where A and B represent various metal cations, usually including iron. Spinel ferrites usually adopt a crystal motif consisting of cubic close-packed (fcc) oxygen anions (O^{2-}) with A cations occupying one eighth of the tetrahedral sites and B cations occupying half of the

octahedral sites. Some ferrites have hexagonal crystal structure, e.g. barium hexa-ferrite $BaO_6Fe_2O_3$ or $BaFe_{12}O_{19}$ [7].

4.2. Hematite properties

4.2.1. Principal properties of hematite

The name hematite is derived from the Greek word for blood αίμα because hematite can be red, as in rouge, a powdered form of hematite. The color of hematite lends it well in use as a pigment. The name was derived from Ancient Greek: αἱματίτης λίθος (haimatitēs lithos, "blood-red stone"), which was imported from latin in lapis hæmatite, from French in hematite pierre and finally from English in hematite.

Hematite is the mineral form of iron (III) oxide (Fe_2O_3), coloured black to steel or silver- gray, brown to reddish brown, or red. Varieties include kidney ore, martite (pseudomorphs after magnetite), iron rose and specularite (specular hematite). While the forms of hematite vary, they all have a rust-red streak. Hematite is harder than pure iron, but much more brittle. Maghemite is a hematite- and magnetite-related oxide mineral.

Huge deposits of hematite are found in banded iron formations. Grey hematite is typically found in places where there has been standing water or mineral hot springs, such as those in Yellowstone National Park in the United States. The mineral can precipitate out of water and collect in layers at the bottom of a lake, spring, or other standing water. Hematite can also occur without water, however, usually as the result of volcanic activity.

Clay-sized hematite crystals can also occur as a secondary mineral formed by weathering processes in soil, and along with other iron oxides or oxyhydroxides such as goethite are responsible for the red color of many tropical, ancient, or otherwise

highly weathered soils. Good specimens of hematite come from England, Mexico, Brazil, Australia, United States and Canada.

Ochre is clay that is colored by varying amounts of hematite, varying between 20% and 70%. Red ochre contains unhydrated hematite, whereas yellow ochre contains hydrated hematite ($Fe_2O_3 \bullet H_2O$). The principal use of ochre is for tinting with a permanent color. The red chalk winning of this mineral was one of the earliest in history of mankind.

The powdery mineral was first used 164,000 years ago by the Pinnacle-Point man obviously for social differentiation. Hematite residues are also found in old graveyards from 80,000 years ago. Near Rydno in Poland and Lovas in Hungary, palaeolitic red chalk mines have been found that are from 5000 BC, belonging to the Linear Pottery culture at the Upper Rhine.

Rich deposits of hematite have been found on the island of Elba that have been mined till the time of the Etruscans.

Hematite can be also part of a complex solid solution oxyhydroxide system having various degrees of water, hydroxyl group, and vacancy substitutions that affect the mineral's magnetic and crystal chemical properties [8].

A cross section of the unit cell in (110) direction is shown in Figure 4.1. All oxygen in the structure is surrounded by four iron atoms. Two different Fe–O bond lengths occur in the crystal: a short bond of 1.944 Å (19,44 nm) and a long bond of 2.113 Å (21.13 nm). In the structure, each oxygen has two long and two short bonds with iron (Figure 4.1) [9].

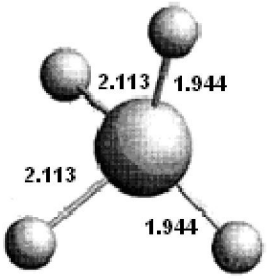

Fig 4.1. The different Fe–O bond lengths in the hematite crystal. The large sphere represents an oxygen while the smaller spheres represent the iron [9]

The dominant crystal face for these crystals is probably the (001) face. At the perfect (001) face, all surface groups are doubly coordinated groups with one long and one short bond. So hematite can be expected to be relatively inert. The (001) face, however, may have imperfections, leading to a different composition in terms of surface sites than a perfect (001) face. For the calculations it is assumed that at several positions underlying Fe atoms are missing. Here two options are possible:

a) A deep lying iron ion is missing in the surface so that three singly coordinated surface groups with a short Fe–O bond arise;

b) A higher lying iron ion is missing in the surface so that three singly coordinated surface groups with a long bond arise.

So at an imperfect (001) face, two types of singly coordinated surface groups and one type of doubly coordinated groups may occur.

Other probable crystal surfaces are the (110) and (120) faces. The surface site composition of these two faces are similar; singly, doubly, and triply coordinated surface groups in a 1:1:1 ratio. All singly coordinated surface groups have a short bond and all triply coordinated surface groups have two long and one short bond.

The doubly coordinated surface groups can be separated in two different types: groups with two short bonds and groups with two long bonds, occurring in a 2:1 ratio. The

above mentioned crystal faces are probable to occur at this crystal, and they will be used for the description of the charging behavior [9].

The principal properties of hematite are resumed in Table 4.2

Table 4.2. Principal properties of hematite [10, 11]

Physical Properties of Hematite			
Formula	α-Fe_2O_3		
System	Trigonal	**Hardness**	5 - 6
Lustre	Metallic, Sub-Metallic, Dull, Earthy		
Geological Setting	Large ore bodies of hematite are usually of sedimentary origin; also found in high-grade ore bodies in metamorphic rocks due to contact metasomatism, and occasionally as a sublimate on igneous extrusive rocks ("lavas") as a result on volcanic activity. It is also found coloring soils red all over the planet.		
Diaphaneity (Transparency)	Opaque		
Color	Steel-grey to black in crystals and massively crystalline ores, dull to bright "rust-red" in earthy, compact, fine-grained material.		
Streak	Reddish brown ("rust-red")		
Hardness (Mohs)	5 - 6 (Pyrite)		

Hardness (Vickers)	VHN_{100}=1000 - 1100 kg/mm^2		
Tenacity	Brittle		
Cleavage	None Observed		
Parting	Partings on {0001} and {1011} due to twinning. Unique cubic parting in masses and grains at Franklin Mine, Franklin, NJ.		
Fracture	Irregular/Uneven, Sub-Conchoidal		
Comment	Elastic in thin lamellae		
Density (measured)	5.27 g/cm^3	**Density (calculated)**	5.255 g/cm^3
Impurities	Ti, Al, Mn, H_2O		

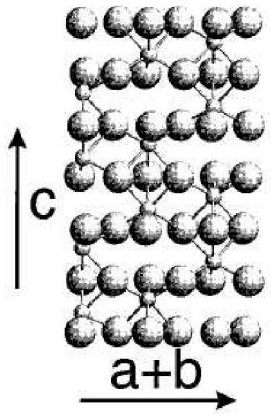

Fig.4.2. the unit cell of hematite, viewed perpendicular to the 110 face. The large spheres represent the oxygen, the smaller spheres the iron. [10]

Table 4.3. Crystallography properties of hematite [10, 11]

Crystallography of Hematite	
Crystal System	Trigonal
Class (H-M)	3*m* (3 2/*m*) - Hexagonal Scalenohedral
Space Group	*R*3*c* {*R*3 2/*c*}
Cell Parameters	a = 50.38(2) nm, c = 137.72(12) Å
Ratio	a:c = 1 : 2.734
Unit Cell Volume	3.02 10^5 nm³ (Calculated from Unit Cell)
Z	6
Morphology	Crystals generally thick to thin tabular {0001}, rarely prismatic [0001] or scalenohedral; also rarely rhombohedral {1011}, producing pseudo-cubic crystals. Often found in sub-parallel growths on {0001} or as rosettes ("iron crosses.") Sometimes in micaceous to platy masses. May be compact columnar or fibrous masses, sometimes radiating, or in reniform masses with a smooth fracture ("kidney ore"), and botryoidal and stalactic. Frequently in earth masses,

	also granular, friable to compact, concretionary and oolitic.
Twinning	Penetration twins on {0001}, or with {1010} as a composition plane. Frequently exhibits a lamellar twinning on {1011} in polished section.

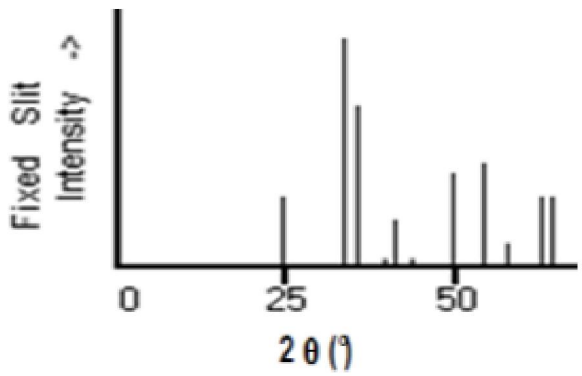

2θ (°)	I/I_0 (%)
24.138	30
33.153	100
35.612	70
39.277	3
40.855	20
43.519	3
49.480	40
54.091	45
56.152	1
57.429	5
57.590	10
62.451	30
63.991	30
66.028	<1
69.601	3

Fig. 4.3. XDR pattern of hematite and related peaks position and intensity, JCPDS 33-0664

4.2.2. Electric properties

α-Fe_2O_3 is an intrinsic semiconductor above 650°C, where it is oxygen pressure independent [12].

The n-type semiconductor behaviour of hematite is clearly reported in the literature [13]. Oxygen vacancies ($V_O^{\bullet\bullet}$) can be produced by heating this material following the disorder equation [14]:

$$O_O^X = \frac{1}{2}O_{2(g)} + V_O^{\bullet\bullet} + 2e' \quad (1)$$

Gardner et al. [15] measured the oxygen deficit resulting from this equilibrium shift. Considering this structural disorder and the independence of the hematite conductivity regarding the oxygen partial pressure, it is possible to conclude that this material is an intrinsic semiconductor [14, 16].

The introduction of defects and impurities by doping can change the electrical behavior respect to the pure hematite [16].

Doping is the process of intentionally introducing impurities into an extremely pure (also referred to as intrinsic) semiconductor to change its electrical properties. The impurities are dependent upon the type of semiconductor. Lightly and moderately doped semiconductors are referred to as extrinsic.

The p-type conductivity of the hematite is mainly due to the presence of cationic impurities whereas a predominant n-type conductivity is observed in the material in which are localized defects associated to donor states [13].

Santilli et al. have studied in details the electrical behavior of hematite with respect to the defects in the material (Figure 4.3).

For T< 750°C an extrinsic behavior is observed. Here again a strong influence of the origin of the precursor and of the sintering time is observed. Fresh (F) ceramics show a σ versus P_{O2} conductivity characteristic of p-type samples, while aged (A) ceramics (holding times > 0 - 25h) are n-type when heated at low P_{O2} where the precursor F = fresh and A = aged.

In the A ceramics sintered for 1 h, the defects are ordered according to a double network which tends to disappear as the heat treatment is prolonged, leading to randomly distributed extended defects. The evolution of defects in F materials is more

complex: many defects are present after 1 h at 1100°C; they tend to order during further heat treatment, leading ultimately to the quasi-ordered network [13].

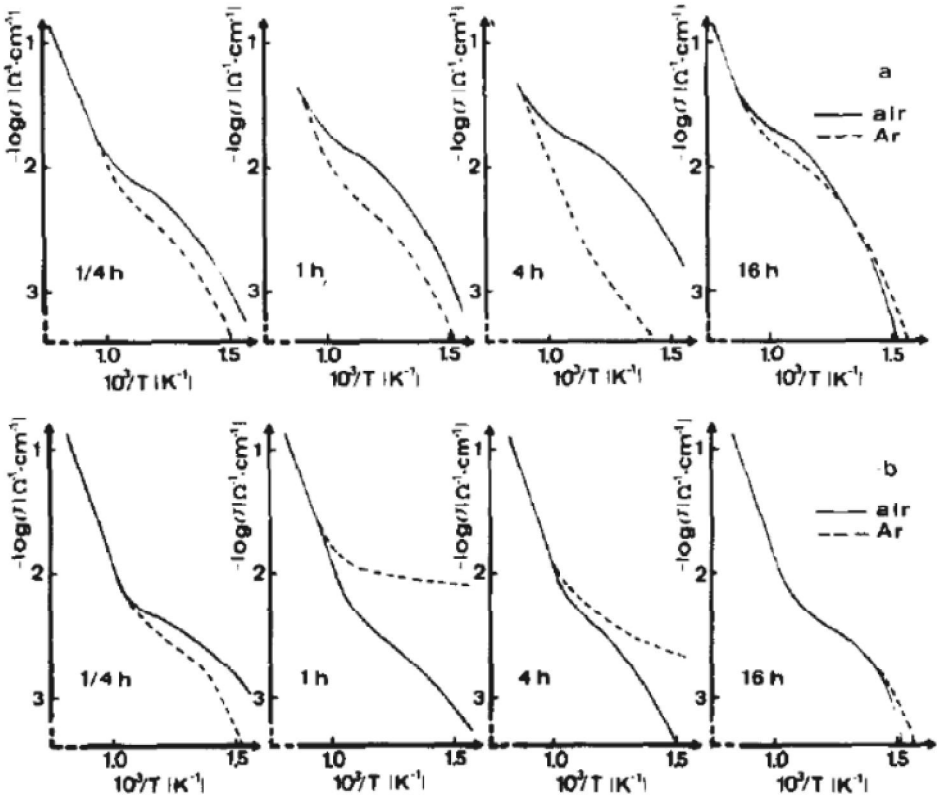

Fig.4.4. Evolution with temperature of electrical conductivity measured in air (P_{O2} = 0.21 atm) and argon (P_{O2} = 7 x 10^{-4} atm): a) F ceramic sintered at 1100°C for various sintering times, b) A ceramic sintered at 1100°C for various sintering times [13]

4.2.3. Hematite compound: ferrites based on alkaline and alkaline earth elements

Ferrites can be produced by heating a mixture of powdered carbonates precursors pressed into a mold. During the heating process, calcination of carbonates occurs:

$$MCO_3 \rightarrow MO + CO_2$$

The resulting mixture of oxides undergoes reaction sintering. [17, 18].

The result of hematite doping with alkaline and alkaline earth elements is the formation of ferrites like $LiFe_5O_8$, $BaFe_{12}O_{19}$, $MgFe_2O_4$, $KFe_{11}O_{17}$, after a first thermal treatment at 900°C for 1 hour [15].

In the last decades many of scientists concerned with doped ferrites in the application of humidity sensors, but very few papers were available concerning gas sensors.

4.2.3.1. Lithium ferrite

There are two types of lithium ferrites, $LiFeO_2$ and $LiFe_5O_8$.

$LiFeO_2$ is obtained above 700°C, it has a cubic structure and the Fe^{3+} and Li^+ ions are placed in the crystallographic sites occupied by Fe^{2+}; the theoretical density is 4.394 g/cm^3.

$LiFe_5O_8$ is obtained by the reaction of hematite and $LiFeO_2$

$$2\ Fe_2O_3 + LiFeO_2 \rightarrow LiFe_5O_8 \quad (2)$$

The structure is cubic spinel like and its density is 4.758 g/cm^3. It is a ferromagnetic material with a Curie point at 620°C and a total magnetic moment of 2.6 μB [16].

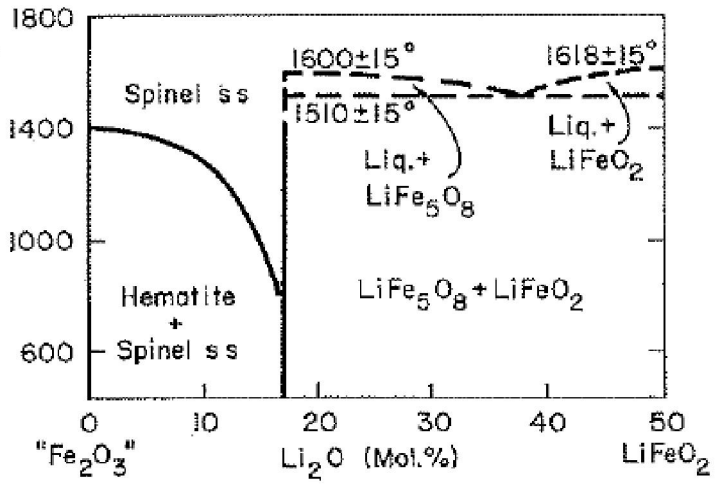

Fig.4.5. System $LiFeO_2$-Fe_2O_3, liquids throughout and solid phases in Fe_2O_3-rich region are ternary and only approximately represented [19]

4.2.4. Ceramic sensors based on hematite

Chemical sensors play a very important role in both environmental protection and human health. The fabrication of metal oxide semiconducting nanomaterials with large surface-to- volume ratios for gas sensor applications is currently a major focus of nanoscience and nanotechnology. As an important n-type semiconductor, hematite, features non-toxicity, low cost, high stability, and environmental compatibility [20].

The properties of α-Fe_2O_3 and of ferrites have been studied in detail especially as humidity sensor.

Pelino et al. studied in details α-Fe_2O_3 properties as a ceramic humidity sensor [21]. The initial Fe_2O_3 powder material has been derived by thermal decomposition of FeOOH. The sintering temperature of the ceramics lies within the interval 850°C-1100°C. The influence of the sintering mode on both the size distribution of the pores and the sensitivity has been studied. Optimum parameters have been obtained at sintering temperatures of 850°C-900°C. Sensor hysteresis is not observed. The response time is from three to five minutes. The dependence of this parameter on the form of the electrode has been studied [21]. The best results have been achieved when the flat walls of the pellets were covered by closely set conducting electrodes. This provided, the resistance is minimal, the response time is the shortest, and the sensitivity is maximum.

In table 4.4 are reported the materials based on hematite used as ceramic humidity sensors.

Table 4.4. Principal ceramic humidity sensors based on hematite

Material	Sintering T (°C)	RH range (%)	Operating T(°C)	References
α-Fe_2O_3, pellet	850-1100	0-95	25	[21]
alkali and alkaline earth doped Fe_2O_3, screen printed films	850-950	40-95 except Ba-doped Fe_2O_3	25	[22]
$MgFe_2O_4$, thick film	750-850	65-85	40	[23]
Cerium oxide add to $MgFe_2O_4$	1000	10-90	25	[24]
$Mg1-xLi_xFe_2O_4$	750	10-80	25	[25]
Li-doped-Fe_2O_3, thin films	80	0-95	25	[26]
Li and Au-doped-Fe_2O_3, thin films	80	0-30	25	[27]
Li, Zn and Au-doped-Fe_2O_3, thin films	80	0-100	/	[28]
silica-coated-Fe_2O_3, pellet	850-1100	0-100	20-70	[29]

α-Fe_2O_3 - doped sepiolite	520 600-1000	5-98	25	[30]

4.2.5. Lithium ferrite as humidity sensors

It can be noted instead the strong enhancement of the sensitivity of Li-doped films, FL025 (iron oxide film doped with 25 wt% of Li), FL10 (iron oxide film doped with 10 wt% of Li) and AFL10 (iron oxide film doped with 5 wt% of gold and 10 wt% of Li). This is due to the high charge/size ratio of Li which provides preferential sites for the water molecules adsorption.

Water is a donor type molecule and giving one electron to the bulk, becomes positively charged and this leads to the formation of a negative space charge region (Fig. 4.6):

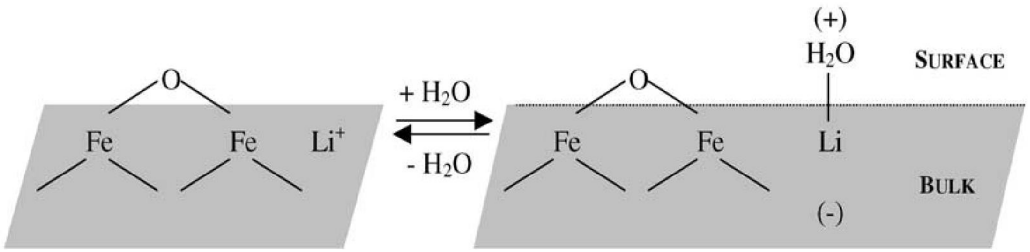

(1)

Fig.4.6. Interaction of lithium ions with water molecules

A major problem associated with the practical use of metal oxide films as humidity sensors is the drift of the baseline resistance with time. Sensors based on iron oxide and Li–iron oxide have shown a large baseline drift with time attributed to a progressive hydroxylation of the sensing surface layer, according to Fig. 4.7:

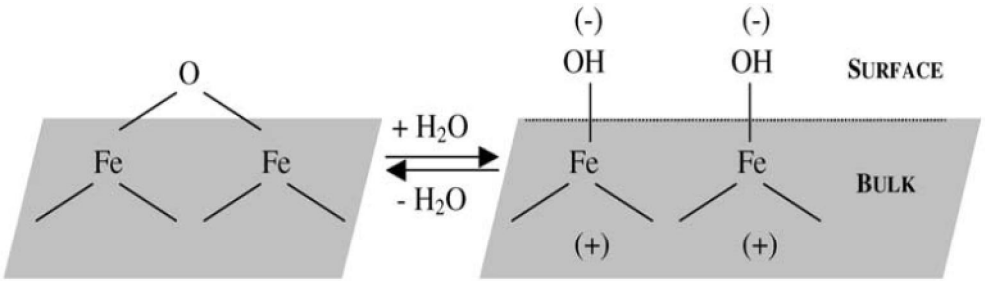

Fig.4.7. Hydroxylation of iron oxide due to water molecules

The adsorbed water molecules dissociate into hydroxyls causing the formation of a depletion layer which leads to an increase of resistance. By attracting electrons from the bulk they become negatively charged and give rise to a positive space charge region. The process is competitive with the adsorption of water in the molecular form as described in Fig. 4.6. At room temperature, the mechanism reported in Fig. 4.7 is slower than the one illustrated in Fig. 4.6, but it gains importance on increasing the temperature. However, because of the higher thermodynamic stability of the hydroxylated structure, water adsorption leads gradually with time to the hydroxylation of the metal oxide surface at room temperature.

At temperature higher than 400°C, the surface dehydroxylates with loss of water. This allows to recover the baseline resistance by heating at elevated temperature (>400°C).

Other than the increase of the baseline resistance, a loss of sensitivity at low RH was observed due to the same factor that is to say, the hydroxylation of the film surface through the mechanism reported in Fig. 4.7. However, the observed behaviors can be also due to a progressive transformation of amorphous iron oxy (hydroxy) phases into hematite. It is well known that amorphous iron oxy (hydroxy) phases such as ferrihydrite are formed at low temperature as that used during the films synthesis. These amorphous phases are not thermodynamically stable and with time, they tend to transform into the more stable and ordered α-Fe_2O_3 phase. The increase of

crystallinity, consequently, leads to a decrease of water chemisorption sites, and hence loss of sensitivity at low RH, and, on the other hand, to an increase of intergrain resistance.

Dopants play different roles. Li acts creating preferential adsorption sites for the H_2O molecules increasing the sensitivity at low RH [31].

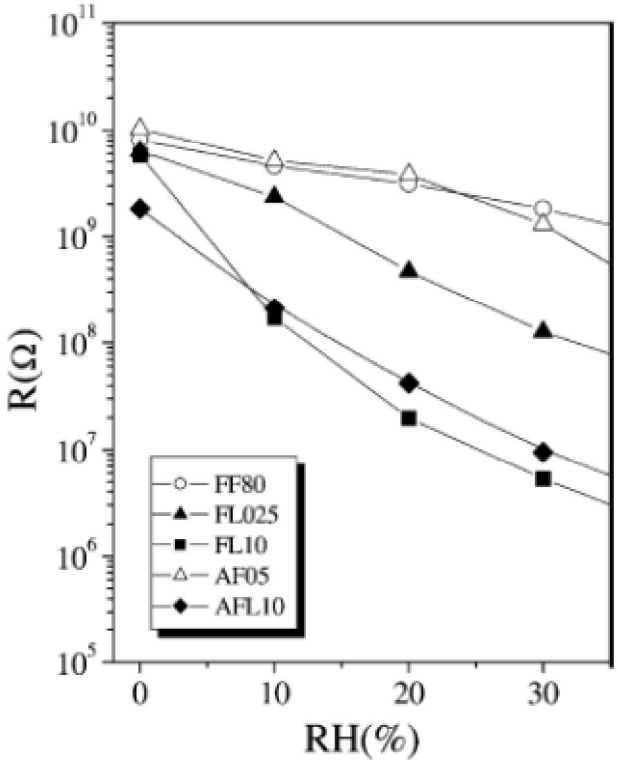

Fig.4.8. Variation of the resistance as a function of RH for various undoped and Li- and Au-doped iron oxide films. Annealing temperature of the films is 80◦C. (undoped Fe_2O_3 film is FF80 and iron oxide film doped with 5 wt% of gold is AF05 [31]

In general, alkali ions can also create surface defects or oxygen vacancies and possess high local charge density and strong electrostatic field for the smallest ions such as Li^+, resulting in an increase of adsorption sites for water-vapor adsorption [32].

Lithium addition to hematite by 5 wt% of Li_2O with a firing temperature of ranging from 850° to 950°C has been studied as a humidity sensor, as well as other alkali ions additions [32]. All the screen printed films presented a lack of response for low humidity atmospheres below 50 RH% (Fig. 4.9) [32].

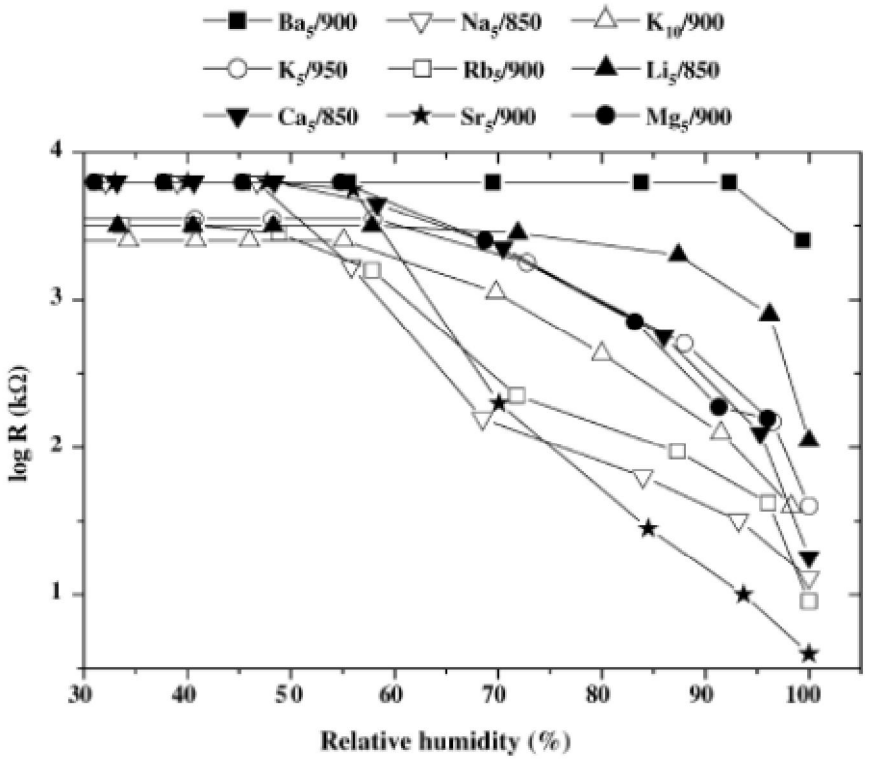

Fig.4.9. Sensors resistance at 30ºC in function of RH

Lithium additions to hematite also led to an increase of the porosity and the mean pore radius but did not change the pore size distribution as we can see in figure 4.10. [32].

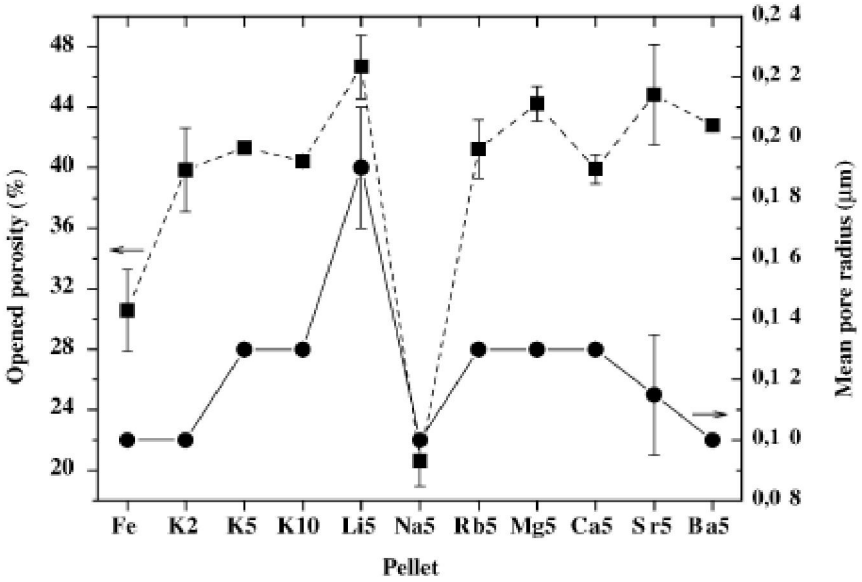

Fig.4.10. Total porosity and mean pore radius of the 900°C heat treated pellets of the different alkali and alkaline earth oxides doped iron oxide [32].

There are few papers in the literature dealing with pure and alkaline or earthy-alkaline doped hematite.

In table 4.5 are reported the NO_X sensors based on pure and doped-hematite.

Table 4.5. Principal iron oxides [3]

Material	**Sintering T (°C)**	**NO_X range (ppm)**	**Operating T (°C)**	**References**
α-Fe_2O_3, nanospheres	400-600	1000	210	[33]
Nb-doped hematite	800	0-100	150	[34]
Y-stabilized	1000-1200	50-436	600-700	[35]

$ZnFe_2O_3$				
Au-Zn- α-Fe_2O_3	400	25	150-400	[36]
α-Fe_2O_3 -In_2O_3	300	0-0.5	135	[37]
Alkaline, alkaline-earth elements doped hematite	1300	0–500	60-350	[38]
BaO - α-Fe_2O_3	1000	0.62-80	150-300	[39]

4.2.6. Lithium ferrite in gas sensing application

It has been used rarely for different gas sensing application; Li ferrite behaves being characterized by high electrical resistivity (105–106 Ω cm) and high Curie temperature (640–680 ˚C).

The characteristics of a semiconducting gas sensor have a major dependence on two factors. One is the intrinsic conduction mechanism and the other is the pore size and distribution. Both factors influence the kinetics of the chemisorption reaction between the sensor and the surrounding gases.

The electrical conduction in Li ferrite is attributed to electron hopping between the two valence state of iron, Fe^{2+} and Fe^{3+} on the octahedral sites in the spinel lattice.

The Fe^{2+} ion concentration depends upon several factors such as sintering temperature, atmosphere, and grain structure. In Li ferrite it is possible that some amount of Fe^{2+} ions appear due to Li evaporation during the heat treatment.

Samarium substituted lithium ferrites ($Li_{0.5}SmxFe_{2.5-x}O_4$), prepared by a sol–gel self-combustion route are suitable for ethanol or methanol sensing applications. The response of these materials is dependent on the operating temperature, porosity, gas

concentration and type. In the case of 200ppm methanol or ethanol concentration and operating temperature of 340 - 355°C, the response time is of about 3min for a response of 80–87%. The obtained results incite to deepen investigations on nanostructured Li ferrite as a sensor element for the detection of ethanol or methanol vapour and as well other gases [40].

Lithium ferrite ($LiFe_5O_8$) prepared by solid state reaction from 5 wt% equivalent of lithium oxide doped hematite investigated for NO_2 sensing applications [38]. Lithium doped hematite material showed an extrinsic n-type semiconducting behavior for temperature below 500°C. The study under NO_2 environment revealed that lithium doped hematite exhibited a singular behavior that author explained on the basis of a transition from n-to p-type conductivity due to the formation of an inversion layer.

AC electrical measurements were performed under 0–500 ppm NO_2 partial pressure in the 60–350 ◦C temperature range.

According to the author, the optimal working temperature is found to be at 250°C.

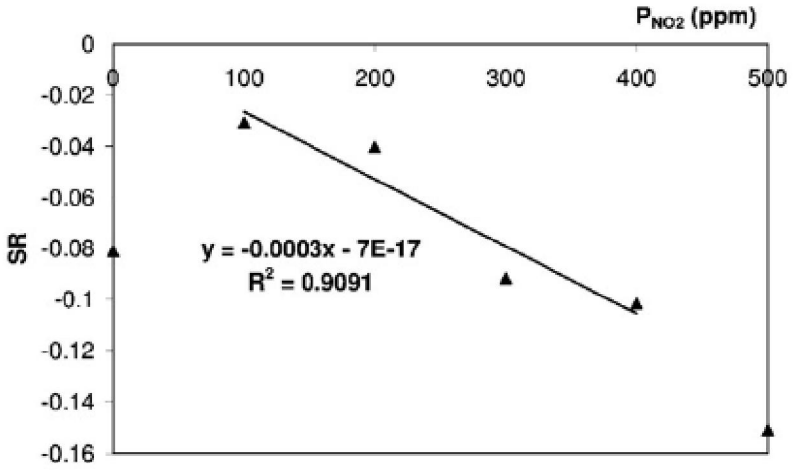

Fig.4.11. Sensor response (SR) in function of NO_2 partial pressure at 250°C of α-Fe_2O_3 + 5% Li_2O [38].

The remarkable linearity of 5% lithium doped hematite material response is promising for the targeted application [38].

Conclusions

In this part the interest for developing sensors based on hematite has been discussed. Different materials have been studied in the literature as humidity and gas sensors.

The composition, the synthesis conditions, the presence of defect and the electrodes geometries greatly influence sensor responses.

The aim of this part of my Ph.D. thesis is the development of a ceramic sensor based on hematite doped with lithium, starting from the production of doped powders to the electrical characterization under NO_X for environmental monitoring.

4.3. Li – doped iron oxide as a new material for NO_2 detection

Various compositions of lithium doped hematite containing 1, 2, 5, 10, 15, and 20 atomic percent were synthesized by solid state reaction, on the basis of previous results [38]. Lithium additions were chosen because it is well known in the literature that alkali ions can create surface defects or oxygen vacancies and possess high local charge density and strong electrostatic field for the smallest ions such as Li^+, resulting in an increase of adsorption sites for different gases adsorption. X-ray diffraction (XRD) and scanning electronic microscopy (SEM) observations were performed to follow the progressive evolution of the crystalline phases and of the microstructure of the materials. Electrochemical impedance spectroscopy (EIS) analyses under air and argon were used to determine the semiconducting behavior of the samples (n- or p-type). EIS analyses were also performed under various NO_2 partial pressures to investigate the sensitivity of these materials regarding the detection of such a gas.

4.3.1. Preparation Procedure

α-Fe_2O_3 commercial powder (Aldrich > 99 %, particle size distribution below 2 μm) were doped with alkaline and alkaline earths elements using the protocol reported in Figure 4.12.

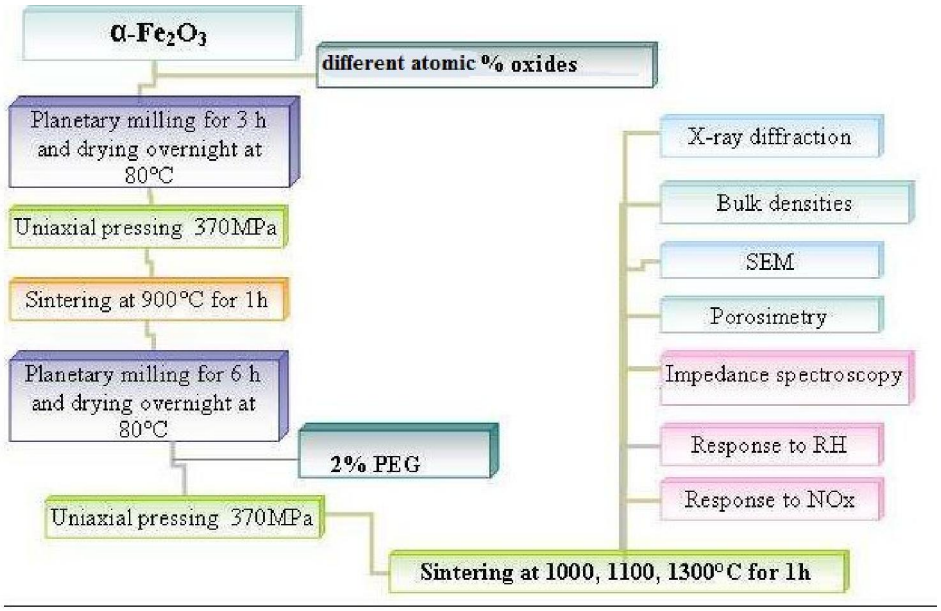

Fig.4.12. Preparation procedure of lithium-doped hematite pellets

α-Fe_2O_3 was mixed in ethanol with lithium carbonate (Li_2CO_3) as a precursor of 1, 2, 5, 10, 15 and 20 wt% equivalent of lithium oxides (Fluka > 99 %), in a planetary mill, in agate jars with agate balls, for 1 hour. After drying overnight in an oven, the mixtures were uniaxially pressed at 370 MPa and calcined at 900°C for 1 hour. Then, the samples were manually ground with an agate mortar and an agate pestle, prior to planetary mill them for 6 hours in agate jars with agate balls. The grain size of the produced powders was then controlled by laser granulometry. The retained solution was to increase the green density of the pellets by adding polyethylene glycol (PEG 4000, Sigma-Aldrich) to the doped powder, during the 6 hours planetary milling step. As, the densest material, decreases the possibility of humidity cross-sensitivity with

the targeted gas. Then, pellets were uniaxially pressed at 370 MPa and heat treated at 1300°C for 1 hour, with an heating ramp of 5°C/min. This sintering temperature was chosen because of the high value of relative densities as the theoretical one (5.27g/cm^3) where obtained with pure hematite.

4.3.2. Chemical and physical characterization

The fired materials were characterized by XRD (Philips PW 3830) in the 5-70° in 2 theta range, with a CuKα radiation (and a step size of 0.02° and 2 s per step) (Fig. 4.13).

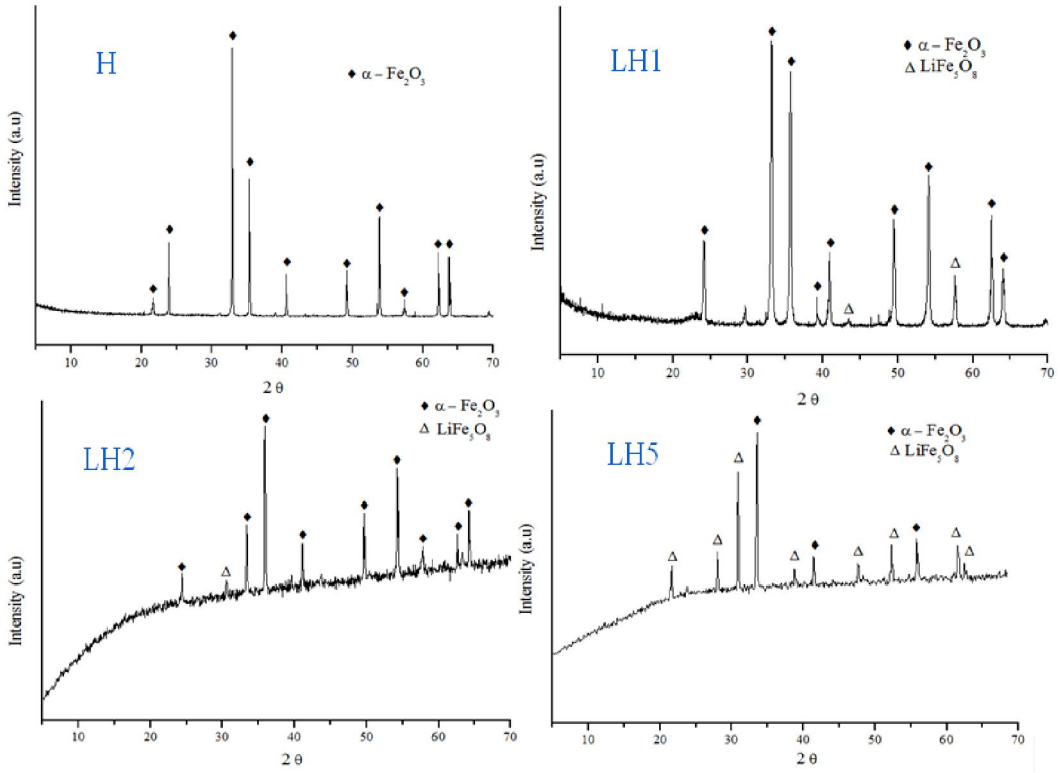

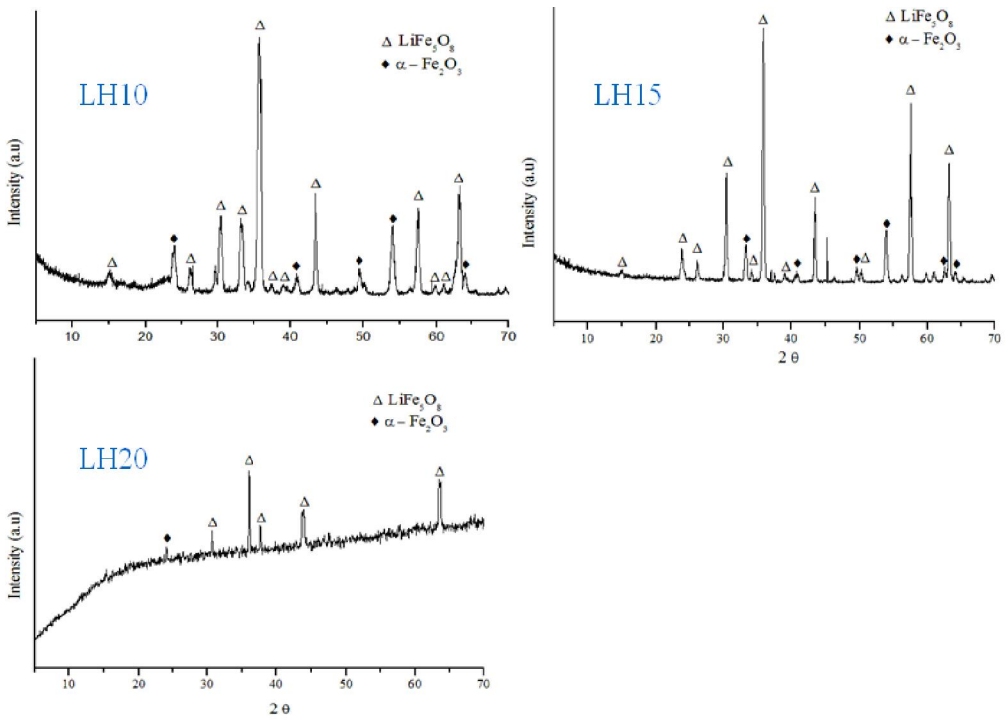

Fig.4.13. XRD patterns of (H) Hematite a lone, (LH1) Li doped hematite 1 %,(LH2) Li doped hematite 2 %, (LH5) Li doped hematite 5 %,(LH10) Li doped hematite 10 %, (LH15) Li doped hematite 15 %, and (LH20) Li doped hematite 20 % [JCPDS card: 33 – 0664 α-Fe_2O_3, 38 – 0259 $LiFe_5O_8$.

X-ray diffraction patterns on the lithium doped hematite evidenced the formation of the ferrites $LiFe_5O_8$ and $liFeO_2$, with the increasing content of lithium oxide, the tendency of pure ferrites formation tops the scene.

SEM observations:

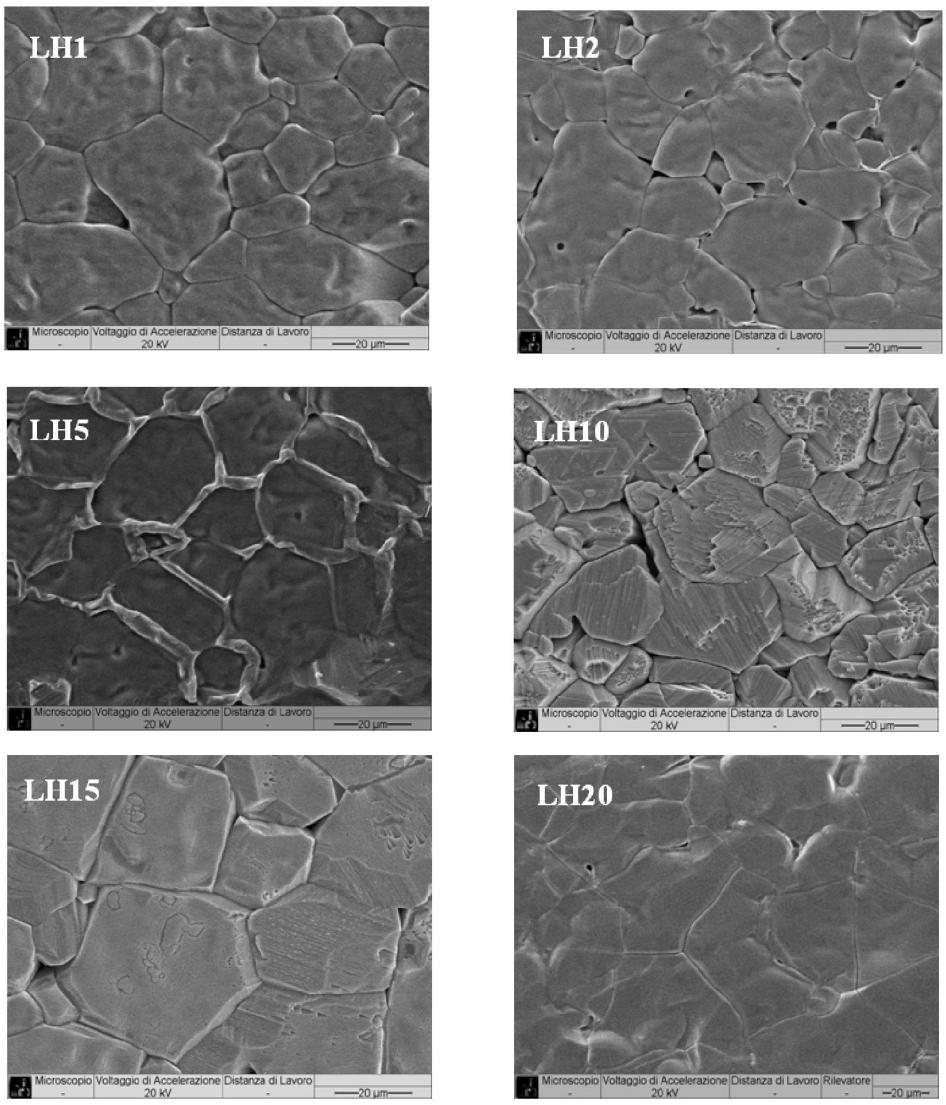

Fig.4.14. SEM micrographs of (LH1) Li doped hematite 1 %, (LH2) Li doped hematite 2 %, (LH5) Li doped hematite 5 %, (LH10) Li doped hematite 10 %, (LH15) Li doped hematite 15 %, and (LH20) Li doped hematite 20 % after sintering at 1300°C for 1 h

SEM observations show that samples are quite well dense and when increasing the atomic percentage of Li, grain size increases (Fig. 4.13).

4.3.3. Humidity test

The samples were first studied as humidity sensors in preliminary tests, because it is known in literature that water molecules can interfere with NO_X detection.

The powders were uniaxially pressed at 370 MPa and sintered at 1300°C before the electrodes deposition.

Interdigitated gold electrodes (ESL 520 A) were screen-printed onto the surface of the pellets and fired at 520°C for 18 minutes (Fig. 4.15). Sensors humidity response was studied in the range 0-100% relative humidity (RH) in a laboratory apparatus described in Appendix 1.

Fig.4.15. Example of bulk sensor

After the electrical characterization under different relative humidity percentages, from the sensors resistance value the sensor response SR was calculated on the basis of equation (3):

$$SR\ \% = [(R(P_{gas}) - R(P_{gas \to 0})) / R(P_{gas \to 0})]. 100 \quad (3)$$

Where R (P_{gas}) is the total resistance of the material when exposed under P (gas) partial pressure and R ($P_{gas \to 0}$) is the resistance measured when the gas partial pressure tends towards zero [41].

The sensor responses SR % of the previously described materials are a function of time, varying the relative humidity every 3 minutes; in Figure 4.15, each point corresponding at the SR % relative at the third minute are illustrated.

The pure hematite showed a slight increase of its electrical resistances above ca. 80 RH%, 1 and 2 % Li_2O doped hematite showed slightly increase over 70 RH%, while the remaining Li doped hematite materials were slightly more sensitive to water vapor (from 30 to 40 RH%).

In general, the SR dependence of Li doped hematite samples with relative humidity was too small. Therefore, the possibility to use Lithium doped hematite as a NO_2 sensor increased as the cross sensitivity of NO_2 with water vapor could be neglected.

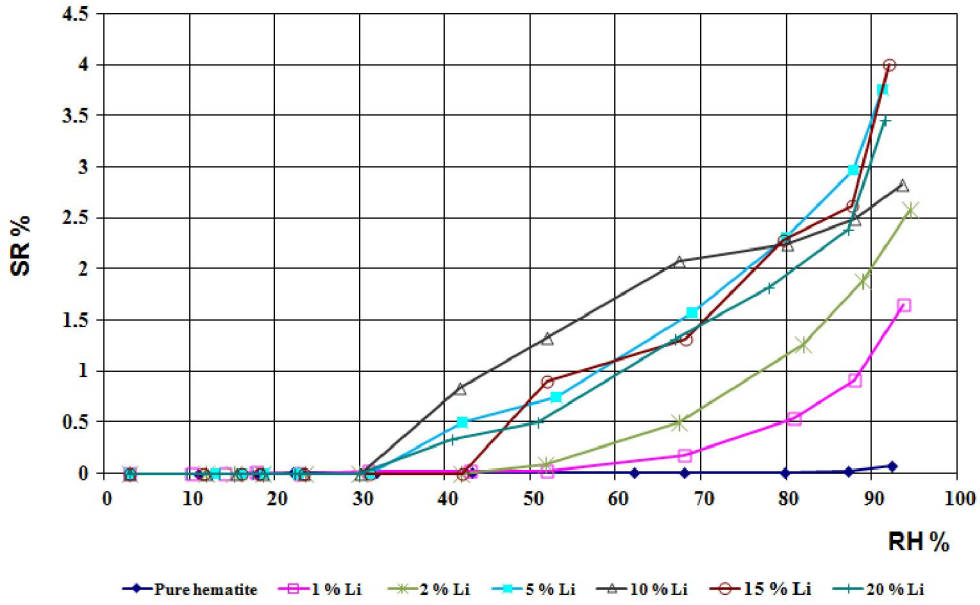

Fig.4.16.SR% of Li doped hematite samples with relative humidity%

4.3.4. Electrical characterization by impedance spectroscopy

The electrical characterization of the materials was performed by means of AC impedance spectroscopy in collaboration with INP-LEPMI-IES of Grenoble (France). Platinum electrodes were painted onto each faces of the pellets (~1 - cm in diameter and ~1 mm thick) then impedance spectroscopy measurements were carried out under dry synthetic air (80% N_2-20% O_2) and argon (<$2x10^{-6}$ atm O_2), between 100 and

700°C, in the 5 Hz – 13 MHz frequency range and a 100 mV amplitude signal (Hewlett Packard HP 4192A LF Impedance Analyzer) (Fig. 4.17).

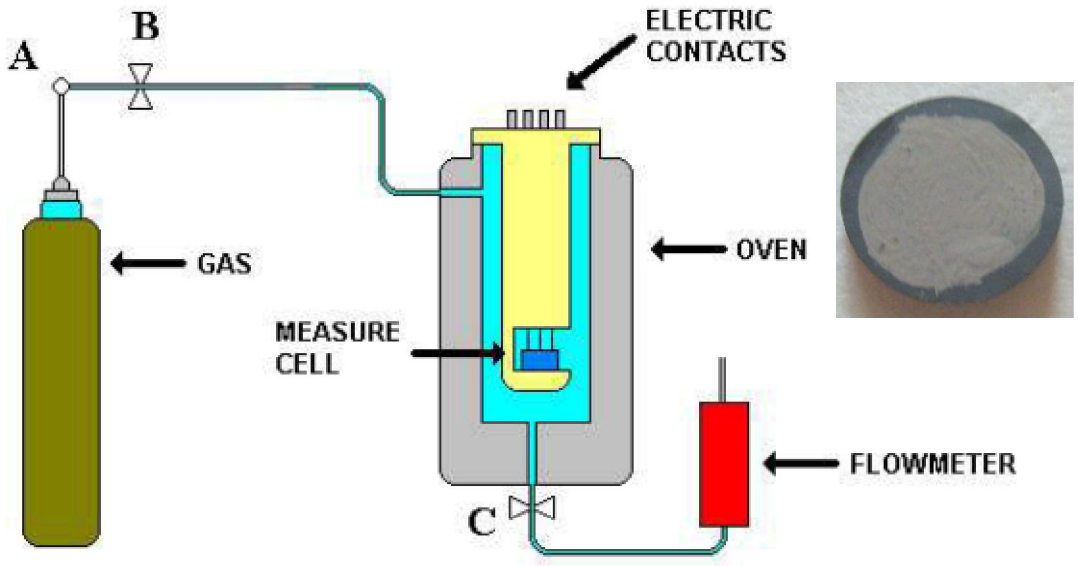

Fig.4.17. Scheme of the apparatus used for impedance measurement

After preliminary tests, a strong dependence of the resistance due to the presence of residual hydroxyl groups onto the surface of the pellets was evidenced.

A previously heating treatment up to 700°C was then applied before each electrical analysis (fig.4.18). This latter consisted in a succession of AC impedance measurements during cooling and heating under the same gas atmosphere in order to verify the reproducibility of each result.

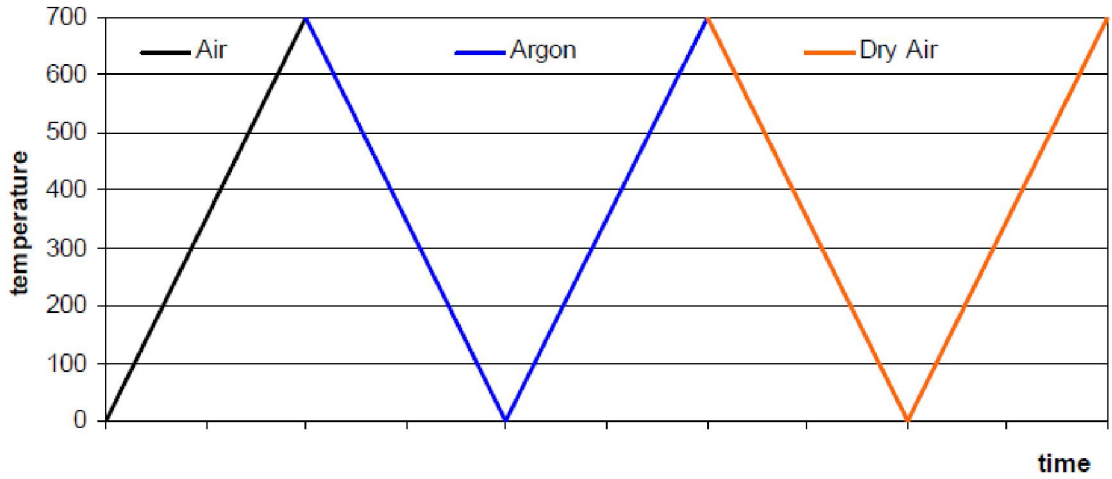

Fig.4.18. Heat-treatment used for impedance spectra measurements

Before the beginning of the impedance characterization, the flow rate was calibrated for the different gases used in the analysis, synthetic air and argon for the electrical characterization and helium, argon and NO_2 for the NO_2 measurements.

The flows were controlled by an electronic flowmeter with a tension comprised between 0 and 5 V; tension values were correlated to the flow rate by calibration curves (Figure 4.19). The calibration was performed using graduated capillary containing water and soap, subsequently the gas was flowed inside the capillary and the soap bubbles were counted for determining the flow rate in mL per minute.

For the characterization under NO_2, different concentrations of gas were used by diluting in argon, in the first measurements, and in helium, for the successive tests a NO_2 flux.

The overall flow rate was kept constant at 40 mL/min. Tension values corresponding to NO_2 concentrations comprised between 0 and 500 ppm are reported in Table 4.6.

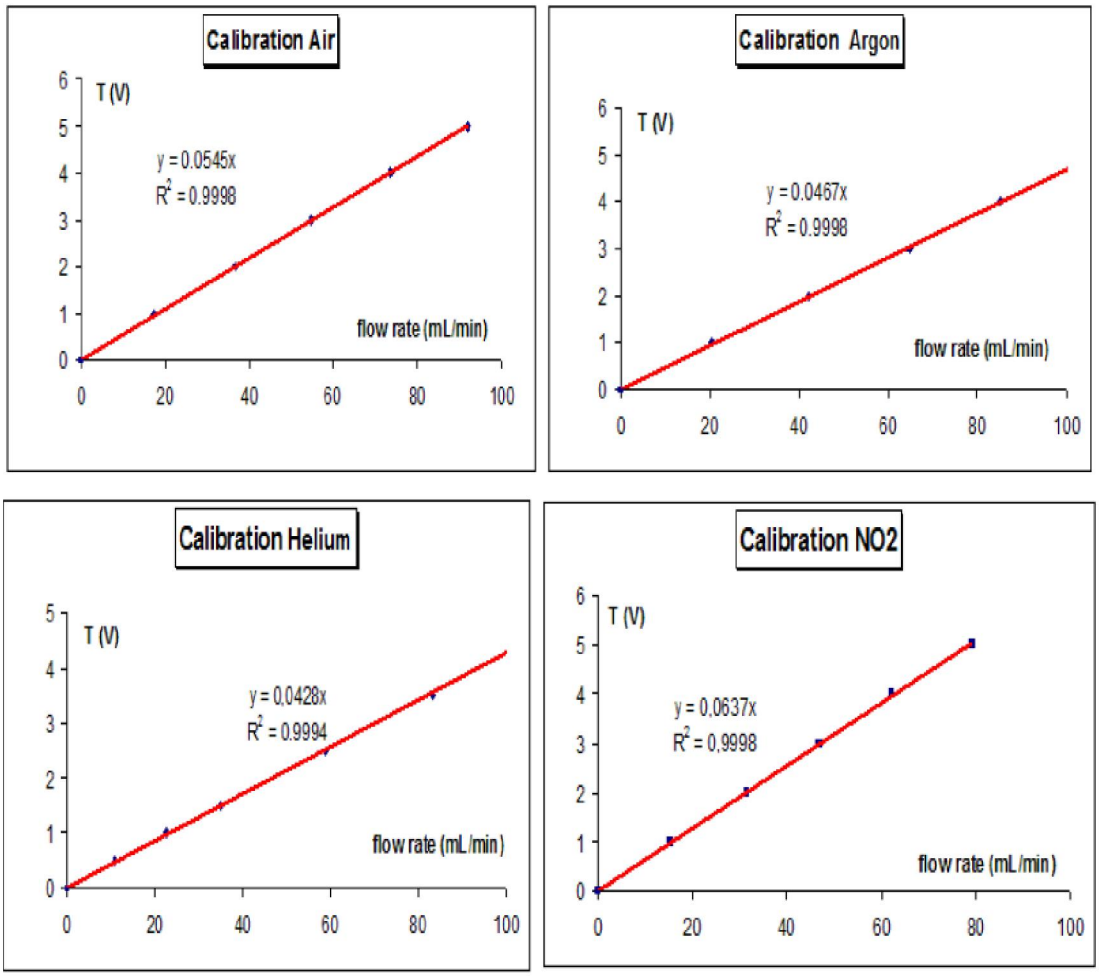

Fig.4.19.Calibration curve of the different gases used during impedance spectroscopy

Table 4.6. NOx concentration of argon and helium (total flow of 40 mL/min)

[NOX] (ppm)	NOX flow	T (V)	Ar flow	T (V)	He flow	T (V)
0	0	0.00	40	1.87	40	1.71
50	2	0.13	38	1.77	38	1.63
100	4	0.25	36	1.68	36	1.54
200	8	0.51	32	1.49	32	1.37
300	12	0.76	28	1.31	28	1.20
400	16	1.02	24	1.12	24	1.03
500	20	1.27	20	0.93	20	0.86

Three different electrical behaviors of the materials are expected:

1) the conductivity increases when increasing the partial oxygen pressure, in this case the holes prevail in the conduction (equation 4); this is the typical behavior of a p-type semiconductor:

$$\frac{1}{2}O_2 \Leftrightarrow O_i'' + 2h^{\cdot} \quad (4)$$

2) The conductivity decreases when increasing the partial oxygen pressure, in this case the electrons prevail in the conduction (equation 5); this is the characteristic behavior of a n-type semiconductor

$$O_O^{\times} \Leftrightarrow \frac{1}{2}O_2 + V_O^{\cdot\cdot} + 2e^{`} \quad (5)$$

3) The conductivity does not change in the different atmospheres, in this case the conduction is due to the ions; this is the typical behavior of an ionic conductor [42].

4.3.4.1. Measurements under air/argon

The Figure 4.19 shows the conductivities evolutions in Arrhenius representations of pure hematite and different concentrations of lithium-doped hematite samples. The conductivities were calculated on the basis of the total resistance measured by means of a.c. impedance spectroscopy the geometrical features of the samples. The impedance measurements have been realized under synthetic air and argon atmospheres successively.

From the Figure 4.19, it was possible to distinguish three different types of electrical behaviors:

1) Pure hematite, 1 and 2% of Li_2O doped hematite samples present a linear dependence of the conductivity with superimposition of the measurements under air and argon. This is the behavior of an intrinsic semiconductor.

2) Samples 10, 15 and 20% Li_2O doped hematite showed no influence of the oxygen partial pressure above 500°C ($1000/T < 1.3\ K^{-1}$); while a strong influence of the oxygen partial pressure below 500°C ($T/1000 > 1.3\ K^{-1}$) was evidenced. This means that the mentioned samples present the behavior of a n-type extrinsic semiconductor for temperatures below 500°C as in the case of barium ferrites [43]. The conductivity increases when the partial pressure of oxygen decreases. The samples behave as an intrinsic semiconductor for temperatures above 500°C.
3) The 5% Li_2O doped hematite sample showed an intermediate behavior between the two cases previously described as it showed an influence to the oxygen for all the range of temperature used for the measurement.

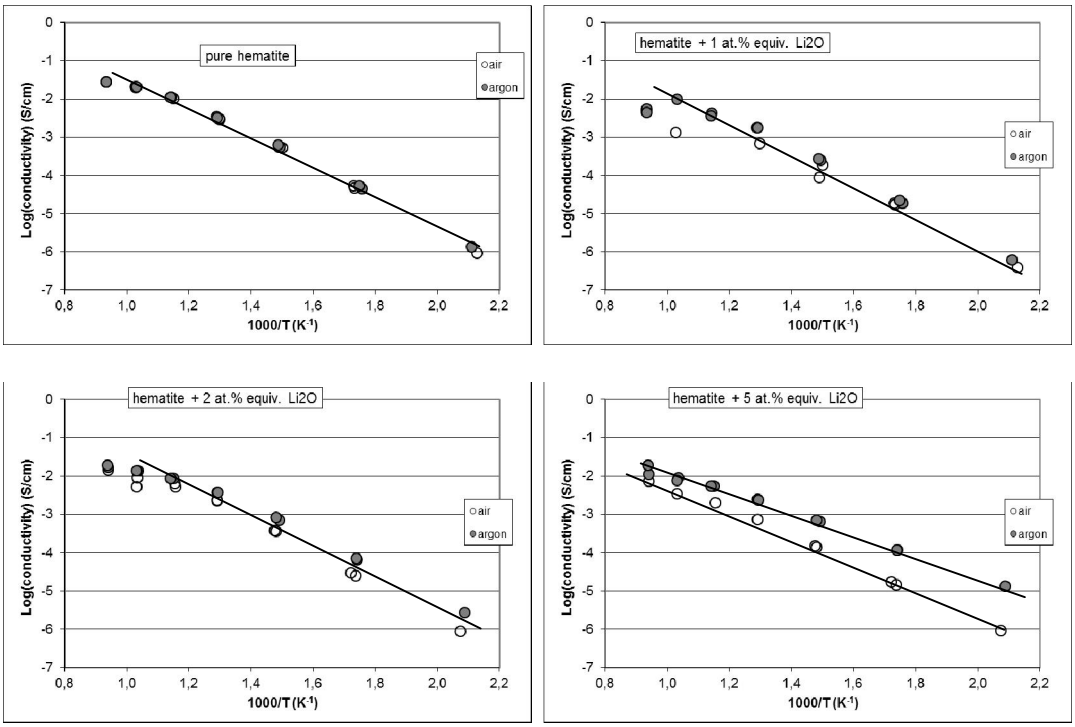

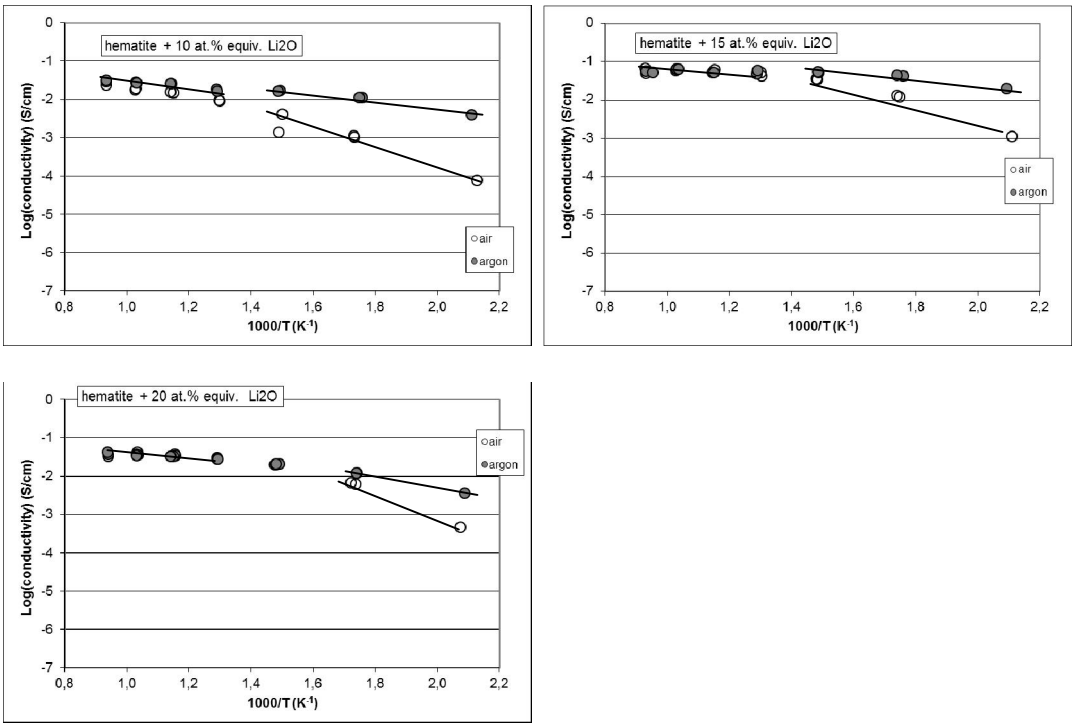

Fig.4.20. Arrhenius diagram of the conductivity under dry air and argon of pure a - Fe_2O_3, a- Fe_2O_3 + 1% Li_2O, a- Fe_2O_3 + 2% Li_2O, a- Fe_2O_3 + 5% Li_2O, a- Fe_2O_3 + 10% Li_2O, a- Fe_2O_3 + 15% Li_2O and a- Fe_2O_3 + 20% Li_2O

Table 4.7. summarizes the values of the activation energies, deduced from the linear regions of the six Arrhenius representations presented on the Figure 4.19 and calculated according to the equation (6) [44].

$$\sigma = \sigma_0 . e^{(-E/RT)} \quad (6)$$

Where σ represent the conductivity at a temperature T, σ_0 the conductivity constant, E denotes the conductance activation energy and R is the Boltzmann constant.

The n-type semiconductor behaviour of hematite is clearly reported in literature.

Oxygen vacancies ($V_O^{\cdot\cdot}$) can be produced by heating this material following the disorder equation (7) [45]:

$$O_O^{\times} \Leftrightarrow \frac{1}{2}O_2 + V_O^{\cdot\cdot} + 2e^{`} \quad (7)$$

Table 4.7. Activation energies calculated from the linear regions of the Figure 4.19

Sample	Activation energy (eV)			
	Below 500°C		Above 500°C	
	Argon	Air	Argon	Air
α-Fe_2O_3	0.73			
α - Fe_2O_3 + 1% Li_2O	0.68			
α - Fe_2O_3 + 2% Li_2O	0.64			
α - Fe_2O_3 + 5% Li_2O	0.59	0.76	0.26	0.40
α - Fe_2O_3 + 10% Li_2O	0.19	0.55	0.075	0.16
α - Fe_2O_3 + 15% Li_2O	0.14	0.46	0.008	
α - Fe_2O_3 + 20% Li_2O	0.18	0.39	0.07	0.09

Gardner et al. [46] measured the oxygen deficit resulting from this equilibrium shift. Considering this structural disorder and the independence of pure hematite conductivity regarding the oxygen partial pressure shown in the figure 4.19 for pure hematite, 1 and 2 % of Li_2O doped hematite which have the same behaviour, we could conclude that those materials are intrinsic semiconductors [45, 47]. The large value of the activation energy measured in this work for pure hematite (0.73 eV), 1% Li_2O doped hematite (0.68 eV), and 2% Li_2O doped hematite (0.64 eV) are the consequence of our experimental procedure where samples were sintered at 1300°C and cooled under air laboratory. Under those conditions, the oxygen vacancies created

during the heat treatment disappear by re-oxidation [48] and hematite, as well as, 1% Li_2O doped hematite and 2% Li_2O doped hematite become a slight n-type semiconductor [49]. The value of 0.73 eV obtained in the present work for hematite is close from the one reported by Gardner [46].

Conductivity of 10, 15 and 20 % Li_2O doped hematite materials show large dependence with oxygen partial pressure for temperatures below 500°C. Furthermore, the conductivities increase as the oxygen partial pressure decreases, in fact the conductivities under argon are higher than the conductivities under air. This corresponds to the behavior of an n-type extrinsic semiconductor.

Kim et al. [45] suggested a doping process with CdO for the reduction of a part of Fe(III) to Fe(I), oxygen vacancies formation and concentration increase of negative charge carriers (electrons). They also suggested that the semiconduction became intrinsic for temperature above 500°C. We observe the same phenomenon and the activation energies deduced from the Figure 4.19. are close from the values obtained by Gardner et al. [5] on pure hematite in the same temperature range (0.1 to 1.3 eV).

4.3.4.2. Measurements under NO_X

Pure hematite and Lithium doped hematite materials were tested under NO_2 partial pressure (0 to 500 ppm) in the 200 – 400°C temperature range.

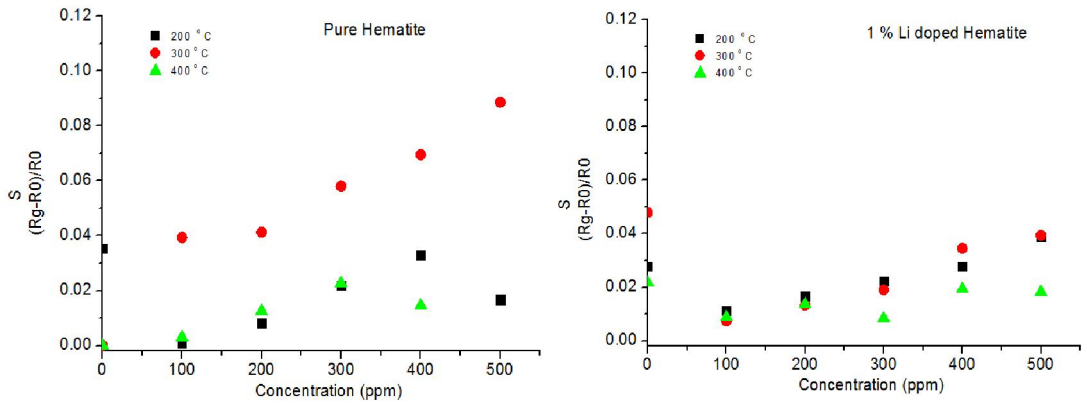

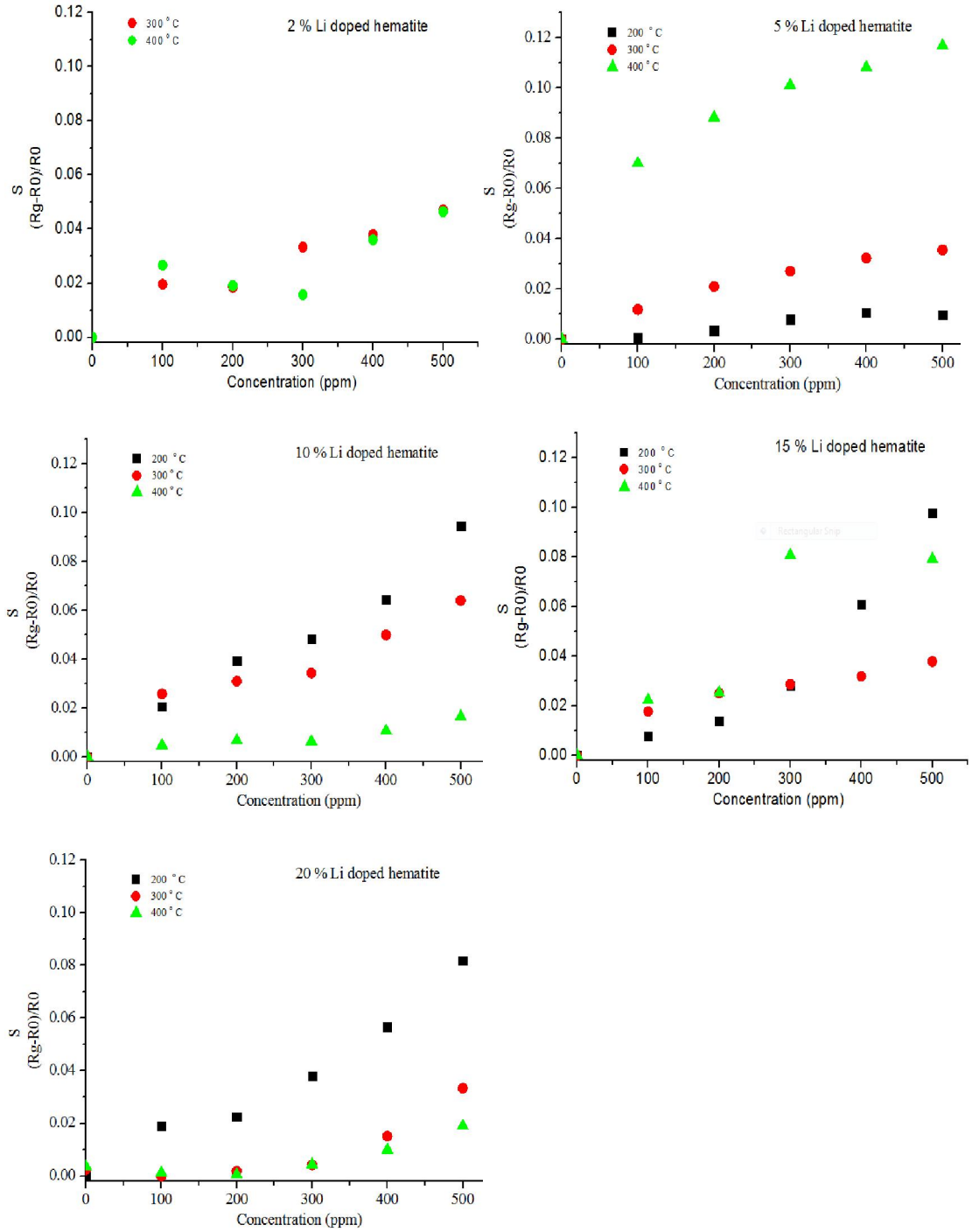

Fig.4.21. Sensor responses of pure hematite, 1, 2, 5, 10, 15 and 20 atomic % of Li_2O doped hematite at different operating temperatures (200 – 400°C)

Generally, Hematite samples show poor response regarding NO_2 partial pressure. This is quite clear in the case for 1, 2 % samples.

Pure hematite sample gives non negligible response, which could be due to its low conductivity especially at 300°C see figure 4.20.

The most encouraging results are those concerning samples containing a high proportion of lithium ferrite 10, and 20% Li_2O at a quite low operating temperature 200°C. The increase in resistance is explained as in the case of barium ferrites [41] by the fact that NO_2, an oxidizing gas, adsorbed onto the surface of a n-type semiconductor material, decreases the concentration of the free charge carriers (electrons in this case) and therefore the material conductivity.

While 5% Li_2O doped hematite sample gave the best sensor signal among all the samples at quite high operating temperature 400ºC.

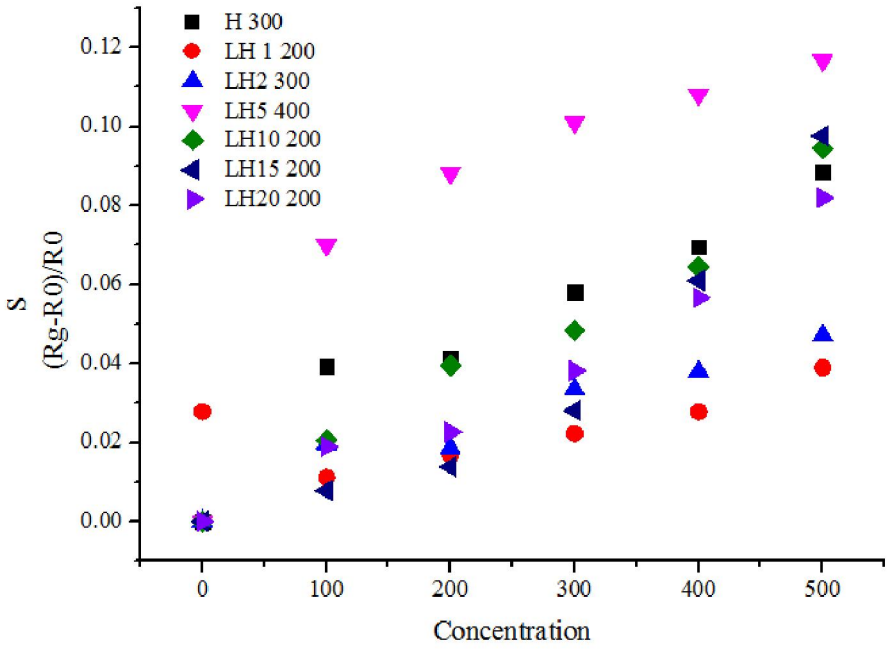

Fig.4.22.Sensor responses of pure hematite and all other different atomic % of Li_2O doped hematite which gave the best response at the different investigated operating temperatures.

Conclusions

Preparation of different ferrites from Fe_2O_3 – Li_2O system by solid state reaction has been successfully done.

Lithium doped hematite samples exhibit an n type semiconducting behavior.

Lithium ferrites could work as NO_2 sensor at a quite low operating temperature (200°C).

Generally, sensor response of lithium ferrites towards NO_2 is not the best but still it gives an acceptable linear evolution with gas concentration for some compositions.

References

1. http://minerals.usgs.gov, 17/11/2012.
2. X. Gou, G. Wang, J. Park, H. Liu and J. Yang, Monodisperse hematite porous nanospheres: synthesis, characterization, and applications for gas sensors, Nanotechnology 19 (2008) 125606, 1-7.
3. http://www.handbookofmineralogy.com, 17/11/2012.
4. C. Y. Oh, J. H. Oh and T. Ko, The Microstructure and Characteristics of Magnetite Thin Films Prepared by Ultrasound-Enhanced Ferrite Plating, IEEE Transactions on magnetics, 38 (2002) 3018-3020.
5. R. Tongpool, S. Jindasuwan, Sol–gel processed iron oxide–silica nanocomposite films as room-temperature humidity sensors, Sensors and Actuators B, 106 (2005) 523–528.
6. H. Y. Wang, X. J. Li, Structural and capacitive humidity sensing properties of nanocrystal magnetite/silicon nanoporous pillar array, Sensors and Actuators B, 110 (2005) 260–263.
7. P. Pascal, Traité de chimie minérale, Fer, (1968) 691-699.
8. P. Pascal, Traité de chimie minérale, Fer, (1968) 1-100.
9. P. Venema, T. Hiemstra, P.G. Weidler and W.H. van Riemsdijk, Intrinsic proton affinity of reactive surface groups of metal (hydr)oxides: application to iron (hydr)oxides, Journal of colloid and interface science, 198 (1998), 282-295.
10. www.mindat.org, 02/12/2012.
11. http://webmineral.com, 02/12/2012.

12. B. M Warnes, F. F. Aplan and G. Simkovich, Electrical conductivity and Seebeck voltage of Fe_2O_2 pure and doped, as a function of temperature and oxygen pressure, Solid State Ionics, 12 (1984) 271-276.
13. C. V. Santilli, J. P. Bonnet, P. Dordor, M. Onillion and P. Hagenmuller, Influence of structural defects on the electrical properties of α-Fe2O3 ceramics, Ceramic International, 16 (1990), 25-32.
14. K. H. Kim, S. H. Lee and J. S. Choi, Electrical conductivity of pure and doped α-ferric oxides, Journal of Physical Chemistry Solids, 46 (3) (1985) 331-338.
15. R. F. G. Gardner, F. Sweett and D. W. Tanner, The electrical properties of alpha ferris oxide-II. Ferric oxide of high purity, 24 (1963) 1183-1196.
16. R. H. Chang and J. B. Wagner, Direct-current conductivity and iron tracer diffusion in hematite at high temperatures, J. Am. Cer. Soc., 55 (1972) 211-213.
17. P. Pascal, Traité de chimie minérale, Fer, (1968) 701-732.
18. B. T. Shirk, US Patent 3,630,667, Production of barium ferrite, (1971).
19. E. M. Levin, F. P. Hall, H. F. McMurdie, Phase diagrams for ceramists, Columbus American ceramic society, (1956) 54.
20. M. Pelino, C. Colella, C. Cantalini, M. Faccio G. Ferri and A. D'Amico; Microstructure and electrical properties of an α-hematite ceramic humidity sensor, Sensors and Actuators B, B7 (1-3) (1992) 464-469.
21. X. Gou, G. Wang, J. Park, H. Liu and J. Yang, Monodisperse hematite porous nanospheres: synthesis, characterization, and applications for gas sensors, Nanotechnology 19 (2008) 125606 , 1-7.

22. J. M. Tulliani and P. Bonville; Influence of the dopants on the electrical resistance of hematite-based humidity sensors, Ceramics International, 31(4) (2005) 507-514.

23. G. Gusmano, G. Montesperelli, B. Morten, M. Prudenziati, A. Pumo and E.Traversa; Thick films of $MgFe_2O_4$ for humidity sensors; Journal of Materials Processing Technology, 56 (1996) 589 – 599.

24. J. Shah, R. K. Kotnala, B. Singh and H. Kishan, Microstructure-dependent humidity sensitivity of porous $MgFe_2O_4$–CeO_2 ceramic, Sensors and Actuators B, 128 (2007) 306–311.

25. R. K. Kotnala, J. Shah, B. Singh, H. kishan, S. Singh, S.K. Dhawan and A. Sengupta, Humidity response of Li-substituted magnesium ferrite, Sensors and Actuators B, 129 (2008), 909–914.

26. G. Neri, A. Bonavita, S. Galvagno, C. Pace, S. Patanè and A. Arena, Humidity sensing properties of Li–iron oxide based thin films, Sensors and Actuators B, B73 (2-3) (2001), 89-94.

27. G. Neri, A. Bonavita, C. Milone, A. Pistone and S. Galvagno, Gold promoted Li– Fe_2O_3 thin films for humidity sensors, Sensors and Actuators B, B92 (3) (2003) 326-330.

28. G. Neri, A. Bonavita, S. Galvagno, N. Donato and A. Caddemi, Electrical characterization of Fe_2O_3 humidity sensors doped with Li+, Zn^{2+} and Au^{3+} ions, Sensors and Actuators B, 111-112 (2005) 71-77.

29. M. Pelino, C. Cantalini, H.-T. Sun and M. Faccio, Silica effect on α-Fe_2O_3 humidity sensor, Sensors and Actuators, B3 (1998), 186-193.

30. A. Esteban-Cubillo, J.M. Tulliani, C. Pecharromán and J. S. Moya, Iron-oxide nanoparticles supported on sepiolite as a novel humidity sensor, Journal of the European Ceramic Society, 27 (2007), 1983–1989.
31. G. Neri, A. Bonavita, C. Milone, A. Pistone, S. Galvagno, Gold promoted Li–Fe_2O_3 thin films for humidity sensors, Sensors and Actuators B 92 (2003) 326–330.
32. J.-M. Tulliani and P. Bonville, Influence of the dopants on the electrical resistance of hematite-based humidity sensors, Ceramics International 31 (2005) 507–514.
33. O. Berger, T. Hoffmann, W.-J. Fischer and V. Melev, Tungsten-oxide thin films as a novel material with high sensitivity to NO_2, O_3, and H_2S. Part II: application as a gas sensors, Journal of Materials Science: Materials in Electronics, 15 (2004), 483-493.
34. A. Chiorino, G. Ghiotti, F. Prinetto, M. C. Carotta, D. Gnani and G. Martinelli; Preparation and characteriziation of SnO_2 and MoO_x–SnO nanosized powders for thick film gas sensors, Sensors and Actuators, B58 (1999) 338-349.
35. H. T. Sun, C. Cantalini, M. Faccio and M. Pelino, NO_2 gas sensitivity of sol-gel- derived α-Fe_2O_3 thin films, Thin Solid Films, 269 (1995) 97-101.
36. C. Cantalini, H.T. Sun, M. Faccio, G. Ferri and M. Pelino, Niobium-doped α-Fe_2O_3 semiconductor ceramic sensors for the measurement of nitric oxide gases, Sensors and Actuators, B, B25 (1-3) pt 2 (1995) 673-677.
37. S. Zhuiykov, T. Ono, N. Yamazoe and N. Miura, High-temperature NO_x sensors using zirconia solid electrolyte and zinc-family oxide sensing electrode, Solid State Ionics, Diffusion & Reactions, 152-153 (2002) 801-807.

38. J.-M. Tulliani, C. Baroni, C. Lopez, L. Dessemond, New NO_x sensors based on hematite doped with alkaline and alkaline-earth elements, Journal of the European Ceramic Society 31 (2011) 2357–2364.

39. M. Debliquy, C. Baroni, A. Boudiba, J.-M. Tulliani, M. Olivier, C. Zhang, Sensing characteristics of hematite and barium oxide doped hematite films towards ozone and nitrogen dioxide, Procedia Engineering 25 (2011) 219 – 222.

40. N. Rezlescu, C. Doroftei, E. Rezlescu, P.D. Popa, Lithium ferrite for gas sensing applications, Sensors and Actuators B, 133 (2008) 420–425.

41. T. G. Nenov and S.P. Yordanov; Ceramic sensor – Technology and Applications, (1996) 65-70.

42. T. G. Nenov and S.P. Yordanov; Ceramic sensor – Technology and Applications, 1996, 65-70.

43. C. Lopez, C. Baroni and J-M. Tulliani, Ba-Doped Iron Oxide as a New Material for NO_2 Detection, Materials 6 (2013) 4801-4816.

44. H. T. Sun, C. Cantalini, M. Faccio and M. Pelino, NO_2 gas sensitivity of sol-gel derived α-Fe_2O_3 thin films, Thin Solid Films, 269 (1995) 97-101.

45. K. H. Kim, S. H. Lee and J. S. Choi, Electrical conductivity of pure and doped α-ferric oxides, Journal of Physical Chemistry Solids, 46 (1985) 331-338.

46. R. F. G. Gardner, F. Sweett and D.W. Tanner, The electrical properties of alpha ferris oxide-II. Ferric oxide of high purity, 24 (1963) 1183-1196.

47. R. H. Chang and J. B. Wagner, Direct-current conductivity and iron tracer diffusion in hematite at high temperatures, Journal of the American Ceramic Society, 55 (1972) 211-213.

48. H. T. Sun, C. Cantalini, M. Faccio and M. Pelino, NO_2 gas sensitivity of sol-gel derived α-Fe_2O_3 thin films, Thin Solid Films, 269 (1995), 97-101.
49. H. E. N. Stone, Electrical conductivity and sintering in iron oxides at high temperatures, Journal of Materials Science, 3 (1968) 321-325.